

**ACTIVE MICROWAVE REMOTE SENSING OF SOIL MOISTURE:
A CASE STUDY IN KURUKAVAK BASIN**

**A THESIS SUBMITTED TO
THE GRADUATE SCHOOL OF NATURAL AND APPLIED SCIENCES
OF
MIDDLE EAST TECHNICAL UNIVERSITY**

BY

MUSA YILMAZ

**IN PARTIAL FULFILLMENT OF THE REQUIREMENTS
FOR
THE DEGREE OF DOCTOR OF PHILOSOPHY
IN
CIVIL ENGINEERING**

DECEMBER 2008

Approval of the thesis:

**ACTIVE MICROWAVE REMOTE SENSING OF SOIL MOISTURE:
A CASE STUDY IN KURUKAVAK BASIN**

submitted by **MUSA YILMAZ** in partial fulfillment of the requirements for the
**Degree of Doctor of Philosophy in Civil Engineering Department, Middle
East Technical University** by,

Prof. Dr. Canan Özgen

Dean, Graduate School of **Natural and Applied Sciences**

Prof. Dr. Güney Özcebe

Head of Department, **Civil Engineering**

Prof. Dr. Ali Ünal Şorman

Supervisor, **Civil Engineering Dept., METU**

Examining Committee Members:

Prof. Dr. Melih Yanmaz

Civil Engineering Dept., METU

Prof. Dr. Ali Ünal Şorman

Civil Engineering Dept., METU

Prof. Dr. Vedat Toprak

Geological Engineering Dept., METU

Assoc. Prof. Dr. Zuhale Akyürek

Civil Engineering Dept., METU

Assoc. Prof. Dr. Günay Erpul

Agricultural Faculty, Ankara University

Date: 31/12/2008

I hereby declare that all information in this document has been obtained and presented in accordance with academic rules and ethical conduct. I also declare that, as required by these rules and conduct, I have fully cited and referenced all material and results that are not original to this work.

Name, Last name: Musa Yilmaz

Signature:

ABSTRACT

ACTIVE MICROWAVE REMOTE SENSING OF SOIL MOISTURE: A CASE STUDY IN KURUKAVAK BASIN

YILMAZ, Musa

Ph.D., Department of Civil Engineering

Supervisor: Prof. Dr. Ali Ünal Şorman

December 2008, 135 pages

Soil moisture condition of a watershed plays a significant role in separation of rainfall into infiltration and surface runoff, and hence is a key parameter for the majority of physical hydrological models. Due to the large difference in dielectric constants of dry soil and water, microwave remote sensing and particularly the commonly available synthetic aperture radar is a potential tool for such studies.

The main aim of this study is to produce the distributed soil moisture maps of a catchment from active microwave imagery. For this purpose, nine field trips are performed within a small basin in western Anatolia and point surface soil moisture values are collected with a Time Domain Reflectometer. The field studies are planned to match radar image acquisitions and accomplished over the water year of 2004 - 2005.

In this context, first, the Dubois Model, a semi-empirical backscatter model is utilized in the reverse order to develop radar backscatter – soil roughness relationship and soil roughness maps of the study area are obtained. Then another

relationship is built between radar backscatter and the three governing surface parameters: local incidence angle, soil moisture and soil roughness, which is later used in the soil moisture estimation methods. Depending on land use and vegetation cover condition, surface soil moisture maps of the catchment are produced by Backscatter Correction Factors, Water Cloud Model and Basin Indexes methods.

In the last part of the study, the soil moisture maps of the basin are input to a semi-distributed hydrological model, HEC-HMS, as the initial soil moisture condition of a flood event simulation. In order to investigate the contribution of distributed initial soil moisture data on model outputs, simulation of the same flood event is also performed with the lumped initial soil moisture condition. Finally, a comparison between both the distributed and lumped model simulation outputs and with the observed data is carried out.

Keywords: Soil Moisture, Surface Roughness, Synthetic Aperture Radar, Kurukavak Basin, Turkey

ÖZ

TOPRAK NEMİNİN AKTİF MİKRODALGA İLE UZAKTAN ALGILANMASI: KURUKAVAK HAVZASI UYGULAMASI

YILMAZ, Musa

Doktora, İnşaat Mühendisliği Bölümü

Tez Yöneticisi: Prof. Dr. Ali Ünal Şorman

Aralık 2008, 135 sayfa

Havzanın toprak nemi durumu, yağışın sızma ya da yüzey üstü akımına ayrışmasında önemli bir rol oynamaktadır, ve bu nedenle, fiziksel hidrolojik modellerin büyük çoğunluğunda anahtar bir değişkendir. Kuru toprak ve suyun dielektrik sabit değerleri arasında büyük fark bulunması sebebiyle mikrodalga uzaktan algılama (özellikle de yaygın olarak mevcut olan sentetik aperture radar) bu tür çalışmalar için oldukça önemli bir araçtır.

Bu çalışmanın esas amacı, hidrolojik bir modele girdi olarak kullanılabilen, dağılımlı havza toprak nemi haritalarının üretilmesidir. Bu amaçla, dokuz arazi çalışması gerçekleştirilmiş ve noktasal yüzey toprak nemi değerleri Time Domain Reflector cihazı ile toplanmıştır. Batı Anadolu'da küçük bir havzada gerçekleştirilmiş olan arazi çalışmaları, radar görüntü alımlarını yakalayacak şekilde planlanmış ve bir su yılı içinde tamamlanmıştır.

Bu doğrultuda, öncelikle bir geri yansımaya modeli olan Dubois Modeli, toprak yüzey pürüzlülüğü ile radar geri yansımaya değerleri arasında bir ilişki oluşturmak amacıyla

tersine kullanılmış ve çalışma havzasının toprak pürüzlülüğü haritaları elde edilmiştir. Daha sonra radar geri yansımaya değerleri ile en baskın üç yüzey parametresi; yüzey geri yansımaya açısı, toprak nemi ve toprak pürüzlülüğü, arasında bir ilişki elde edilmiş ve yüzey toprak neminin hesaplanması yöntemlerinde kullanılmıştır. Çalışma bölgesinin dağılımlı toprak nemi haritalarının çıkartılmasında havzanın arazi kullanım ve bitki örtüsü yoğunluğuna bağlı olarak; Geri Yansımaya Düzeltme Katsayıları, Su Bulutu Metodu ve Havza İndeksleri yöntemleri kullanılmıştır.

Çalışmanın son aşamasında, elde edilen dağılımlı toprak nemi haritaları, havzada gözlemlenen bir taşkın simülasyonu amacıyla, yarı dağılımlı bir hidrolojik modele başlangıç yüzey toprak nemi durumu olarak girilmiştir. Dağılımlı yüzey toprak nemi girdisinin hidrolojik model sonuçları üzerindeki katkısını incelemek amacı ile aynı taşkın simülasyonu tüm havza için sabit kalan başlangıç yüzey toprak nemi değeri ile de gerçekleştirilmiştir. Son olarak, elde edilen simülasyon sonuçları birbirleri ve de gözlenen sonuçlar ile karşılaştırılmıştır.

Anahtar Kelimeler: Toprak Nemi, Toprak Pürüzlülüğü, Sentetik Aperture Radar, Kurukavak Havzası, Türkiye

To those precious ones
who never gave up even if I did

ACKNOWLEDGMENTS

This study is funded by The Scientific and Technological Research Council of Turkey (TÜBİTAK). The active microwave remote sensing imagery of this work is provided by European Space Agency (ESA) through the joint collaboration between ESA and TÜBİTAK.

In this part of the study I would like to mention and thank the ones who will be always remembered with great respect.

My Family, being so far but always so close, for their endless support and patience, and for always believing in me,

My supervisor, Dr. Ali Ünal Şorman, for his guidance, incredible patience and for his invaluable support throughout the study,

Dr. Melih Yanmaz, for his never ending encouragement, for his precious advices and lifelong guidance, and for his invaluable support at all times,

Dr. Aynur Şensoy and Dr. Ali Arda Şorman, for always being there for me, for their never giving up nature, and for their amazing patience and continuous encouragement,

Günseli Akınç and Deniz Akınç, my little sisters, for their true love, for their heartwarming hugs and for always being just beside me,

Sir Onur Arı, for his true friendship, for his amazing support and for all the "brands" that I met with him,

İpek Neşe Şener, my blood sister, for always believing in me even if I did not, and for always being with me even if she is far far away.

TABLE OF CONTENTS

ABSTRACT	iv
ÖZ	vi
DEDICATION	viii
ACKNOWLEDGMENTS	ix
TABLE OF CONTENTS	xi
LIST OF TABLES	xiv
LIST OF FIGURES	xvi
CHAPTER	
1. INTRODUCTION	1
1.1. Introduction and Objectives	1
1.2. Thesis Outline	4
2. REMOTE SENSING OF SOIL MOISTURE	6
2.1. Remote Sensing	6
2.2. Microwave Remote Sensing	8
2.2.1. Side-Looking Radar	9
2.2.2. Radar Signal Characteristics	12
2.2.3. Radar Image Analysis	13
2.3. Remote Sensing of Soil Moisture	16
2.4. Soil Moisture Estimation Using SAR	18

3. STUDY AREA AND SOIL MOISTURE DATA	25
3.1. Study Area	25
3.2. Field Studies and Collection of Soil Moisture Data	27
3.3. Resampling of Point Soil Moisture Measurements	30
4. POST-PROCESSING OF RADAR IMAGERY	36
4.1. Synthetic Aperture Radar Data	36
4.2. Computation of Incidence and Local Incidence Angles	40
4.3. Derivation of Radar Backscatter Coefficients	45
5. SOIL SURFACE ROUGHNESS	49
5.1. Inversion of Dubois Model.....	49
5.2. Analysis of Computed Roughness Values	52
5.3. Backscatter – Soil Surface Roughness Relationship	55
6. SURFACE SOIL MOISTURE	59
6.1. Method I – Backscatter Correction Factors	60
6.2. Method II – Water Cloud Model	65
6.3. Method III – Basin Indexes	72
6.4. Mapping Surface Soil Moisture	76
7. LUMPED AND SEMI-DISTRIBUTED HYDROLOGICAL MODEL SIMULATION	83
7.1. Calibration of Model Parameters	85
7.2. Simulation Results	92
8. DISCUSSION OF RESULTS	98
9. RECOMMENDATIONS AND CONCLUSIONS	104
9.1. Recommendations	104
9.2. Conclusions	107
REFERENCES	109

APPENDICES	
A. SOIL SURFACE ROUGHNESS MAPS	115
B. SURFACE SOIL MOISTURE MAPS	118
C. OBSERVED VERSUS COMPUTED SURFACE SOIL MOISTURE VALUES	123
CURRICULUM VITAE	135

LIST OF TABLES

TABLES

Table 2.1	Radar band designations	12
Table 2.2	Rayleigh and Modified Rayleigh criteria	15
Table 3.1	Areal distribution of land use classes within the basin	27
Table 3.2	Land use class and number of points within measurement within nine plots	29
Table 3.3	Technical specifications of the TDR instrument	29
Table 3.4	Field study dates and measured average volumetric soil moisture values	31
Table 3.5	The number of original and resampled points for each plot	33
Table 3.6	Statistical parameters of the original TDR points	34
Table 3.7	Statistical parameters of the resampled points	35
Table 3.8	Percent change between the average, minimum and maximum values of soil moisture for original TDR and resampled points	35
Table 4.1	ASAR image properties	39
Table 4.2	Radar imagery acquired for the study area	40
Table 5.1	Summary of the parameters used in the roughness computation data sets	52
Table 5.2	Summary of data reduction for roughness values	54
Table 5.3	Selection of the threshold value for second level of reduction	55
Table 6.1	Summary of parameters used in the regression analyses	61

Table 6.2	Summary of the application of the soil moisture estimation methods	80
Table 7.1	Summary of the parameters used in the model simulations	94
Table 7.2	Comparison of simulation results with the observed values	95
Table C.1	Statistical parameters of the computed and observed soil moisture values for 09-Oct-2004	123
Table C.2	Statistical parameters of the computed and observed soil moisture values for 18-Dec-2004	126
Table C.3	Statistical parameters of the computed and observed soil moisture values for 07-May-2005	129
Table C.4	Statistical parameters of the computed and observed soil moisture values for 20-Aug-2005	132

LIST OF FIGURES

FIGURES

Figure 2.1	The electromagnetic spectrum	7
Figure 2.2	An electromagnetic wave	7
Figure 2.3	Operating principle of SLR systems	10
Figure 2.4	Geometry of radar data collection	11
Figure 2.5	Polarization modes	13
Figure 2.6	Root mean square roughness	14
Figure 3.1	Location, DEM and drainage network of the Kurukavak Basin	25
Figure 3.2	The RGB composite Quickbird image of the Kurukavak Basin	26
Figure 3.3	The land use map of the Kurukavak basin	27
Figure 3.4	Locations of soil moisture measurement plots within the basin	28
Figure 3.5	Time Domain Reflectometer (TDR)	29
Figure 3.6	A typical measurement with a TDR	30
Figure 3.7	Original and resampled point soil moisture locations in Plot 1	33
Figure 4.1	SAR image acquisition geometry of ERS-2	37
Figure 4.2	ASAR image acquisition geometry of ENVISAT	38
Figure 4.3	Georeferenced SAR image for 09-October-2004	41
Figure 4.4	The schematic representation of the parameters used in the computation of incidence angle at the i^{th} coordinate	42

Figure 4.5	Incidence Angle (α) grid of the 09-October-2004 dated SAR image	44
Figure 4.6	The schematic representation of the parameters used in the computation of the local incidence angle (θ_L)	45
Figure 4.7	The local Incidence Angle (θ_L) grid of the 09-October-2004 dated SAR image	46
Figure 4.8	The Backscatter grid of the 09-October-2004 dated SAR image	48
Figure 5.1	Frequency histogram of the computed roughness values ($n = 378$)	53
Figure 5.2	Frequency histogram of the computed delta values ($n = 378$)	54
Figure 5.3	Comparison of the soil surface roughness values obtained from the Data Sets I and II after 2 nd level of reduction	56
Figure 5.4	Backscatter – Roughness relationship for the Data Set I – SAR	57
Figure 5.5	Backscatter – Roughness relationship for the Data Set II – ASAR	58
Figure 6.1	Computed vs. observed backscatter values for the Data Set I-SAR	62
Figure 6.2	Computed vs. observed backscatter values for the Data Set II-ASAR	63
Figure 6.3	Corrected backscatter – observed soil moisture relationship for the Data Set I – SAR	64
Figure 6.4	Corrected backscatter – observed soil moisture relationship for the Data Set II – ASAR	65
Figure 6.5	The Normalized Difference Vegetation Index grid of the Kurukavak basin	68
Figure 6.6	Observed vs. computed (σ_{can}) canopy backscatter values from the WCM for the Data Set I-SAR	70
Figure 6.7	Observed vs. computed (σ_{can}) canopy backscatter values from the WCM for the Data Set II-ASAR	70
Figure 6.8	Relationship between delta ($\Delta\sigma$) and soil moisture (m_V) for the Data Set I-SAR	71

Figure 6.9	Relationship between delta ($\Delta\sigma$) and soil moisture (m_v) for the Data Set II-ASAR	72
Figure 6.10	Topographic Index (TI) grid of the Kurukavak basin	74
Figure 6.11	Solar Radiation Index (SRI) grid of the Kurukavak basin for 09-Oct-2004	76
Figure 6.12	Observed vs. computed soil moisture values for the Method III	77
Figure 6.13	Land use map of the Kurukavak basin with major classes (vector)	78
Figure 6.14	Land use map of the Kurukavak basin in permanent raster data model with cell centers as points	79
Figure 7.1	Illustration of exponential baseflow recession	88
Figure 7.2	Illustration of baseflow recession after peak	89
Figure 7.3	Schematic representation of flow direction	90
Figure 7.4	Schematic computation of flow travel length for 10 m cell size	90
Figure 7.5	Results of the Lumped model simulation	96
Figure 7.6	Results of the Distributed SAR model simulation	96
Figure 7.7	Results of the Distributed ASAR model simulation	97
Figure A.1	Soil surface roughness map and histogram for 09-Oct-2004	115
Figure A.2	Soil surface roughness map and histogram for 18-Dec-2004	116
Figure A.3	Soil surface roughness map and histogram for 20-Aug-200	117
Figure B.1	Soil moisture distribution of the Kurukavak basin for 09-Oct-2004 (SAR)	118
Figure B.2	Soil moisture distribution of the Kurukavak basin for 09-Oct-2004 (ASAR)	119
Figure B.3	Soil moisture distribution of the Kurukavak basin for 18-Dec-2004 (SAR)	119
Figure B.4	Soil moisture distribution of the Kurukavak basin for 18-Dec-2004 (ASAR)	120

Figure B.5	Soil moisture distribution of the Kurukavak basin for 07-May-2005 (SAR)	120
Figure B.6	Soil moisture distribution of the Kurukavak basin for 07-May-2005 (ASAR)	121
Figure B.7	Soil moisture distribution of the Kurukavak basin for 20-Aug-2005 (SAR)	121
Figure B.8	Soil moisture distribution of the Kurukavak basin for 20-Aug-2005 (ASAR)	122
Figure C.1	Frequency histograms of the computed and observed soil moisture values for the 09-Oct-2004 SAR image	124
Figure C.2	Frequency histograms of the computed and observed soil moisture values for the 09-Oct-2004 ASAR image ...	125
Figure C.3	Frequency histograms of the computed and observed soil moisture values for the 18-Dec-2004 SAR image	127
Figure C.4	Frequency histograms of the computed and observed soil moisture values for the 18-Dec-2004 ASAR image	128
Figure C.5	Frequency histograms of the computed and observed soil moisture values for the 07-May-2005 SAR image	130
Figure C.6	Frequency histograms of the computed and observed soil moisture values for the 07-May-2005ASAR image	131
Figure C.7	Frequency histograms of the computed and observed soil moisture values for the 20-Aug-2005 SAR image	133
Figure C.8	Frequency histograms of the computed and observed soil moisture values for the 20-Aug-2005 ASAR image ...	134

CHAPTER 1

INTRODUCTION

1.1. Introduction and Objectives

Soil moisture is the water held in the upper soil layer. Despite the fact that it constitutes a very small portion of the global water resources, soil moisture is an important surface variable for meteorology, agriculture, hydrology etc. In the field of hydrology, soil moisture controls the separation of rainfall into infiltration and surface runoff, and excess soil moisture could lead to high floods, whereas deficiency of it could lead to droughts.

Traditional methods of soil moisture measurements are limited to point values in which achieving higher temporal and spatial resolution of the variable could be labor intensive and costly. On the other hand, soil moisture maps of broader areas can be produced with remote sensing techniques at relatively lower costs. The remote sensing instruments which operate in the visible and infrared portions of the electromagnetic spectrum can provide limited information about variations in soil moisture. Due to the large difference in dielectric constants of dry soil and water, and sensitivity of the microwave region to surface dielectric properties, microwave remote sensing and particularly the commonly available synthetic aperture radar (SAR) is a potential tool for such studies. Moreover, microwave remote sensing has the advantages of penetrating clouds and independent of the sun as the source of illumination.

The main objective of this study is to obtain distributed soil moisture maps of a catchment with microwave remote sensing. It is also aimed that these maps are

coupled with a hydrological model as the initial soil moisture condition of the study basin prior to a rainfall-runoff event simulation. For this purpose, a small catchment in western Anatolia, Kurukavak basin, is selected as the study area. During 2004 – 2005 water year, nine field trips are performed within the basin and point soil moisture measurements are carried out on 68 locations with a Time Domain Reflectometer. The field studies are planned in advance to match radar image acquisitions.

Radar remote sensing of soil moisture in the Kurukavak basin is achieved through a number of objectives which will be described in this section of the study.

Since field measurements of soil surface roughness is not held during field studies, developing a relationship between radar backscatter and surface roughness is the first objective of this research. For this reason, the Dubois Model, a semi-empirical backscatter model is utilized in the reverse order to compute soil surface roughness values of the point soil moisture measurement locations. This is accomplished for the field study dates which have two radar image acquisitions and with sparse vegetation cover. Then, the developed relationship is used to compute roughness values of the catchment areas with similar surface conditions.

The second objective of the study is to develop an algorithm for retrieval of soil moisture from radar imagery for bare soil surfaces. First, the wet soil backscatter relationship is established between radar backscatter and three governing surface parameters; local incidence angle, soil moisture and soil roughness. After computing the incidence angle maps of the study area, the wet soil backscatter relationship is successfully developed and later utilized in the soil moisture estimation methods.

Depending on land use and vegetation cover condition, surface soil moisture distribution of the Kurukavak catchment is calculated by three methods. Similar to the analyses held with soil roughness, these methods are first developed with the point measurements of soil moisture and then applied to other areas of the study basin.

First, the Backscatter Correction Factors method, which does not include vegetation effect on radar backscatter, is built for bare or sparsely vegetated farmland and pasture fields of the basin. In this method, dry soil backscatter relationship, which is developed from the wet soil relationship with an assumption of dry soil condition, is utilized with a correction algorithm.

The third objective of this research is to propose an algorithm that would be used for microwave remote sensing of soil moisture on vegetation covered areas of the Kurukavak basin. For this reason, the second method of soil moisture estimation, a delta index approach is utilized with the Water Cloud Model for the farmland and pasture land use classes under dense vegetation cover condition.

Lastly, the third method of soil moisture estimation is developed and applied for the forested areas of the basin where radar remote sensing of soil moisture is impractical. The Basin Indexes method depends only on watershed terrain indexes of topographic index and solar radiation index. Finally, the three soil moisture estimation methods are used together to produce the soil moisture maps of the study catchment on four of the field study dates.

The last objective of the study is to integrate the distributed soil moisture maps of the basin with a semi-distributed hydrological model. During the field studies held in the Kurukavak basin, a rainfall and runoff measuring station is installed at the basin outlet which recorded a major flood event on 01-Jun-2005 with a peak discharge of $9.97 \text{ m}^3/\text{s}$. In the last part of the study, semi-distributed rainfall-runoff model simulations of this flood event are carried out with Hydrologic Engineering Center – Hydrologic Modeling System (HEC-HMS). In these analyses, the soil moisture maps of the Kurukavak catchment are input to the HEC-HMS model as the initial soil moisture condition of the watershed at the beginning of the simulation period. In order to question the contribution of distributed initial soil moisture data on model results, simulation of the same flood event is also performed by assuming a lumped initial soil moisture condition for the entire basin. Finally, the distributed and lumped model simulation results are compared with the observed flood event.

1.2. Thesis Outline

The structure of this thesis closely follows the order in which the work is undertaken in response to the objectives and consists of eight further chapters.

Chapter 2 outlines the fundamental principles of microwave remote sensing and discusses the application of it for soil moisture retrieval. It also reviews the aspects and previous research on remote sensing of soil moisture.

Chapter 3 introduces the field study catchment. It summarizes the soil moisture data collection with Time Domain Reflectometer and details the post processing analyses performed with the collected data. The permanent raster data model, which is used to integrate point measurements with raster data sets, is also outlined in this chapter.

Chapter 4 describes the radar imagery utilized in this work. First, the geometrical and optical properties of the acquired images are presented. Then, details of producing radar backscatter coefficients and incidence angle maps from these images are discussed in detail.

Chapter 5 details the application and results of the methodology carried out for soil surface roughness mapping of the study area. The semi-empirical Dubois model and inversion of the model is discussed in this chapter. Lastly, the relationship established between radar backscatter and soil surface roughness is outlined.

Chapter 6 describes the three methodologies developed and used for surface soil moisture mapping of the Kurukavak catchment. First, background and application of the Backscatter Corrections Factors method, which is used for bare or sparsely vegetated farmland and pasture fields, is discussed. Then, theory and application of the Water Cloud Model that is applied for the densely vegetated farmland and pasture areas is detailed. The Basin Indexes method, which does not incorporate radar imagery, is the third method of the study and application details of it for the forest land use class of the catchment is presented as well. Finally, coupling of these

methods for producing surface soil moisture maps of the Kurukavak basin is discussed.

Chapter 7 outlines the procedures carried out for the rainfall-runoff model simulation of the 01-June-2005 flood event. First, a detailed discussion about model parameters and calibration procedure is given in this chapter. Then, the simulations performed for distributed and lumped initial soil moisture conditions are presented with a comparison between the outcomes of the two conditions.

Chapter 8 presents a detailed discussion about all aspects of the study. Finally, recommendations for future studies and concluding remarks are given in Chapter 9.

CHAPTER 2

REMOTE SENSING OF SOIL MOISTURE

2.1. Remote Sensing

Remote sensing is the science of obtaining information about an object through the analysis of data acquired by a device that is not in contact with the object. Reading could be the best example for remote sensing, in which the object is the words on the paper, eyes are the device that determines the black and white areas of the page, and brain is processing this data to form knowledge (Lilesand and Kiefer, 1999).

According to this concept, many instruments and methods of observations could be accepted as remote sensing, but one of the major goals of this science is to investigate broader areas beyond the sight of human eye, which necessitates utilizing space satellites or planes for the process of sensing. Moreover, among many types of sensors collecting remote data, light or electromagnetic sensors are the key instruments of remote sensing.

In remote sensing, electromagnetic waves are categorized by their wave lengths within the electromagnetic spectrum (Figure 2.1). Similar to the radio waves or X-rays, the visible light is one of the forms of the electromagnetic energy. This energy radiates in accordance with the basic wave theory; traveling in a harmonic, sinusoidal way with the speed of light (Figure 2.2). Although certain regions of the spectrum are assigned with known names, there is no clear boundary between these regions.

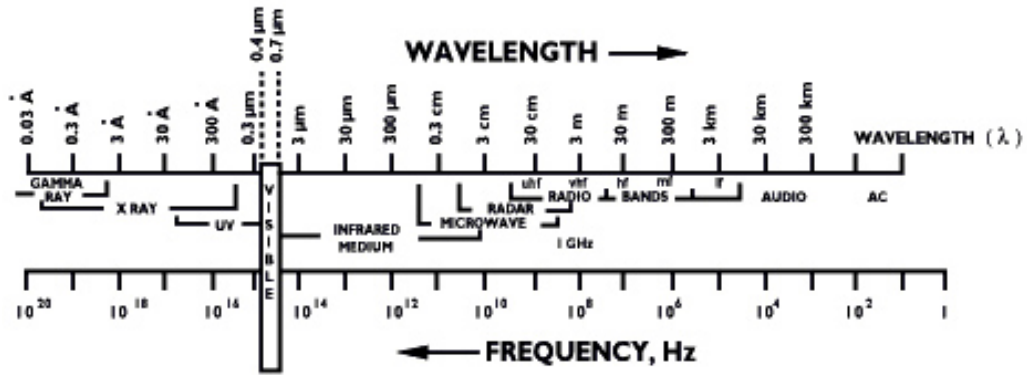


Figure 2.1. The electromagnetic spectrum

The basic characteristics of a digital remote sensing data are similar to photography. The data are actually a two dimensional array of discrete picture elements or pixels (Lillesand and Kiefer, 1999). The value of each pixel represents the average brightness or radiance measured over the ground area corresponding to that pixel. The pixel values, or Digital Numbers (DN), are positive integer values that result from quantizing the original electrical signal to numeric values. In a typical remote sensing image the DN values are recorded over such scales; 0 to 255, 0 to 511, etc. These ranges represent the set of integers that can be recorded using 8 and 9 bit computer scales, respectively.

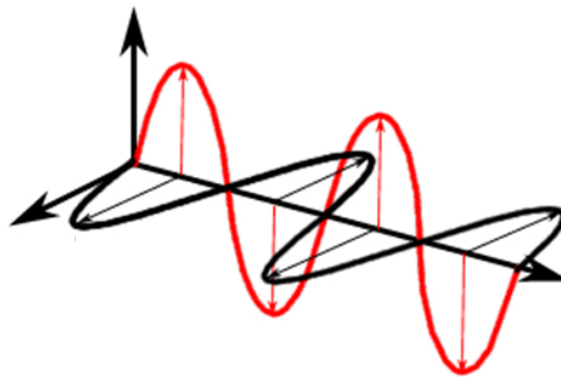


Figure 2.2. An electromagnetic wave

The sensors used in remote sensing of the earth can be categorized into two distinct groups according to their source of electromagnetic energy. The *passive* sensors require external energy sources, such as sun. Similar to the human eye or photographic films, these sensors generally record the reflected solar energy or the naturally available energy. On the other hand, *active* sensors have their own source of energy. Like a camera utilizing flash, these sensors transmit their own electromagnetic energy and hence record the reflected amount of the previously transmitted energy.

First remote sensing satellite systems were generally designed to work within the visible band of the electromagnetic spectrum with a single sensor. Similar to major passive systems, these satellites were located on a sun-synchronous orbit, in which the satellite always passes over the sun-illuminated part of the earth. But in the last decades with the development in technology and increasing need for better imaging systems, today's satellite platforms are occupied with more than one sensor, acquiring data on a wider range of the spectrum.

2.2. Microwave Remote Sensing

Remote sensing of the earth by utilizing the sensors working within the microwave portion of the electromagnetic spectrum is known as microwave (MW) remote sensing. This portion includes wavelengths within a range of 1 mm to 1 m approximately. There are two distinct features of microwave remote sensing among the remote sensing point of view:

- Microwaves can penetrate atmosphere under almost all conditions. Different from sensors working within the visible bands, images acquired by MW sensors are free of clouds, haze, smoke, etc.
- Reflection and emission characteristics of the earth materials under MWs have no direct relationship to their similar characteristics under electromagnetic energy from thermal or visible bands (Lilesand and Kiefer, 1999).

Similar to other remote sensing systems, MW sensors can be both *airborne* (mounted on a plane) and *spaceborne* (mounted on a satellite platform). Moreover the source of illumination is the main distinction for MW systems. *Radar* (Radio Detection and Ranging) is an example of the active MW systems, which have its own source of illumination (or energy). On the other hand, the passive sensors, which are referred as microwave *radiometers*, respond to the low level of reflected and emitted MW energy originating from the object. For the radiometer, the transmission source is the target itself, and the radiometer acts passively as a receiver (Ulaby et al., 1981a).

2.2.1. Side-Looking Radar

Radar was first developed and used for detection of location and orientation (with respect to the radar) of objects by using radio waves. The working principles of all radar systems start with sending small pulses of electromagnetic energy in the direction of interest and then recording the strength and origin of the echoes (reflections) received from the objects (Lilesand and Kiefer, 1999).

The most known radar systems are the ones used for air traffic and weather forecasting. These systems are called as plan position type, have a 360° rotating antenna and displaying the plan view (map like view) of the objects within the radar range. However, this type of radar systems is not suitable for common remote sensing applications due to their rather poor spatial resolution (Lilesand and Kiefer, 1999).

Radar systems used for remote sensing applications fall within three categories: imaging radars, scatterometers and altimeters. Majority of the remote sensing applications require imaging radars, but specialized applications use scatterometers and altimeters (Ulaby et al., 1981a).

Most imaging radars used for remote sensing are Side-Looking Radars (SLR), which were first developed for military purposes in the late 1940s (Ulaby et al., 1981a). SLR (or SLAR) is a system that utilizes an antenna which is fixed below the aircraft

and pointed to the side. The basic operating principles of a SLR system are shown in Figure 2.3 (Lilesand and Kiefer, 1999). MW energy is transmitted from the radar antenna by means of small pulses which propagate in the air with the speed of light and according to the wave theory. As described in Figure 2.3, the pulse will reach to the house at the 7th time and reach to the tree at the 9th time, but return echoes will return to the antenna at the 13th and 17th times, respectively. Since the house is more reflective than the tree, a stronger response is recorded by the radar sensor. After processing of all sent and received signals, intensity of the response is reflected as the objects DN value and return time of pulse is reflected as the distance of the object from the sensor (Ulaby et al., 1981a).

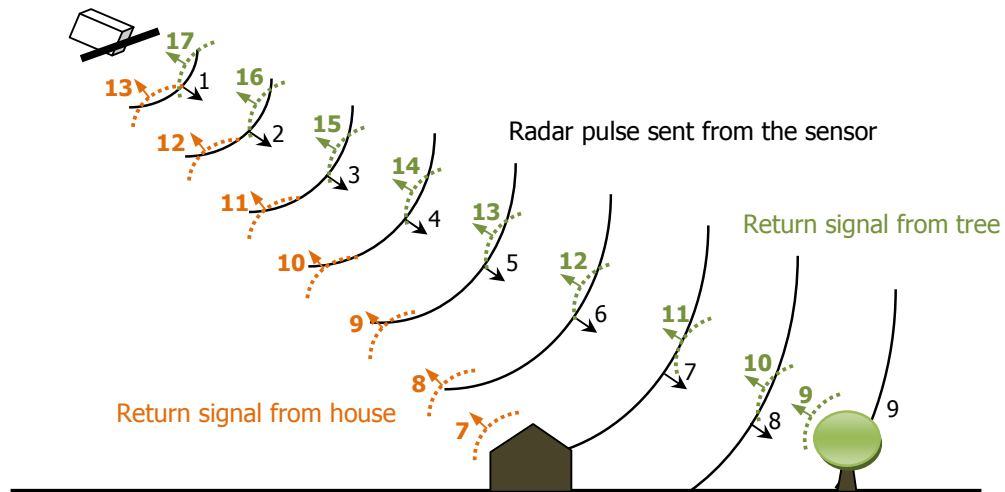


Figure 2.3. Operating principle of SLR systems (Lilesand and Kiefer 1999)

Due to their side looking nature, remote sensing radar systems have a totally different geometry from the other remote sensing systems. Figure 2.4 illustrates the system of names typically used for describing radar data acquisition. As shown in Figure 2.4, the incident angle (or its synonym *incidence angle*) is the angle between the radar beam and the normal to the earth surface at the point of incidence. In this figure, nadir refers to the point which is directly beneath the sensor.

The ground resolution of a SLR system is defined by two parameters: pulse length and antenna beamwidth (β). The pulse length of the radar signal is determined by

the interval of the time that the antenna emits its electromagnetic energy and it defines the ground resolution in the range direction (perpendicular to flight direction). On the other hand, the width of the antenna beam determines the ground resolution in the flight (azimuth) direction (Lilesand and Kiefer, 1999).

In MW remote sensing systems the radar beamwidth is controlled by;

a) The physical (actual) length of the antenna. This type of system is called as Real Aperture Radar and it is hard to obtain small β values.

b) Synthesizing a virtual antenna length which makes it possible to have smaller beamwidths and it is called as Synthetic Aperture Radar (SAR) (Lilesand and Kiefer, 1999). The SAR system has a major advantage over the real-aperture system that the resolution of the image in the flight direction is independent of the distance between the target and the radar (Ulaby et al., 1981a).

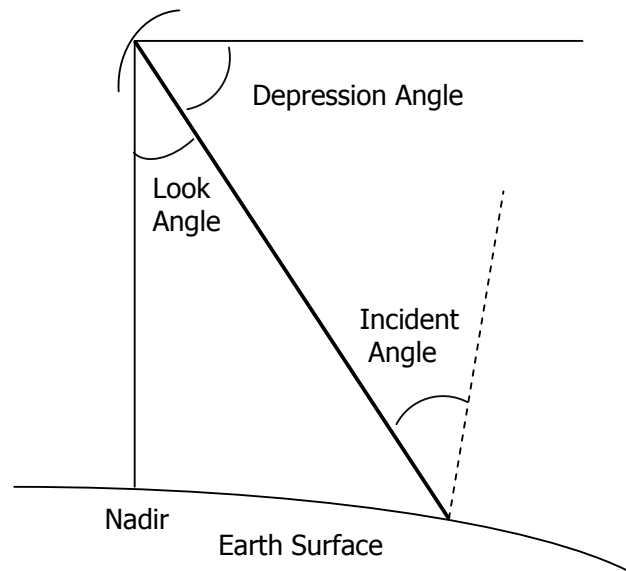


Figure 2.4. Geometry of radar data collection

Although they have narrow effective antenna beamwidths (higher spatial resolution), the Synthetic Aperture Radars (SARs) has a physically short antenna.

However, by utilizing a modified data recording and processing technique, they synthesize the effect of a very long antenna. This is achieved by a method called as Doppler Beam Sharpening (Lilesand and Kiefer, 1999).

2.2.2. Radar Signal Characteristics

The two primary factors affecting the transmission characteristics of the signals from any radar system are the wavelength and the polarization of the energy pulse used in the system (Lilesand and Kiefer, 1999). During the early stages of radar development letter codes (K, X, L, etc) were assigned to certain bands of the microwave portion due to military security reasons. These arbitrarily assigned band names are continued to use as a matter of convenience. These representations of the MW bands with their respective wavelengths are given in Table 2.1.

Table 2.1. Radar band designations (Lilesand and Kiefer, 1999)

Band Name	Wavelength (λ) (cm)
K _a	0.75 - 1.1
K	1.1 - 1.67
K _u	1.67 - 2.4
X	2.4 - 3.75
C	3.75 - 7.5
S	7.5 - 15
L	15 - 30
P	30 - 100

In the electromagnetic wave theory, polarization describes the direction of light wave oscillations. Independent of its wavelength, in MW systems radar signals can be transmitted and/or received in different modes of polarization. The signal can be filtered in such a way that its electrical wave vibrations are restricted to a single plane. A radar signal can be transmitted in either Horizontal (H) or Vertical (V) plane. Similarly, it can be received on either a horizontal or a vertical plane. As a result, there exist four different combinations of signal transmission and reception: H send H receive or HH, H send V receive or HV, VV and VH (Lilesand and Kiefer,

1999). Figure 2.5 illustrates the vertical and horizontal polarizations of electromagnetic waves.

2.2.3. Radar Image Analysis

Side-looking radar image analysis has been successful in many fields of applications: mapping geological structures and vegetations, determining sea ice types, etc. Because of its side-lighted characteristic, radar images resemble aerial photography taken under low sun angle conditions (Lilesand and Kiefer, 1999). In the radar terminology and MW literature, *backscatter* is frequently mentioned. From the physics point of view, backscatter is the reflection of waves, particles, or signals back to the direction where they came from. In other terms, it represents the amount of the returning radar pulses to the antenna. MW sensors measure the amount of backscatter as the intensity of the returning electromagnetic energy and it is commonly referred in the units of decibels (dB).

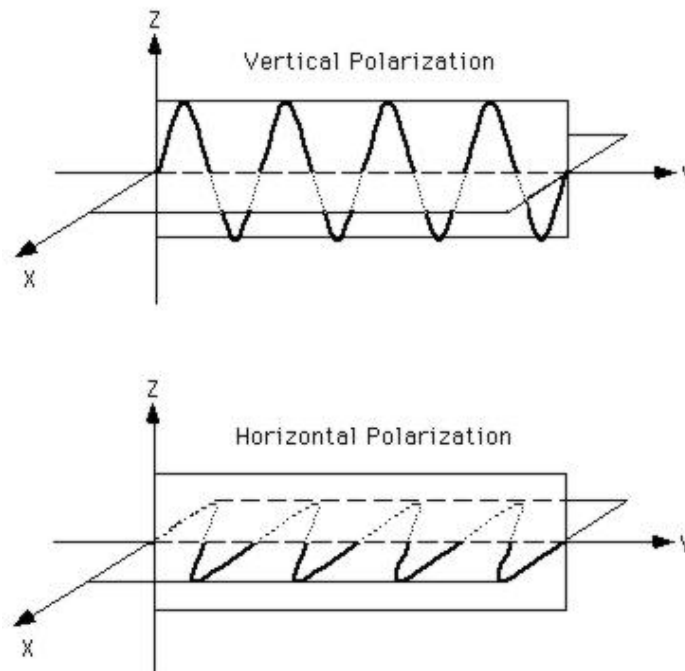


Figure 2.5. Polarization modes

In radar imagery, intensity of backscatter depends on;

- a) *target parameters*: geometric and electrical characteristics of the surface; roughness, moisture, incidence angle.
- b) *sensor parameters*: wavelength, polarization, incidence angle (Sahebi et al., 2002).

Soil Surface Roughness

Soil surface roughness is one of the surface geometric characteristics which has a dominant effect on radar backscatter, intensity of the return signals. In general terms, roughness is a measurement of the small-scale variations in the height of a physical surface. From radar remote sensing point of view, a surface is called as *rough* if it scatters the incoming radar energy in all directions and returns a significant portion back to the antenna. Consequently, a surface is called as *smooth* if it reflects most of the energy away from the antenna (Lilesand and Kiefer, 1999).

Surface roughness is usually described by two parameters: *standard deviation of surface height* (***h***) and *correlation length* (***c***) (Ulaby et al., 1981b). The first roughness parameter is also referred as *root mean square height of surface variations* (Sahebi et al., 2002) or simply *root mean square roughness* and represents the amount of deviations observed over the soil surface from the reference/mean surface. As illustrated in the Figure 2.6, the root mean square roughness, ***h***, is obtained by measuring the surface variations (***r_i***) from the reference/mean surface (shown with the dotted line) along a sampling length of ***L***.

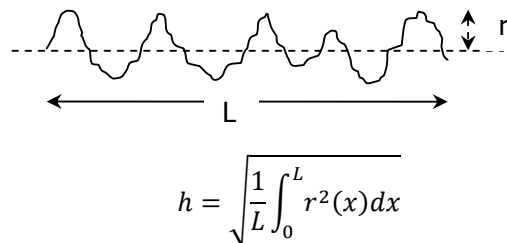


Figure 2.6. Root mean square roughness

The second roughness parameter, the correlation length (c) provides a reference for estimating the statistical independence of two points over a surface. If the two points are separated by a horizontal distance greater than c , then their heights may be considered to be statistically independent of one another (Ulaby et al., 1981b).

In this study, since no field measurement of roughness parameters are available, inversion of the semi-empirical Dubois backscatter model (Dubois et. al., 1995), which has a single roughness parameter (root mean square of surface heights; h), is utilized for computation of soil surface roughness on bare fields of the study catchment. The detailed discussion about the Dubois model is given in Chapter 5 of this thesis.

According to the incoming signal wavelength, the surface acts as rough or smooth. Since MW wavelengths vary from 1 cm to 100 cm approximately, a surface which acts as rough in L band may act as smooth in K band. Rayleigh criterion or its modified version (Table 2.2) is generally used to determine surface behavior (rough or smooth) for a specific MW sensor.

Table 2.2. Rayleigh and Modified Rayleigh criterions (Sabins, 1997)

<i>Rayleigh Criteria</i>		<i>Modified Rayleigh Criteria</i>	
$h > \frac{\lambda/8}{\cos(\theta_L)}$	Rough	$h > \frac{\lambda/4}{\cos(\theta_L)}$	Rough
			Intermediate
otherwise	Smooth	$h < \frac{\lambda/25}{\cos(\theta_L)}$	Smooth

λ : wavelength, θ_L : Local incidence angle

Vegetation

Similar to soil surface roughness, vegetation cover of the target area has a significant effect on the radar backscatter. Similarly, as the density of the vegetation canopy increases, amount of scattering also increases. As a general rule, strong volume backscatter will be expected when mean vegetation size is equal to the radar wavelength. It is also possible to investigate vegetation by using radar imagery. For this purpose, using small wavelengths is more suitable for sensing crops and trees, on the other hand, larger wavelengths are used for sensing trunks and limbs. Moreover, vegetation with higher moisture content returns more signals than that with lower moisture content (Lilesand and Kiefer, 1999).

Electrical Characteristics

Similar to the geometric characteristics, the electrical characteristics of surface features have the same strong effect on radar backscatter. One of the measures of an object's electrical characteristics is the complex dielectric constant (DC) which is a fundamental property that characterizes both the reflection and the attenuation properties of a wave interacting with that material (Ulaby et al., 1996). In the MW region of the electromagnetic spectrum, most natural materials have a dielectric constant within the range of 3 to 8 when dry. On the other hand, water has a dielectric constant of 80 and hence the presence of moisture in soil or vegetation increases the radar reflectivity significantly. In fact, a change in radar backscatter is often related to changes in moisture content much more than changes from one material to another. Since the dielectric constant of water is at least 10 times greater than that of dry soil, the presence of moisture in the top few centimeters of bare soil can be detected by radar imagery (Lilesand and Kiefer, 1999).

2.3. Remote Sensing of Soil Moisture

Soil moisture refers to the water stored in the pores of the soils. It is the key parameter controlling the separation of rainfall into infiltration and surface runoff. Soil moisture content also has a limiting effect on evaporation and transpiration and

no need to mention but it is crucial for plant growth (Wagner et al., 2003). Accordingly, several methodologies have been developed to generate soil moisture information. For small scale studies direct; such as neutron probes and Time Domain Reflectometer (TDR), and indirect measurements; such as gravimetric, are performed. However, methodologies involving remote sensing techniques are developed for local and regional scale studies (Ceballos et al., 2005).

Initial soil moisture condition of a watershed is significant for almost all hydrological simulation models. Considering such watershed scale applications, obtaining point measurements of soil moisture would be sufficient only up to a certain level. On the other hand, remote sensing of soil moisture would enable us to estimate the initial wetness condition of the basin in a distributed manner. From this point forward, optical and microwave remote sensing of soil moisture is summarized with their advantages and limitations.

Visible and InfraRed Reflectance

The spectral information obtained from visible, near infrared and shortwave infrared wavelengths is related to soil moisture as a function of spectral absorption characteristic of the surface. For example, an increase in soil moisture generally leads to a decrease in soil reflectance for bare soils. Even if there are many sensors available for these wavelengths with fine spatial resolution, their relation to moisture content is weak. Moreover, inability to penetrate clouds and being strongly affected by vegetation are the other limitations (Moran et al., 2004).

Thermal Infrared Radiation

Estimation of soil moisture using remotely sensed thermal wavelengths is mainly related to the use of radiative temperature measurements. Available moisture in soil directly influences soil temperature by increasing both specific heat and thermal conductivity (Moran et al., 2004). As a result, variation in surface thermal radiation is primarily due to varying moisture content for bare soils (Friedl and Davis, 1994). Similar to visible bands, a number of sensor having high spatial resolution and broad

coverage are available, but studies utilizing these type of sensors also suffer from cloud and vegetation cover (Moran et al., 2004).

Passive Microwave Radiation

Due to the large differences in dielectric constant of dry soil and water, intensity of microwave radiation from soil is related to its moisture content for bare soils. Advantages of using these sensors are both their insensitiveness to cloud cover and their strong relationship to moisture content. On the other hand, strong influences of roughness and vegetation on these sensors are the major limitations (Moran et al., 2004).

Active Microwave (Radar)

Similar to passive MW sensors, the radar backscatter is highly correlated with the available soil moisture content. Moreover, they share the common advantages of cloud penetration and surface penetration up to almost 5 cm. Active MW imagery is also highly disturbed by surface roughness and vegetation cover. But major advantage of these sensors is that they acquire finer resolution imagery than passive microwave sensors (Moran et al., 2004).

2.4. Soil Moisture Estimation Using SAR

The only satellites that can currently meet the spatial resolution and coverage requirements of watershed scale applications are the active microwave sensors. Moreover, the most common active MW instrument is the Synthetic Aperture Radar (SAR) systems (Moran et al., 2004). This section of the study covers a brief review of the literature by grouping similar methodologies developed for soil moisture sensing with SAR.

Semi-empirical Approaches

According to Ulaby et al. (1996) there are three major contributors of the radar backscatter from a vegetated surface (σ^0).

$$\sigma^0 = \tau^2 \sigma_{soil}^0 + \sigma_{vegetation}^0 + \sigma_{veg+soil}^0 \quad (2.1)$$

in which;

σ_{soil}^0 is the backscatter contribution of the bare soil

τ^2 is the two-way attenuation of the vegetation layer

$\sigma_{vegetation}^0$ is the direct backscatter contribution of the vegetation layer

$\sigma_{veg+soil}^0$ represents the multiple scattering involving the vegetation and ground surface

For surfaces having high vegetation cover, τ^2 is almost 0 and hence backscatter is primarily determined by the scattering from the vegetation canopy. On the other hand, for sparsely vegetated areas, τ^2 is close to 1, and, the second and third terms of Equation 2.1 are negligible. In that case, radar backscatter is determined by soil roughness and moisture content (Engman and Chauhan, 1995).

This method utilizes a two step algorithm; first vegetation backscatter is eliminated and then the relation between moisture content and backscatter is estimated by assuming a constant offset value due to roughness. Schneider and Oppelt (1998) have proposed the Equation 2.2,

$$m_s = a + b\sigma_s^0 \quad (2.2)$$

in which;

m_s is the moisture content,

a and b are constants,

σ_s^0 is the radar backscatter.

a and b in Equation 2.2 are linear regression coefficients determined primarily by field experiments. The major disadvantage of Equation 2.2 is that it is valid only for a certain type of sensor, land use and soil type, and, for areas when $\tau^2, \sigma_{vegetation}^0$ and $\sigma_{veg+soil}^0$ are known or negligible (Moran et al., 2004).

For a semiarid watershed in Arizona, the difference between dry and wet season SAR backscatter values are utilized to normalize the effects of roughness and topography. This method requires the images be acquired with exactly the same sensor type and configuration. In that study, effect of sparse vegetation is found to be negligible (Moran et al., 2000).

An important disadvantage of semi empirical approaches is that sensitivity of radar backscatter to surface roughness can be much greater than the sensitivity of it to moisture content (Moran et al., 2004).

SAR used for change detection

This approach uses multipass SAR imagery to determine variations in the moisture content by assuming that the temporal variation of roughness and vegetation is at a larger scale than that of moisture content (Moran et al., 2004). During the time elapsed between two SAR images, it is assumed that there is relatively high change in moisture content but almost no change in roughness and vegetation conditions. It should be noted that this assumption is not valid for cultivated crops where roughness and vegetation changes significantly over short time periods (Moran et al., 2004). As a simple application, a normalized radar backscatter soil moisture index (NBMI) was derived over a site from two images acquired at two different times (t_1 and t_2) (Shoshany et al., 2000).

$$NBMI = \frac{\sigma_{t_1}^0 + \sigma_{t_2}^0}{\sigma_{t_1}^0 - \sigma_{t_2}^0} \quad (2.3)$$

Moreover, by using relatively long record of SAR images, it is also possible to correlate changes in backscatter with changes in moisture content. In a study by

Wickel et al. (2001), 10 radar scenes over a month period are acquired for an agricultural site in Oklahoma. After eliminating fields having high temporal variation of roughness, a strong correlation of 0.89 is calculated between backscatter and moisture content.

SAR Data Fusion Approach

This group of methods involves studies that integrate SAR images with other remote sensing images, such as optical and passive microwave. Majority of these techniques have addressed the information independency and interchangeability of integration of active and passive, and, active and optical remote sensing systems (Moran et al., 2004).

The greatest advantage of active MW systems over passive sensors is the fine spatial resolution, where SAR resolution is in terms of tens of meters while passive MW resolution is in terms of tens of kilometers. However, both of them appear to have similar sensitiveness to soil moisture and near-similar sensitiveness to roughness (Chauhan et al., 1999, Du et al. 2000). Data fusion of passive and active MW sensing has a general form of using SAR backscatter for determining fine resolution vegetation and roughness parameters and then combining these with coarse resolution passive MW radiance for estimating soil moisture (Moran et al., 2004).

The methods of microwave and optical remote sensing have been separately used for the estimation of surface properties. There are several studies that have focused on the similarities between optical and SAR data. The SAR bands having longer wavelengths (> 6 cm) are being related to thermal measurements and for vegetated areas shorter SAR bands are related to optical vegetation indices (Moran et al., 1997).

SAR and Microwave Scattering Models

The continuing researches on estimating the effects of roughness, vegetation and moisture content on radar backscatter have led to the use of physically based scattering models. These models generally predict the radar backscatter as a function of sensor and surface conditions, and hence can be used backwards to estimate soil moisture content. For this purpose, empirical, semi-empirical and theoretical models have been developed (Moran et al., 2004).

Empirical models are usually based on experimental data and may only be applicable to the surface and sensor conditions of the experiment. In order to overcome this limitation, semi-empirical models, which have theoretical background and include model parameters obtained from experiments, have been developed. An example for this type is the Water Cloud Model (WCM) which represents the vegetation as a uniform cloud of spherical droplets (Attema and Ulaby, 1978).

Moreover, the Integral Equation Model (IEM) (Fung et al., 1992) is a physically based radiative transfer model, which is developed for calculating radar backscatter from a randomly rough dielectric surface. Since IEM has combined Kirchhoff and small perturbation theories to address a wide range of roughness conditions, it is one of the most widely used scattering models (Moran et al. 2004).

The parameters used in the IEM are;

- a) radar incidence angle (θ),
- b) surface roughness;
 - i) standard deviation of surface heights (h)
 - ii) surface correlation length (c)
- d) dielectric constant of the soil (ϵ), (Bindlish and Barros, 2000).

The IEM has been found to be particularly suitable for retrieving soil moisture content from single type SAR backscatter values. Generally, for this type of application a prior knowledge of surface roughness is required to calculate moisture

values from the radar imagery. It also led to a number of methods for computation of distributed roughness parameters from orbiting SAR sensors (Moran et al., 2004). Known as IEM inversion algorithm, this technique requires the information of point moisture measurements and corresponding backscatter values for a number of locations, and is utilized to obtain point roughness values. One such methodology is developed by Bindlish and Barros (2000), where an iterative schema is applied to eliminate the two unknown surface roughness parameters from the observed backscatter values. After obtaining the surface parameters from the inversion algorithm, the IEM can be used in the forward direction to calculate the moisture values from radar backscatter.

Baghdadi et al. (2002a) have improved moisture estimates through IEM inversion technique on multi incident angle SAR imagery. In another study, Baghdadi et al. (2002b) proposed empirical relations between several IEM parameters for the improvement of IEM inversion technique. In addition, Rahman et al. (2008) utilized multi-angle radar imagery for roughness and soil moisture estimation and found these parameters with good accuracy at the watershed scale. Moreover, Verhoest et al. (2000) used multi temporal data to determine an effective roughness parameter. In another study (Sahebi et al., 2002), an index very similar to Equation 2.3 is proposed as Normalized Radar Backscatter Roughness Index (NBRI). The NBRI is determined from Equation 2.4, in which subscripts 1 and 2 represent two different incidence angle conditions. This index is tested by comparing simulated (Geometric Optics Model) and observed (RADARSAT) data and correlation coefficients of 0.83 and 0.95 were found, respectively.

$$NBRI = \frac{\sigma_1^0 + \sigma_2^0}{\sigma_1^0 - \sigma_2^0} \quad (2.4)$$

There have been several other improvements and additions to the IEM that would increase the use of it for moisture retrieval. In order to reduce the complexity of IEM, algorithms based on numerical simulation of IEM for a range of roughness and moisture conditions have been developed. Chen et al. (1995) have utilized the IEM to generate backscatter values for a range of incidence angle, roughness and

moisture conditions. Then these values are used as a look-up table of the IEM from which backscatter and moisture values are related to each other on a theoretical basis. Similar studies were also performed by Shi et al. (1997) and van Oevelen and Hoekman (1999). These simplified IEM algorithms require fewer parameters and are easier to use with remote sensing data (Moran et al., 2004).

Integration of vegetation backscatter effect into the IEM inversion algorithm is another important improvement of the IEM methodology. Even if it has successful applications for sparsely vegetated areas, the original IEM algorithm was developed for bare soil conditions (Moran et al. 2004). Bindlish and Barros (2001) have formulated an IEM vegetation scattering method in the framework of water cloud model (WCM). They reported that the modified IEM algorithm led to a significant improvement in the correlation coefficients between ground measured and SAR derived moisture values.

CHAPTER 3

STUDY AREA AND SOIL MOISTURE DATA

3.1. Study Area

Kurukavak basin, which is a small catchment located within the Bilecik province of Turkey, is selected as the study area of this research. The basin covers an area of 4.73 km² and it is one of the subbasins of the Sakarya River. The Digital Elevation Model (DEM), which is obtained from 1/25000 scaled contour maps of the area, and drainage network map of the basin are presented in Figure 3.1. The maximum and minimum elevations of the basin are 1080 m and 840 m, respectively. Kurukavak Basin is one of the pilot basins of General Directorate of Agricultural Research of Turkey. The directorate has been collecting rainfall and runoff data within the basin since 1984.

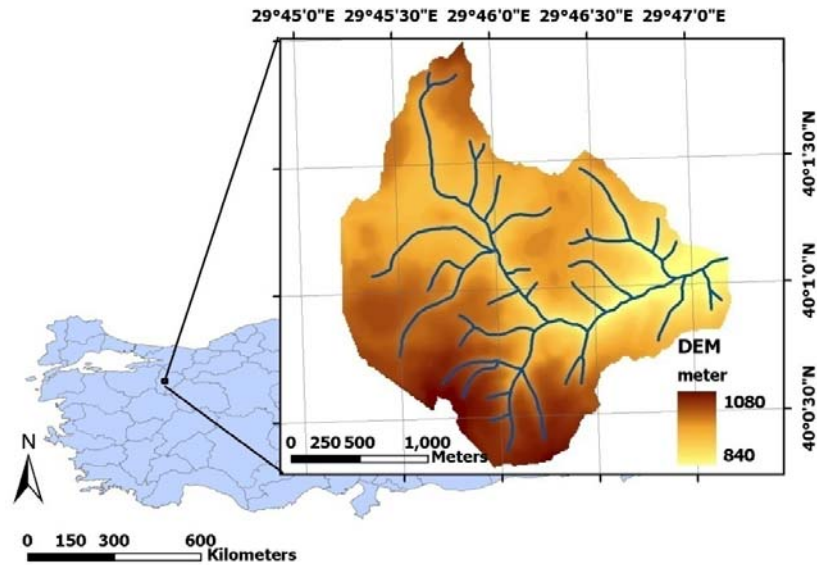


Figure 3.1. Location, DEM and drainage network of the Kurukavak Basin

In order to obtain an up-to-date land use map and vegetation index of the study site, a high resolution satellite image of the area has been acquired by Quickbird satellite. This image is composed of four spectral bands, which are Blue (B: 450 – 520 nm), Green (G: 520 – 600 nm), Red (R: 630 – 690 nm), and Near InfraRed (NIR: 760 – 900 nm), and has a ground resolution of 0.60 meters. The date of the acquisition is 6th of May of 2006 and the RGB composite of the image is presented in Figure 3.2. The land use map of the basin, which is digitized from the Quickbird image, is also shown in Figure 3.3.

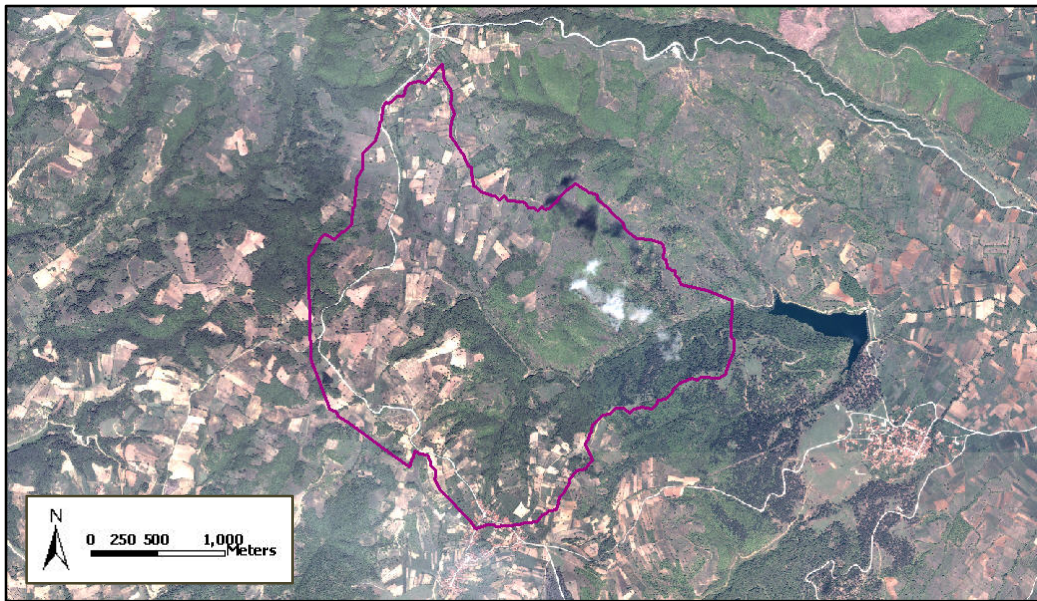


Figure 3.2. The RGB composite Quickbird image of the Kurukavak Basin

After obtaining the land use map of the study site, areal distribution of the land use classes is computed in percentages and square kilometers (Table 3.1). It is observed from Table 3.1 that about half of the basin is covered with forest and the rest of the area is almost shared with two land use classes; farmland and pasture.

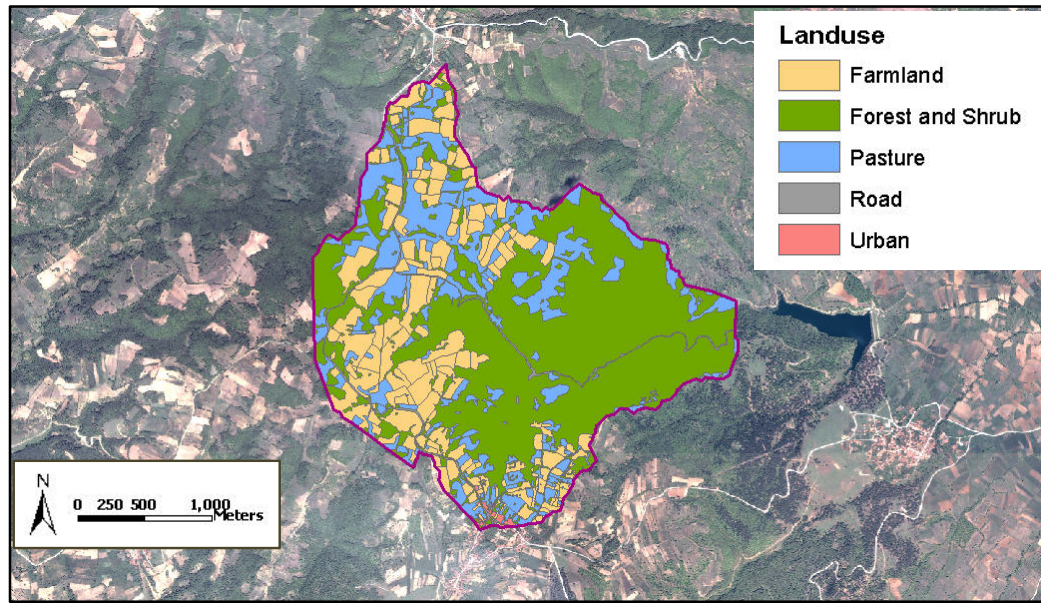


Figure 3.3. The land use map of the Kurukavak basin

Table 3.1. Areal distribution of the land use classes within the basin

Land use	Area (km ²)	Area (%)
Farmland	1.12	23.6
Pasture	1.03	21.9
Forest	2.51	53.1
Other	0.07	1.4

3.2. Field Studies and Collection of Soil Moisture Data

Between September 2004 and August 2005, a total of nine field trips were carried out within the basin for collecting soil moisture data. The volumetric soil moisture values were measured with a Time Domain Reflectometer at the previously selected 68 stationary points which were grouped within 9 plots. Since radar waves could not penetrate through dense vegetation canopy such as forest, these measurement locations are selected over farmland and pasture fields of the basin. In addition to land use maps, the topographic index (discussed in Chapter 6.3) map of the basin is

also considered in selection of the plot locations. The geographic locations of these measurement plots are presented in Figure 3.4, and, land use classes and number of measurement points within each plot is tabulated in Table 3.2. The selection criteria for location and number of points are discussed in section 3.3 of this chapter.

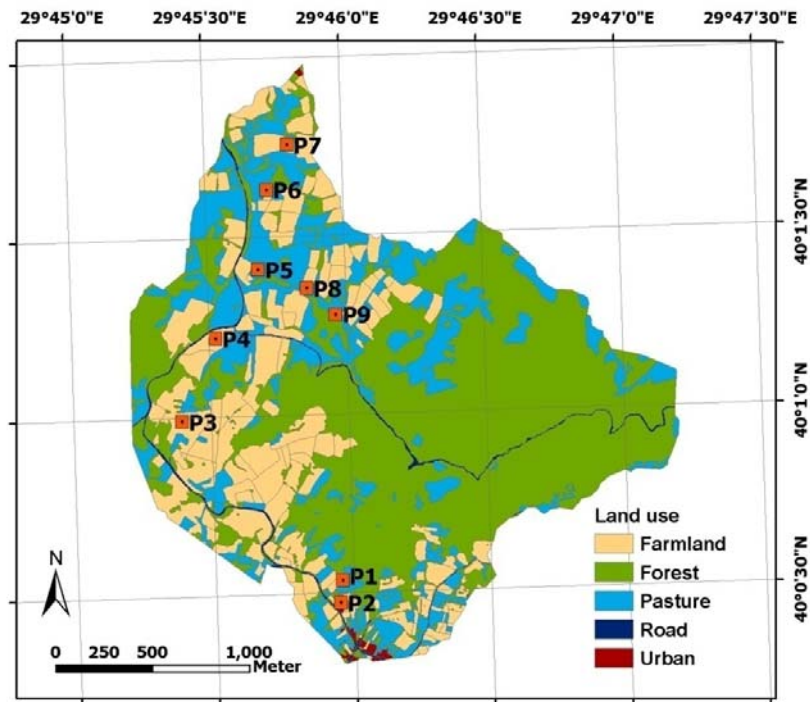


Figure 3.4. Locations of soil moisture measurement plots within the basin

The Time Domain Reflectometer (TDR) is an electronic tool, which is composed of two parts as shown in Figure 3.5: a display/computing unit and a measurement probe. As photographed in Figure 3.6, a typical volumetric soil moisture measurement is carried out by inserting the two probes of the instrument into the soil and reading the value from the display in the units of percentages (%). TDR measures the electrical conductivity of the soil between the probes and some of the device parameters are tabulated in Table 3.3. For all point soil moisture measurements, probes having a length of 16 cm are used in all field studies.

Table 3.2. Land use class and number of points within nine measurement plots

Plot #	Land use	Number of Points
P1	Farmland	6
P2	Farmland	8
P3	Farmland	9
P4	Farmland	10
P5	Pasture	8
P6	Farmland	7
P7	Farmland	9
P8	Pasture	7
P9	Pasture	4
Total	6 Farmland + 3 Pasture	68 = 49 + 19

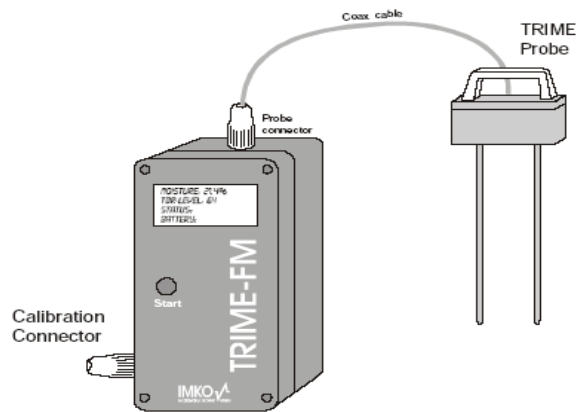


Figure 3.5. Time Domain Reflectometer (TDR)

Table 3.3. Technical specifications of the TDR instrument

Measurement Time	10 -15 seconds
Sensitivity	0.1 %
Accuracy on Remeasurement	± 0.3 %
Range of Measurement	0-100 %
Temperature Range	-15 °C - 50 °C



Figure 3.6. A typical measurement with a TDR

The field studies are carried out for the water year 2004 – 2005. At each field trip, surface soil moisture values of the 68 previously selected locations are measured with the TDR. The field study dates are selected in advance to match the radar image acquisition dates, which will be discussed in Chapter 4 of the thesis. The dates and measured average soil moisture values on these field trips are tabulated in Table 3.4. It is observed from Table 3.4 that the highest average soil moisture is measured on 2-June-2005, just one day after a flood event occurred in the catchment.

3.3. Resampling of Point Soil Moisture Measurements

In the planning phase of the field studies, locations of the soil moisture measurement plots are selected from farmland and pasture areas of the basin. Each plot is homogenous for its land use class, and measurement points within the plot are determined in a grid manner (by taking regular interval points) to represent the whole plot. Depending on the size and orientation of the plot, the total number and distribution of the measurement points vary among these plots (Table 3.2).

Table 3.4. Field study dates and measured average volumetric soil moisture values (%)

Date	All n = 68	Pasture n = 49	Farmland n = 19
09-Oct-2004	16.17	19.20	14.57
13-Nov-2004	13.79	18.62	11.92
15-Dec-2004	27.89	36.96	24.37
18-Dec-2004	20.50	27.47	17.73
28-Apr-2005	24.28	34.57	20.29
07-May-2005	26.12	35.27	22.58
02-Jun-2005	34.37	44.74	30.34
11-Jun-2005	29.24	43.88	23.56
20-Aug-2005	12.06	13.01	11.69

n; number of point soil moisture measurements

In Geographic Information System (GIS) terminology, grid or raster data model represents the geographic distribution of a single variable on an array of equally sized square cells arranged in rows and columns. Each grid cell is referenced by its geographic X, Y location. The Digital Elevation Model (DEM) of the study area shown in Figure 3.1 is an example of the grid/raster type data model, in which topographic elevation of the basin is represented by 30 m x 30 m grid cells each of which has an elevation value for the 900 m² of the cell area. Moreover, both the radar and Quickbird images have raster type data models, with ground resolutions (square cell size/dimension) of 12.5 m and 0.60 m, respectively.

In the analysis part of the study, while investigating relationships between the point moisture and radar backscatter values, one of the major problems faced is matching point moisture measurement locations with the grid cell representation of backscatter values. In order to derive similar relations effectively, it is concluded that coinciding point locations with the raster data cells is a necessity.

This is achieved by first selecting the raster type data having the highest ground resolution. Since radar images have a ground resolution of 12.5 m and the Quickbird image has a 0.6 m cell size, resolution of the DEM of the catchment, 30 m is the highest among the raster data sets and it is selected as the base resolution for the study. Then, soil moisture surfaces are computed from the point measurement locations. A single surface is derived for each plot on each field trip date by using Kriging interpolation technique (Stein, 1999). In this procedure, the Inverse Distance Weighted (IDW) and Spline surface interpolation techniques are also used. The decision in selection of the interpolation technique is based on by visual inspection of the soil moisture surfaces overlaid with the slope map of the respective plot. As a general rule, soil moisture values are expected to increase with the increasing slope. It is observed that the surfaces interpolated with the Kriging technique have better results than the other two interpolation techniques.

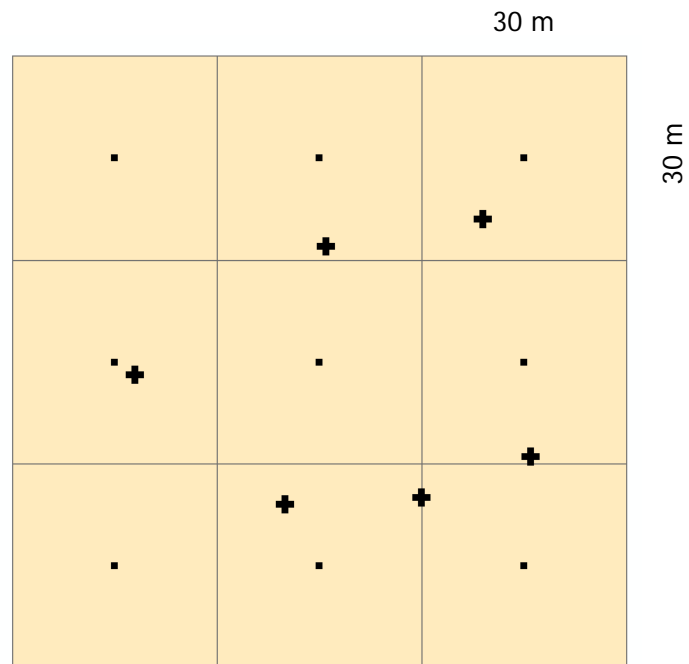
After overlaying the interpolated surfaces with grid cell boundaries of the DEM, average moisture value within each cell boundary is computed from the interpolated surface and assigned to the point at the geometric center of the cell. As an example, the original TDR measurement points (indicated with a + sign) and the new resampled points (indicated with square dots) of the Plot 1 are presented in Figure 3.6. The square grid cells shown in Figure 3.7 have 30 m by 30 m dimensions and obtained from grid data model of the DEM. This interpolation technique is applied to all plots and the total number of points is increased to 126. The number of original and resampled points within each plot is tabulated in Table 3.5.

Finally, results of the interpolation method are analyzed by comparing average, maximum and minimum moisture values of the original TDR measurements (n = 68) in Table 3.6, with the similar values of the resampled points (n = 126) in Table 3.7. This is carried out by computing percent change in the volumetric soil moisture values with Equation 3.1.

$$\text{Percent Change} = \frac{(\text{Moist}_{TDR} - \text{Moist}_{\text{Resampled}})}{\text{Moist}_{TDR}} \times 100 \quad (3.1)$$

Table 3.5. The number of original and resampled points for each plot

Plot	Land use	Number of Points	
		Original - TDR	Resampled - Kriging
P1	Farmland	6	9
P2	Farmland	8	9
P3	Farmland	9	12
P4	Farmland	10	24
P5	Pasture	8	20
P6	Farmland	7	12
P7	Farmland	9	16
P8	Pasture	7	15
P9	Pasture	4	9
Total	6 Farmland + 3 Pasture	68 = 49 + 19	126 = 82 + 44



+ original TDR measurement location
 . new resampled point moisture location

Figure 3.7. Original and resampled point soil moisture locations in Plot 1

Equation 3.1 is evaluated for all of the average, maximum and minimum moisture values of the original TDR and resampled points in Tables 3.6 and 3.7, and the computed percent changes are tabulated in Table 3.8. It is also calculated from Table 3.8 that the average percent change in daily average moisture values is -6.56 % for all farmland and pasture land use classes, -2.63 % for farmlands and -4.04 % for pasture areas. These estimates are found accurate enough and the analyses described in the next chapters of the thesis are continued with the new 126 point locations.

Table 3.6. Statistical parameters of the original TDR points
(volumetric soil moisture values in %)

%	Farm and Pasture $n_1 + n_2 = 68$			Farm $n_1 = 49$			Pasture $n_2 = 19$		
	Date	Ave	Min	Max	Ave	Min	Max	Ave	Min
09-Oct-04	16.17	8.26	36.40	14.57	8.26	32.38	19.20	9.10	36.40
13-Nov-04	13.79	5.70	37.80	11.92	5.70	24.35	18.62	9.70	37.80
15-Dec-04	27.89	14.60	62.30	24.37	14.60	36.90	36.96	19.00	62.30
18-Dec-04	20.50	5.10	44.00	17.74	5.10	27.00	27.47	18.51	44.00
28-Apr-05	24.28	9.70	55.40	20.29	9.70	31.40	34.57	19.20	55.40
07-May-05	26.12	10.70	51.60	22.58	10.70	33.20	35.27	22.90	51.60
02-Jun-05	34.37	21.60	63.50	30.34	21.60	38.20	44.74	34.70	63.50
11-Jun-05	29.24	9.90	70.80	23.56	9.90	38.20	43.88	28.50	70.80
20-Aug-05	12.06	4.80	35.70	11.69	4.80	26.70	13.01	6.70	35.70

Table 3.7. Statistical parameters of the resampled points
(volumetric soil moisture values in %)

% Date	Farm and Pasture n1 + n2 = 126			Farm n1 = 82			Pasture n2 = 44		
	Ave	Min	Max	Ave	Min	Max	Ave	Min	Max
09-Oct-04	16.52	7.04	31.27	14.64	8.04	27.82	18.93	7.04	31.27
13-Nov-04	14.51	5.93	35.62	11.92	5.93	20.69	19.32	8.31	35.62
15-Dec-04	30.19	15.24	58.46	25.27	15.24	37.78	39.36	20.04	58.46
18-Dec-04	21.58	6.64	42.85	17.82	6.64	25.83	28.60	19.84	42.85
28-Apr-05	26.23	8.96	54.36	20.68	8.96	32.88	36.57	23.35	54.36
07-May-05	28.20	11.57	52.77	23.15	11.57	35.32	37.61	24.95	52.77
02-Jun-05	35.82	22.06	57.36	30.78	22.06	36.71	45.22	37.59	57.36
11-Jun-05	32.25	11.38	68.13	24.67	11.38	36.44	46.38	29.81	68.13
20-Aug-05	12.98	5.09	32.69	12.66	5.09	25.44	13.56	5.59	32.69

Table 3.8. Percent change between the average, minimum and maximum values of
soil moisture for original TDR and resampled points

% Date	Farm and Pasture			Farm			Pasture		
	Ave	Min	Max	Ave	Min	Max	Ave	Min	Max
09-Oct-04	-2.13	14.74	14.09	-0.47	2.71	14.08	1.39	22.61	14.09
13-Nov-04	-5.17	-4.08	5.77	-0.02	-4.08	15.04	-3.76	14.33	5.77
15-Dec-04	-8.26	-4.35	6.16	-3.70	-4.35	-2.39	-6.50	-5.45	6.16
18-Dec-04	-5.32	-30.25	2.62	-0.49	-30.25	4.34	-4.11	-7.16	2.62
28-Apr-05	-8.02	7.64	1.87	-1.91	7.64	-4.73	-5.79	-21.61	1.87
07-May-05	-7.97	-8.14	-2.26	-2.57	-8.14	-6.38	-6.65	-8.95	-2.26
02-Jun-05	-4.23	-2.15	9.67	-1.43	-2.15	3.89	-1.07	-8.32	9.67
11-Jun-05	-10.30	-14.99	3.78	-4.71	-14.99	4.60	-5.69	-4.61	3.78
20-Aug-05	-7.63	-6.06	8.42	-8.36	-6.06	4.72	-4.21	16.53	8.42
Average	-6.56	-5.29	5.57	-2.63	-6.63	3.69	-4.04	-0.29	5.57

CHAPTER 4

POST-PROCESSING OF RADAR IMAGERY

4.1. Synthetic Aperture Radar Data

The European Space Agency (ESA), which is founded and financed by a number of European countries, is an international organization working for the commonwealth of Europe. In addition to other space missions, since 1991 ESA has orbited remote sensing satellites which are indeed satellite platforms including a number of sensors. The ESA satellite platforms of ERS-1 (not in operation), ERS-2 and ENVISAT-1 have an Active Microwave Instrument (AMI) which is used to acquire radar imagery.

In this study, radar images that are acquired by the AMI of ERS-2 and ENVISAT-1 satellites are used during the field campaign in the Kurukavak basin. Both of the AMIs on the two satellites work within the C band and have a frequency of 5.3 GHz. But they differ in other technical properties and capabilities, which are discussed briefly in this section of the study.

The European Remote Sensing-2 (ERS-2) satellite, which is orbited on 21 April 1995, is designed to be used for multidisciplinary earth observation studies. ERS-2 has an altitude of 785 km and acquires images with a temporal resolution of 35 days. The AMI on ERS-2 platform is composed of two sensors: SAR (Synthetic Aperture Radar) and Wind Scatterometer.

The SAR of the ERS-2 platform is designed to look to the right of the platform (according to flight direction) with a constant angle of 20.3° from platform nadir. Hence, it obtains active microwave images with a certain angle of incidence at the

mid-span, which is about 23° . Moreover, the radar imagery acquired by ERS-2 SAR sensor has a constant swath width of 100 km and a single type of polarization of VV (Vertical Send – Vertical Receive). The basic operational geometry of the SAR instrument on ERS-2 is illustrated in Figure 4.1.

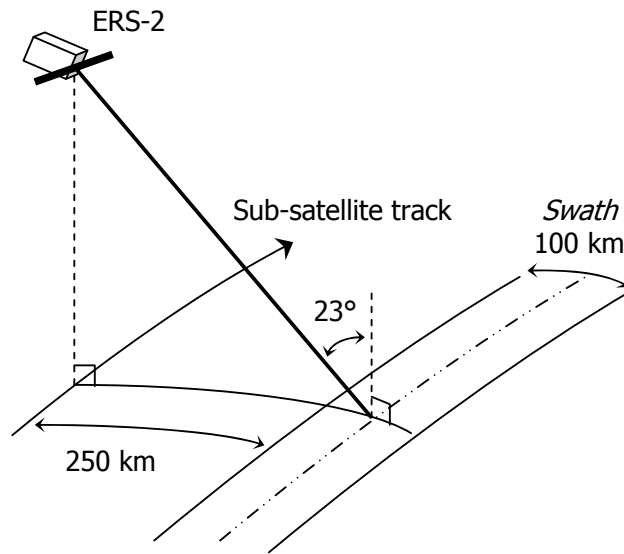


Figure 4.1. SAR image acquisition geometry of ERS-2

The SAR images, which are acquired by ERS-2 satellite, are delivered to ESA ground stations (referred as PAFs: Processing and Archiving Facilities). The PAFs could perform predefined level of algorithms on the images depending on the user requirements. The ERS-2 SAR imagery acquired for the Kurukavak basin is Level 1 products, referred as Precision Image Product (PRI). Level 1 products are calibrated and corrected for the SAR antenna pattern and range-spreading loss. Radar backscatter can be derived from the image for geophysical modeling, but no correction is applied for terrain-induced radiometric effects. The delivered image is not geocoded and terrain distortion has not been removed (Laur et al., 2004). The ground resolution of Level 1 PRI images used in this study is 12.5 meters and has unsigned DN values on 16 bit scale.

The ENVISAT platform, which is launched on March of 2002, is designed to provide atmosphere, ocean, earth and glacier imaging for geoscientists. Similar to the other

remote sensing platforms orbited in the last decade, the ENVISAT platform occupies a number and type of sensors. Of these sensors, the AMI includes a SAR antenna which is referred as Advanced Synthetic Aperture Radar (ASAR) instrument.

As mentioned earlier, the ASAR instrument on the ENVISAT platform also works within the C band of microwave spectrum (5.3 GHz). Different from ERS-2 SAR images, the ASAR images could be acquired in one of the three polarization modes: HH, VV and VH, and, at a number of incident angles. As schematically represented in Figure 4.2, ASAR antenna is oriented on the right looking position of the platform but has the capability of acquiring images on seven different swaths, each having a different incident angle and swath width (Table 4.1). Moreover, the ASAR images could be obtained with alternative (dual) polarization, in which a single image can include two image layers of the same area having two different polarization types.

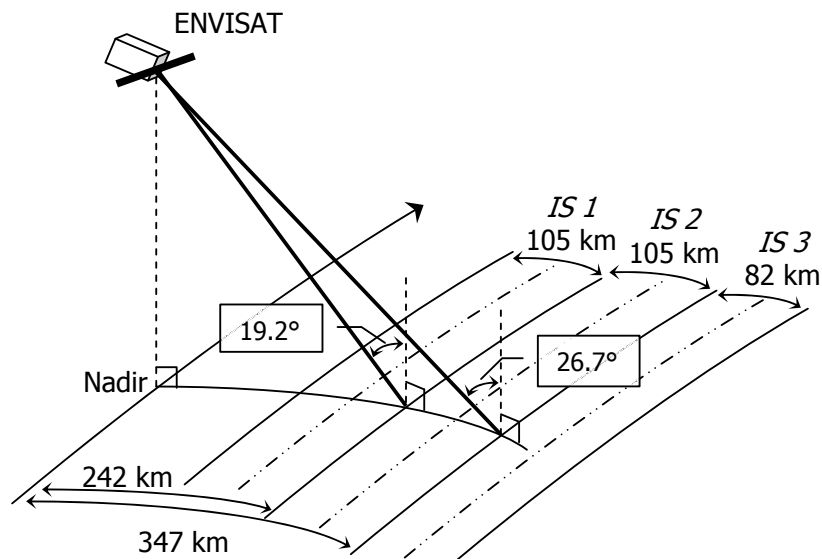


Figure 4.2. ASAR image acquisition geometry of ENVISAT

Table 4.1. ASAR image properties (ESA, 1998)

Swath	Swath Width (km)	Ground position from nadir (km)	Incidence Angle Range (degree)
IS 1	105	187 - 292	15.0 – 22.9
IS 2	105	242 – 347	19.2 – 26.7
IS 3	82	337 – 419	26.0 – 31.4
IS 4	88	412 – 500	31.0 – 36.3
IS 5	64	490 – 555	35.8 – 39.4
IS 6	70	550 – 620	39.1 – 42.8
IS 7	56	615 - 671	42.5 – 45.2

The ASAR images acquired for the Kurukavak basin are also Level 1 type of products, which are referred as Image Mode Precision Image (IMP) products. Moreover, the obtained ASAR imagery has VV type of polarization with a ground resolution of 12.5 meters and a pixel depth of 16 bits. Since the images are acquired on Swath 2 (IS 2 in Table 4.1), the mid-span incidence angle of ASAR images is about 23°.

Between October 2004 and August 2005, a total of nine field studies are performed (Table 3.3) and a total of 16 SAR and ASAR images are acquired (Table 4.2). Among these field trips and images, four of them; **09-Oct-2004**, **18-Dec-2004**, **07-May-2005** and **20-Aug-2005**, are selected for mapping surface soil moisture condition of the basin. The time of image acquisitions are also given in Table 4.1 in Coordinated Universal Time (UTC); 8:00 UTC time corresponds to 10:00 local time in Turkey. The selection is based on the vegetation condition of the study fields and the number of images acquired on that day. As tabulated in Table 4.2, on the selected field study dates two radar images, SAR and ASAR, are available for analysis. Even if two radar images are available, 11-Jun-2005 is not selected for moisture mapping due to lack of information about vegetation index on that day. The selection criteria will be also discussed in detail in the Chapters 5 and 6 of this study.

In the post-processing of radar images, first the product header files and then the image DN values are extracted. Since Level 1 products are not georeferenced, SAR and ASAR images are geocoded by using 1/25000 and 1/100000 scaled topographic maps of the region. For this purpose, a number of ground control points: like dam crest, roadway, airport runway, etc., are identified and used in georeferencing of radar images. The geocoded ERS-2 SAR image of 09-Oct-2004 is shown in Figure 4.3, in which the Āznik Lake can be identified as the large black area on the north of the image.

Table 4.2. Radar imagery acquired for the study area

Date	ERS-2 / ENVISAT	Time of Acquisition SAR/ASAR UTC	Vegetation Condition for Farmland & Pasture Fields	Average Soil Moisture (%)
09-Oct-2004	SAR/ASAR	8:44/8:16	Sparse	16.17
13-Nov-2004	SAR	8:44	Sparse	13.79
15-Dec-2004	-	-	Almost Bare	27.90
18-Dec-2004	SAR/ASAR	8:44/8:16	Almost Bare	20.50
28-Apr-2005	ASAR	7:59	Dense	24.30
07-May-2005	SAR/ASAR	8:44/8:16	Dense	26.12
02-Jun-2005	ASAR	7:59	Dense	34.40
11-Jun-2005	SAR/ASAR	8:44/8:16	Dense	29.24
20-Aug-2005	SAR/ASAR	8:44/8:16	Sparse	12.06

4.2. Computation of Incidence and Local Incidence Angles

As schematically represented in Figure 2.4, incidence angle is the angle between the radar beam and the normal to the earth surface at the point of incidence. In derivation of radar backscatter values from image DN values, an incidence angle map of the image is required. The details of backscatter computation will be discussed in the section 4.3 of the study.

In the post-processing of radar imagery, two incidence angle maps are computed for each radar image: *incidence angle* and *local incidence angle*. The former one, *incidence angle*, is computed for the whole swath (100 – 105 km) of SAR/ASAR

image and by assuming a flat terrain for the area. It is the incidence angle utilized in the derivation of backscatter values. The latter one, *local incidence angle*, is computed for the study catchment area and by utilizing topography of the basin. It is one of the parameters used to derive radar backscatter relationships in the Chapters 5 and 6 of the study.

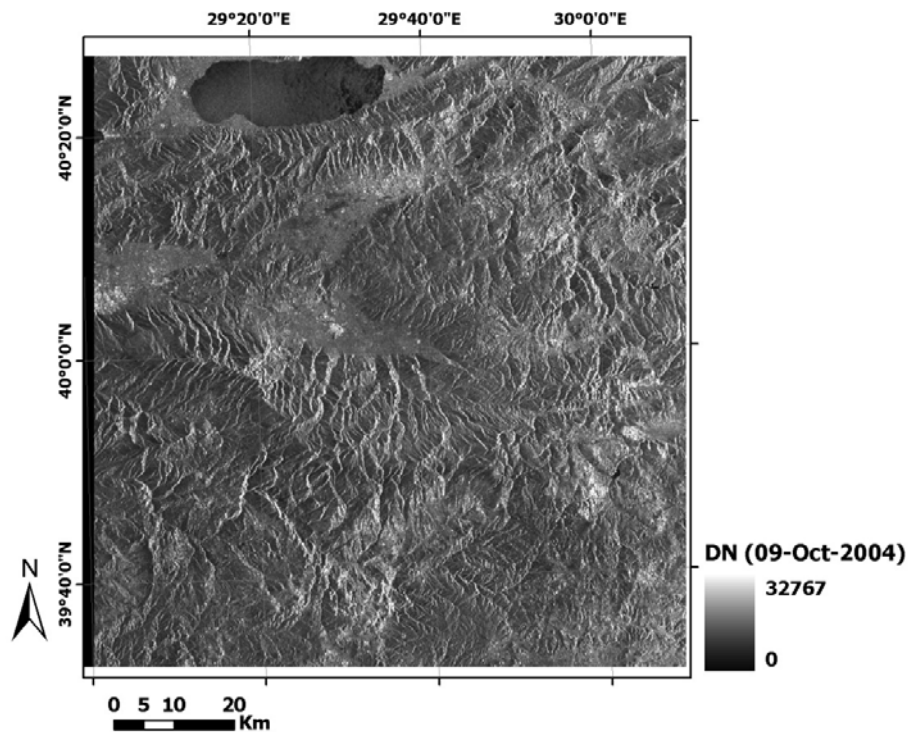


Figure 4.3. Georeferenced SAR image for 09-October-2004

Different from airborne systems, incidence angle depends significantly on the earth curvature for spaceborne radar images. In this study, the reference ellipsoid (Goddard Earth Model 6: GEM6), which is used to represent the earth surface by ERS-2 and ENVISAT satellites, is utilized for the computations (Laur et al., 2004).

The *incidence angle* (α) is computed by the procedure, which is described by ESA (Laur et al., 2004) and summarized below from Equation 4.1 to Equation 4.6. The schematic representation of the geometric and ellipsoid parameters used in the procedure is given in Figure 4.4.

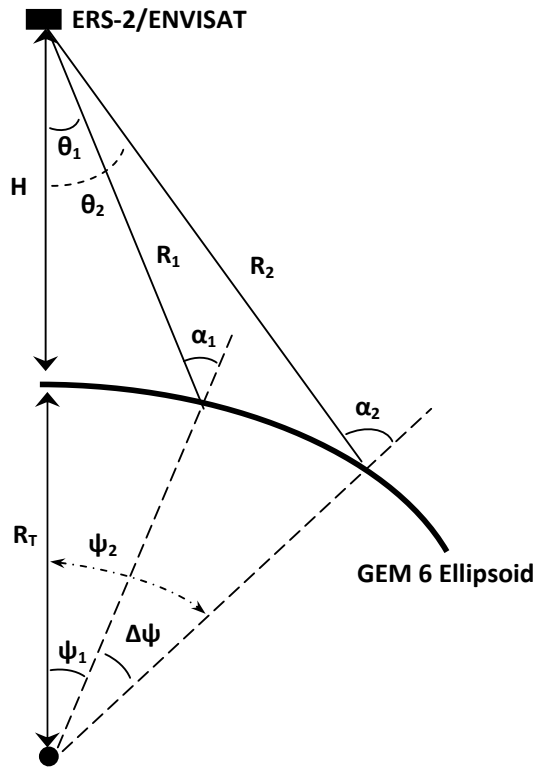


Figure 4.4. The schematic representation of the parameters used in the computation of the incidence angle at the i^{th} coordinate (α_i)

The Earth radius R_T , is calculated using:

$$R_T = a \left[\cos^2 \lambda + (b/a)^4 \times \sin^2 \lambda \right] \times \left[\cos^2 \lambda + (b/a)^2 \times \sin^2 \lambda \right]^{-1/2} \quad (4.1)$$

where;

a is the equatorial Earth radius (6378.144 km)

b is the polar Earth radius (6356.759 km)

a and b values correspond to the ERS reference ellipsoid: GEM6

λ is the geodetic latitude of image centre (obtain from product header file)

From the ERS reference geometry, the ERS altitude (H) is given by:

$$R_T + H = \left[R_T^2 + R_1^2 + 2 \times R_T \times R_1 \times \cos \alpha_1 \right]^{1/2} \quad (4.2)$$

where;

α_1 is the near range incidence angle, (obtain from product header file)

R_1 is the slant range distance to the first range pixel = $c \times t_1 / 2$

t_1 is the zero Doppler range time of the first range pixel (obtain from product header file)

c is the velocity of light

The near range look angle (θ_1) is given by:

$$\cos \theta_1 = (R_1 + R_T \times \cos \alpha_1) / (R_T + H) \quad (4.3)$$

The Earth angle for the pixels in i^{th} column of the image (ψ_i) is:

$$\psi_i = (\psi_1 + \Delta \psi_i) = \psi_1 + (i - 1) \times \Delta r / R_T \quad (4.4)$$

$\psi_1 = \alpha_1 - \theta_1$ (The Earth angle for first range pixel)

Δr is the swath width

The slant range to a pixel at i^{th} column of the image (R_i) is given by:

$$R_i = \left[R_T^2 + (R_T + H)^2 - 2 \times R_T \times (R_T + H) \cos \psi_i \right]^{1/2} \quad (4.5)$$

The incidence (α_i) angle at pixel coordinate i is given by:

$$\cos \alpha_i = \left[(R_T + H)^2 - R_i^2 - R_T^2 \right] / (2 \times R_i \times R_T) \quad (4.6)$$

The incidence angle grids are computed separately for the SAR and ASAR images of the dates: 09-Oct-2004, 18-Dec-2004, 07-May-2005 and 20-Aug-2005, with the same resolution of the actual images, 12.5 m. Even if they both acquire radar imagery of the same region on the same date, the ERS-2 and ENVISAT satellites pass through different tracks, and hence images obtained from these platforms have different incidence angle values for the same locations. As a result, two incidence angle grids are computed for each field study date. The incidence angle grid, evaluated for the SAR image of 09-Oct-2004 is shown in Figure 4.5.

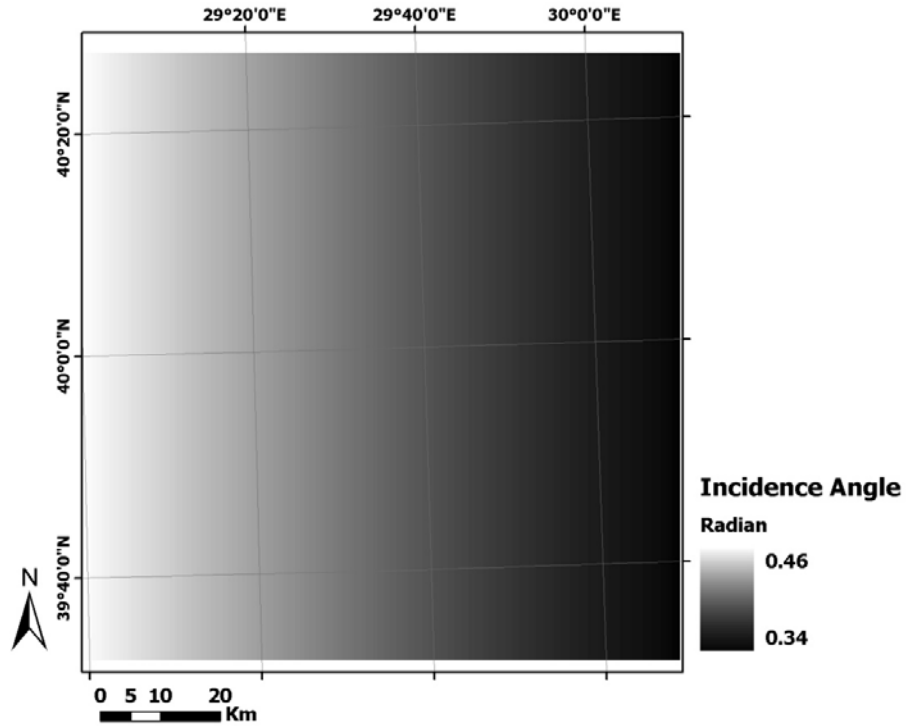


Figure 4.5. Incidence Angle (α) grid of the 09-October-2004 dated SAR image

In the computation of the *local incidence angle* (θ_L) of the Kurukavak basin, topographic characteristics of the study area are utilized. For this purpose, first the slope and aspect maps of the basin are derived from Digital Elevation Model (DEM) of the catchment. The schematic representation of the Equation 4.7 (Su et al., 1997), which is then used to compute the local incidence angle (θ_L), is presented in Figure 4.6.

Similar to the computation of incidence angle grids, local incidence angle grids are calculated separately for the SAR and ASAR images of the dates: 09-Oct-2004, 18-Dec-2004, 07-May-2005 and 20-Aug-2005. Since the computation requires topography, these grids are evaluated within the basin boundary and with the same resolution of Kurukavak DEM, 30 meters. Moreover, two *local incidence angle* grids

are computed for each field study date and the local incidence angle grid, evaluated for SAR image of 09-Oct-2004, is shown in Figure 4.7.

$$\cos \theta_L = \cos (s) \times \cos (\alpha) + \sin (s) \times \sin (\alpha) \times \cos (\varphi - a) \quad (4.7)$$

where:

s is surface slope (radians)

a is surface aspect (radians, with geometric north equal to 0)

α is incidence angle (computed for GEM6 ellipsoid)

φ is flight track angle: angle between the satellite track and the geometric north (radians: obtained from product header file)

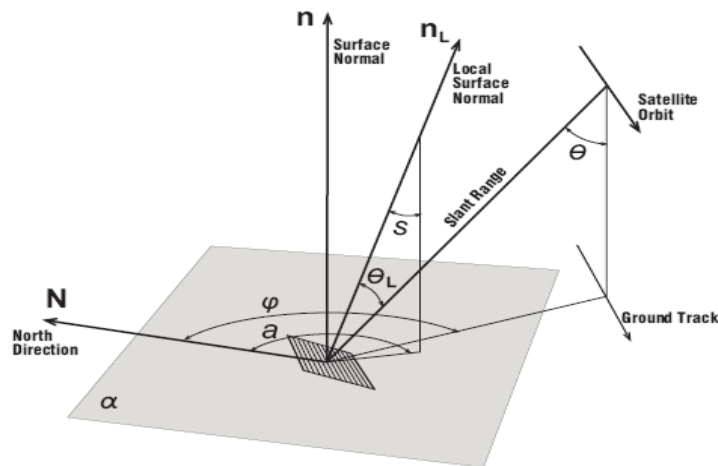


Figure 4.6. The schematic representation of the parameters used in the computation of the local incidence angle (θ_L)

4.3. Derivation of Radar Backscatter Coefficients

Depending on the source of electromagnetic energy, microwave sensors are categorized in two groups: active and passive sensors. Passive sensors, commonly called as *Radiometers*, record the electromagnetic energy emitted by the target itself and output of these systems are referred as *Brightness* or *Brightness Temperature*. On the other hand, active systems, known as *Radars*, transmit their

own source of energy and record the portion of the transmitted energy which is "scattered" by the target and reflected "back" to the sensor. Hence, output of radar systems is called as *Backscatter*.

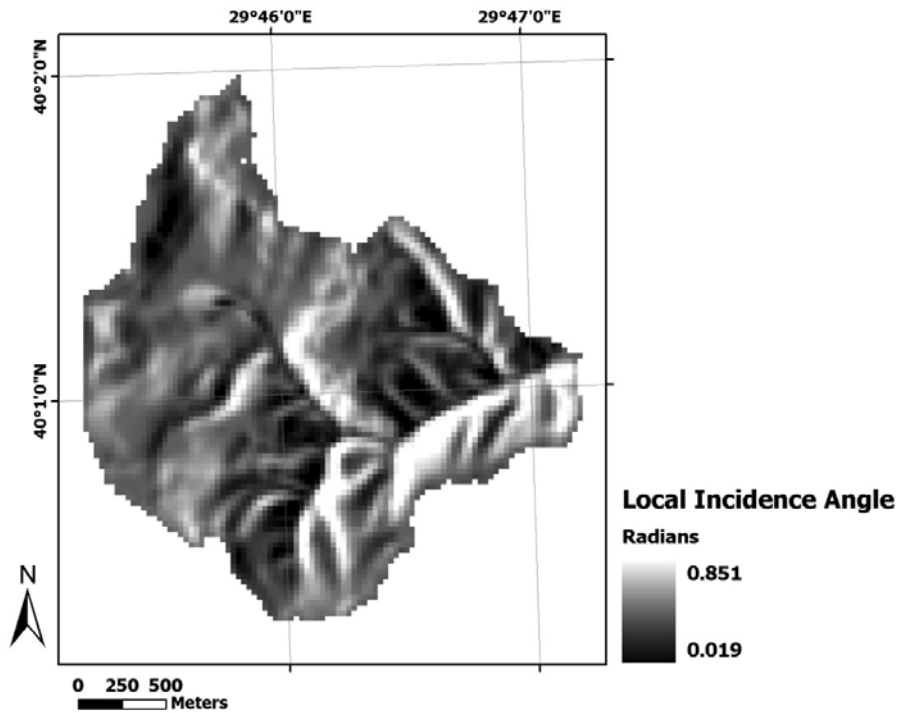


Figure 4.7. The Local Incidence Angle (θ_L) grid of the 09-October-2004 dated SAR image

The radar backscatter values are computed from the DN (Digital Number) values of the acquired SAR and ASAR images. The computation is carried out by using Equations 4.8 and 4.9 (Laur et al., 2004; Rosich and Meadows, 2004) on a pixel by pixel basis. Similar to the derivation of incidence angle grids, backscatter values are computed for the whole swath width of the radar imagery. First, the backscatter values are derived in amplitude, and then these values are converted to decibel (dB) units.

$$BS = DN^2 \times \frac{1}{K} \times \frac{\sin(\alpha)}{\sin(\alpha_{ref})} \quad (4.8)$$

where:

BS is radar backscatter (amplitude: m²/m²)

DN is digital number

K is calibration coefficient

α is incidence angle (radians)

α_{ref} is incidence angle at the center of the image (radians)

$$BS \text{ (dB)} = 10 \times \text{Log}_{10}(BS) \quad (4.9)$$

In the last part of post-processing of radar imagery, backscatter grids of the Kurukavak basin for the selected field study dates are extracted by overlaying basin boundary with the SAR and ASAR images.

The interaction of radar beams with rough surface objects results in addition or cancellation of recorded waves, causing random return backscatter values for similar adjacent surfaces, which is known as *speckle* (Henderson and Lewis, 1998). Removal of speckle is necessary for quantitative analysis of radar imagery (Thoma et al., 2006). In this study, a 3 x 3 mean low pass filter, which calculates the average (mean) value of the 3 x 3 neighborhood and assigns this value to the center cell of the neighborhood, is used for speckle removal of the backscatter grids.

Finally, the filtered backscatter grids, which have the same resolution of raw radar images (12.5 m), are resampled to the general working resolution of the study (30 m). Moreover, resampling process is carried out to match exactly the same cell locations of the DEM, and hence to match the soil moisture measurement locations. The radar backscatter grids are computed for both of the SAR and ASAR images of 09-Oct-2004, 18-Dec-2004, 07-May-2005 and 20-Aug-2005 dates. Among them the backscatter grid, derived for the SAR image of 09-Oct-2004 with a range of backscatter values from -17.43 dB to 3.67 dB, is represented in Figure 4.8.

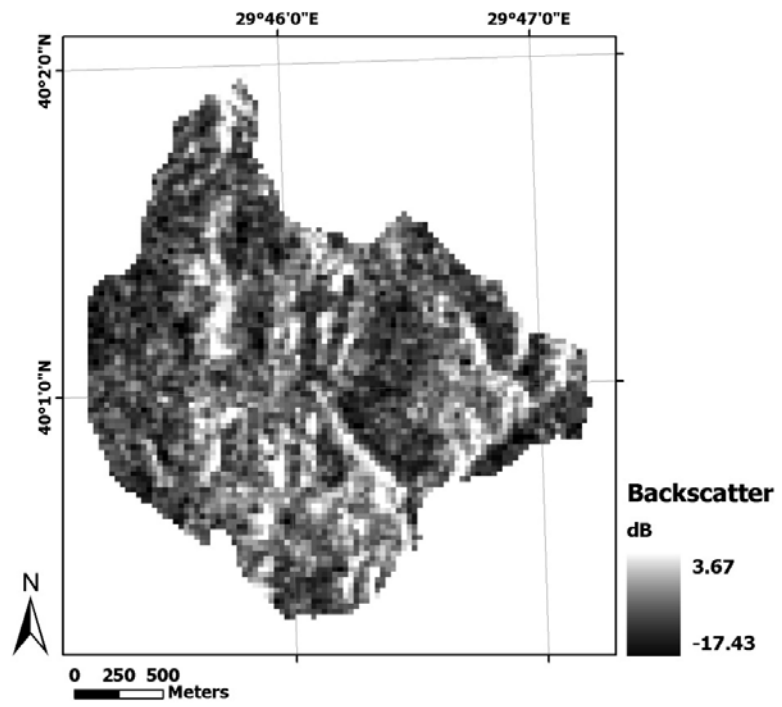


Figure 4.8. The Backscatter grid of the 09-October-2004 dated SAR image

CHAPTER 5

SOIL SURFACE ROUGHNESS

Radar backscatter, which depends on sensor parameters of incidence angle, frequency and polarization, is also correlated with soil surface roughness and moisture for bare soil fields (Leconte et al., 2004). As a result, estimation of surface roughness (either by experimental observations or analytical methods) became an essential part of radar remote sensing of soil moisture studies (Baghdadi et al., 2002c; Neusch and Sties, 1999; Sahebi et al., 2002).

One of the major goals of this study is to establish an accurate relationship between radar backscatter and surface roughness for bare or sparsely vegetated areas of the Kurukavak basin. For this purpose, a semi-empirical backscatter model, Dubois Model, is utilized for the SAR and ASAR images of 09-Oct-2004, 18-Dec-2004 and 20-Aug-2005 dates. Due to dense vegetation cover condition of the study catchment on 07-May-2005 (Table 4.2); this field study date is not included in roughness estimation.

5.1. Inversion of Dubois Model

One of the methods, commonly applied in radar remote sensing of soil moisture and surface roughness, is using a semi-empirical or a physical backscatter model. Among the many semi-empirical backscatter models, the most popular ones are those developed by Oh (Oh et al., 1992) and Dubois (Dubois et al., 1995) from scatterometer measurements and airborne SAR observations over bare soil surfaces. In addition, the Integral Equation Model (IEM) (Fung et al., 1992) is the most

commonly used physical backscatter model. IEM is generally used for inversion of soil moisture and roughness from radar data (Baghdadi and Zribi, 2006).

Dubois et al. (1995) proposed a semi-empirical approach for modeling of radar backscatter values for bare surfaces, by using scatterometer data. The model relates the HH or VV polarization to the soil's dielectric constant, surface roughness, incidence angle and radar frequency. Basically, for a given radar configuration and soil roughness, this model explicitly relates the dielectric constant of a soil to the backscattering coefficient, which is expressed in decibel (dB). The two equations of the model, for HH and VV radar polarizations, are given in Equations 5.1 and 5.2, respectively.

$$\sigma_{HH}^0 = 10^{-2.75} \left[\frac{\cos^{1.5} \theta}{\sin^5 \theta} \right] 10^{0.028 \varepsilon \tan \theta} (k h \sin \theta_L)^{1.4} \lambda^{0.7} \quad (5.1)$$

$$\sigma_{VV}^0 = 10^{-2.35} \left[\frac{\cos^3 \theta}{\sin^3 \theta} \right] 10^{0.046 \varepsilon \tan \theta} (k h \sin \theta_L)^{1.1} \lambda^{0.7} \quad (5.2)$$

where;

σ_{HH} is radar backscatter for HH polarization (dB)

σ_{VV} is radar backscatter for VV polarization (dB)

θ_L is local incidence angle (radian)

ε is dielectric constant of the surface

h is root mean square height of surface; *surface roughness* (cm)

λ is radar wavelength (cm)

$k = 2\pi / \lambda$

Since all of the radar images, which are acquired for the study area, have VV polarization and the Dubois model propose an explicit relationship as in Equation 5.2, inversion of the model is used in this study for soil surface roughness estimation. The model has been derived for bare soil surfaces, but Dubois et al. (1995) also state that it can be applied to moderately dense vegetation cover with a Normalized Difference Vegetation Index (NDVI) as high as 0.4. As a result, inversion of the model is applied for sparsely vegetated farmland and pasture fields of the study basin for the 09-Oct-2004, 18-Dec-2004 and 20-Aug-2005 dates.

Dielectric constant (ϵ) of a material is a fundamental property which characterizes both the reflection and attenuation properties of an electromagnetic wave interacting with that material (Ulaby et al., 1996). The sensitivity of dielectric constant to water is the basis for estimation of soil moisture with microwave sensors. It can range from 2.5 for very dry soil to 25 for very moist soil depending on soil composition and radar frequency (Ulaby et al., 1978). In this study, Equation 5.3, which is experimentally developed by Topp et al. (1980), is used to convert volumetric soil moisture values to dielectric constants. During this experimental study it is found that dielectric constant of soil is not strongly sensitive to temperature (10 – 36 °C), soil texture (clay to sandy loam), bulk density of soil (1.14–1.44 mg m⁻³, for non-swelling soils) and soluble salt content (Noborio, 2001). Considering the three major soil types within the Kurukavak basin; loam, sandy loam and sandy clay loam, it is concluded that Equation 5.3 could be used for inversion of soil dielectric values through the farmland and pasture fields of the basin.

$$m_v = [-530 + 292 (\epsilon) - 5.5 (\epsilon)^2 + 0.043 (\epsilon)^3] \times 10^{-4} \quad (5.3)$$

where:

m_v is soil moisture content (Volumetric: m³ m⁻³)

ϵ is soil dielectric constant

The procedure for estimating surface roughness values is described in four steps:

- i) Volumetric soil moisture (m_v) values, which are measured with TDR, are converted to dielectric constants (ϵ) using Equation 5.3,
- ii) Radar backscatter (σ_{VV}) and local incidence (θ_L) angle values are extracted by overlaying soil moisture measurement points with the respective grids,
- iii) Since ERS-2 and ENVISAT active microwave sensors work at 5.3 GHz, radar wavelength (λ) is 5.66 cm, and the wave number (k) is computed as 1.11,
- iv) Soil surface roughness (h) values are computed from the inversion of Equation 5.2 of the Dubois model.

This procedure is used to compute roughness values of the 126 point soil moisture measurement locations. Since, 3 field study dates are considered, a total of 378 roughness values are obtained. In order to verify the accuracy of the applied procedure, two roughness values are computed for each point; one from the SAR and one from the ASAR images. This is achieved by preparing two data sets and Table 5.1 summarizes the source of parameters used in these data sets.

- **Set I – SAR:** 378 soil roughness values, computed using the SAR images of 09-Oct-2004, 18-Dec-2004 and 20-Aug-2005 dates.
- **Set II – ASAR:** 378 soil roughness values, computed using the ASAR images of 09-Oct-2004, 18-Dec-2004 and 20-Aug-2005 dates.

Table 5.1. Summary of parameters used in the roughness computation data sets

Parameter	Set I – SAR	Set II – ASAR
Dates	09-Oct-2004, 18-Dec-2004 and 20-Aug-2005	
Backscatter	From SAR imagery (Equation 4.8 and 4.9)	From ASAR imagery (Equation 4.8 and 4.9)
Local Incidence Angle	Topography and SAR imagery (Equation 4.7)	Topography and ASAR imagery (Equation 4.7)
Wavelength	5.66 cm	
k	1.11	
Dielectric Constant	From point soil moisture measurements (Equation 5.3)	

5.2. Analysis of Computed Roughness Values

In the analysis of the calculated roughness values from both of the data sets, a procedure including two levels of reduction is carried out for eliminating some of the computed values. The first level of reduction is based on the Dubois model limitations and the second level is based on the assumption that SAR and ASAR datasets result in similar roughness values for the same locations. For this purpose, first the frequency histograms of the obtained values are plotted separately for each data set (Figure 5.1). The x-axis in Figure 5.1 represents the computed roughness

values in equal bins with axis values as the upper bound of each bin. It is also observed that, about 92 % of the values are obtained below 3 cm, and about 86 % of them are below 2 cm. Since the Dubois model is developed by experimental studies, it is optimized for roughness values below 2.5 cm (Baghdadi and Zribi, 2006). After considering the computed roughness values (Figure 5.1) and the model recommendation, a maximum roughness value of 3.0 cm is selected.

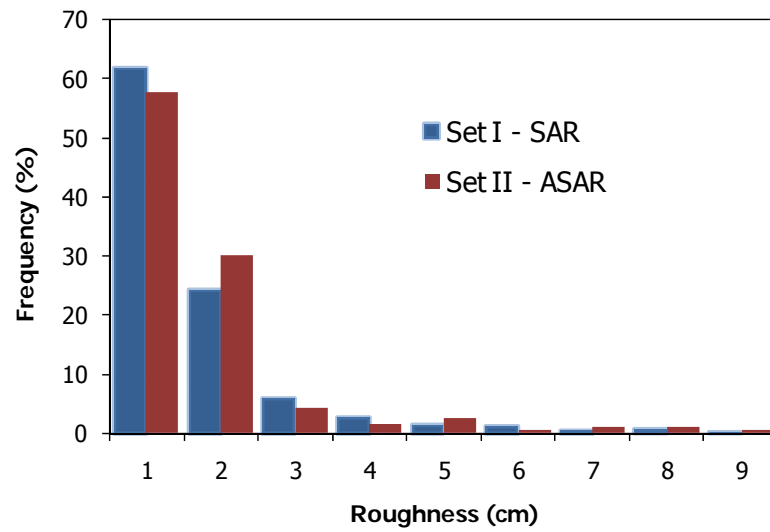


Figure 5.1. Frequency histogram of the computed roughness values (n = 378)

For the 378 points, the Root Mean Square Error (RMSE) between the computed roughness values of Set I and Set II is evaluated as 1.32 cm. After eliminating the points having roughness values greater than 3.0 cm, about 90 % of the points are left and the RMSE value is reduced to 0.49 cm. This is referred as the first level of reduction in Table 5.2.

The second level of reduction is carried out by computing the absolute difference between the calculated roughness values of the two data sets. As given by Equation 5.4, a delta (Δ) value is calculated for each of the 378 points and the frequency histogram of all delta values is shown in Figure 5.2. The x-axis in Figure 5.2 represents the computed delta values in equally spaced bins with axis values as the upper bound of the bin.

$$\Delta = | \text{Roughness (Set I-SAR)} - \text{Roughness (Set II-ASAR)} | \quad (5.4)$$

Table 5.2. Summary of data reduction for roughness values

	Original Data	1 st Reduction	2 nd Reduction
Number of points	378	338	258
% of total points	100	89.4	68.3
RMSE between Set I and II roughness values (cm)	1.32	0.49	0.23
Coefficient of Correlation between Set I and II roughness values	0.70	0.60	0.87

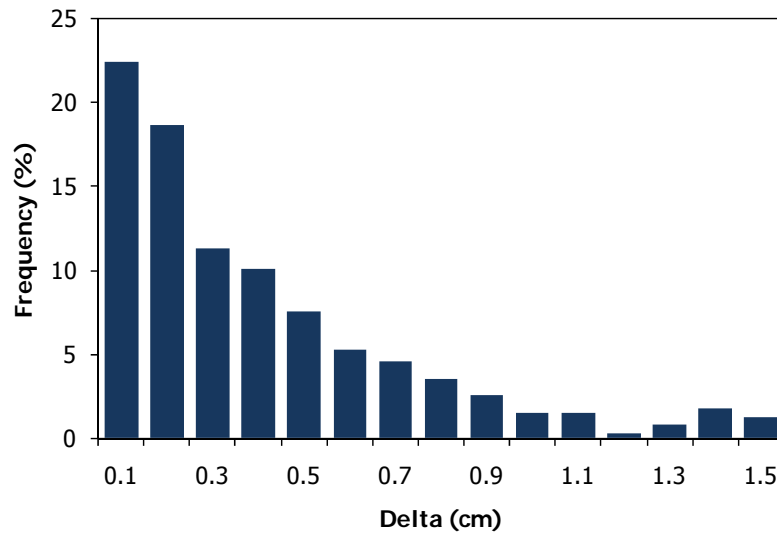


Figure 5.2. Frequency histogram of the computed delta values (n = 378)

It is observed from Figure 5.2 that, for 68.8 % of the measurement points the difference between the computed roughness values from the SAR and ASAR images is less than 0.5 cm and for 52 % of them delta is less than 0.3 cm. The second level of reduction is carried out by eliminating the points having a delta value higher than

the selected threshold value, which is 0.5 cm. For this purpose, a number of different threshold values are investigated as tabulated in Table 5.3 and the threshold value giving the highest correlation coefficient with the maximum number of points (after 2nd level of reduction) is selected. The total number of points after the second level of reduction is 258 (Table 5.2) with a correlation coefficient of 0.87 between the Data Set I-SAR and Data Set II-ASAR roughness values (Figure 5.3). It is concluded from Figure 5.3 that for the 258 points the computed roughness values from the SAR and ASAR images are close enough and a relationship between radar backscatter and soil surface roughness can be investigated.

Table 5.3. Selection of the threshold value for second level of reduction

Delta (cm)	% of total points left after 2 nd level of reduction	RMSE between Set I and II roughness values (cm)	Coefficient of Correlation between Set I and II roughness values
1.0	84.9	0.37	0.73
0.7	77.9	0.30	0.81
0.5	68.8	0.23	0.87
0.3	52.0	0.15	0.94

5.3. Backscatter – Soil Surface Roughness Relationship

After reducing the total number of points to 258 with the two levels of reduction procedure, an average roughness value is computed for each point using Equation 5.5. Arithmetic mean of the two roughness values (h_{SAR} and h_{ASAR}), calculated from Data Set I-SAR and Data Set II-ASAR, is computed and utilized for the derivation of backscatter – soil surface roughness relationship. Even if similar roughness values are computed for the 258 points, soil surface roughness is a physical parameter and each point should be represented with a single value. As a result, arithmetic mean of the computed roughness values is calculated.

$$h_{Average} = \frac{h_{SAR} + h_{ASAR}}{2} \quad (5.5)$$

Then, the relationship between the observed radar backscatter coefficients and computed mean roughness values (Equation 5.5) is investigated by plotting them with respect to each other. The Figures 5.4 and 5.5 represents this relationship for Data Set I-SAR and Data Set II-ASAR, respectively.

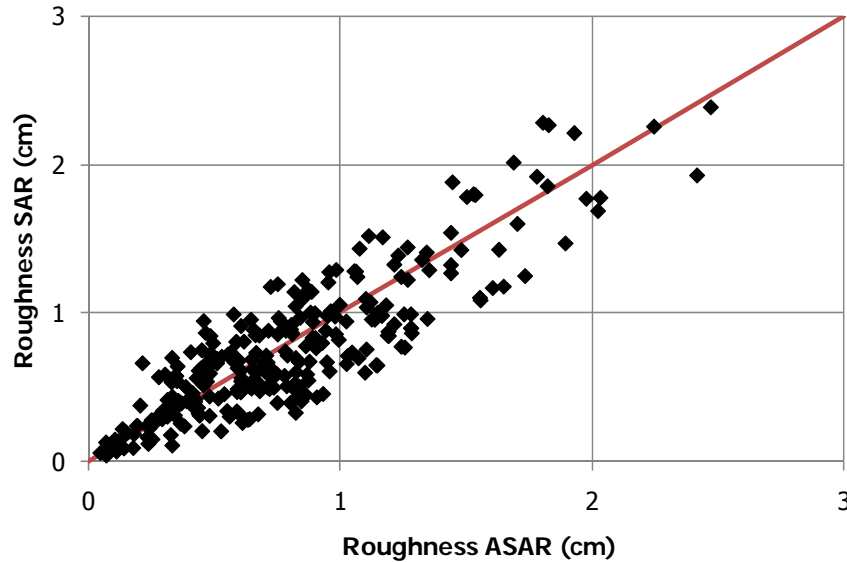


Figure 5.3. Comparison of the soil surface roughness values obtained from the Data Sets I and II after 2nd level of reduction

From Figures 5.4 and 5.5, it is examined that the observed backscatter coefficients have a logarithmic relationship with the computed roughness values. After taking natural base logarithms of roughness values and performing a linear regression analysis, Equations 5.6 and 5.7 are evaluated for backscatter – roughness relationships of the SAR and ASAR images with high coefficient of correlation values of 0.72 and 0.77, respectively. Similar relationships are also developed by Leconte et al. (2004) and Zribi and Dechambre (2002). Moreover, since both the SAR and ASAR images are acquired with a 5.3 GHz frequency and have similar incidence angles, the computed regression equations are almost identical.

$$\sigma_{SAR} = -9.21 + 2.89 \ln (h) \quad [r = 0.72] \quad (5.6)$$

$$\sigma_{ASAR} = -9.11 + 2.84 \ln (h) \quad [r = 0.77] \quad (5.7)$$

where:

σ is radar backscatter (dB)

h is soil surface roughness (cm)

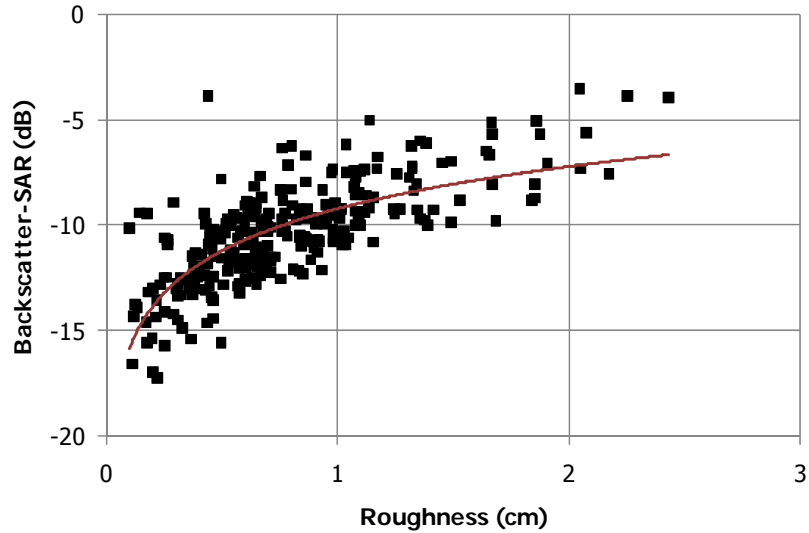


Figure 5.4. Backscatter – Roughness relationship for the Data Set I - SAR

Finally, the radar backscatter – soil roughness relationships (Equations 5.6 and 5.7) are used in the inverse order to compute soil surface roughness values of the Kurukavak catchment. This procedure is carried out for bare soil and/or sparsely vegetated farmland and pasture fields of the basin for 09-Oct-2004, 18-Dec-2004 and 20-Aug-2005 field study dates.

Due to dense vegetation condition of the basin on 07-May-2005, the roughness values computed for 18-Dec-2004 and 20-Aug-2005 field study dates are employed depending on the land use type;

- *Farmland*, by assuming no plowing (no change in roughness value) during spring, the roughness values computed for farmland land use class on 18-Dec-2004 are used,

- *Pasture*: by assuming no change in roughness values during summer, the roughness values computed for pasture land use class on 20-Aug-2005 are used.

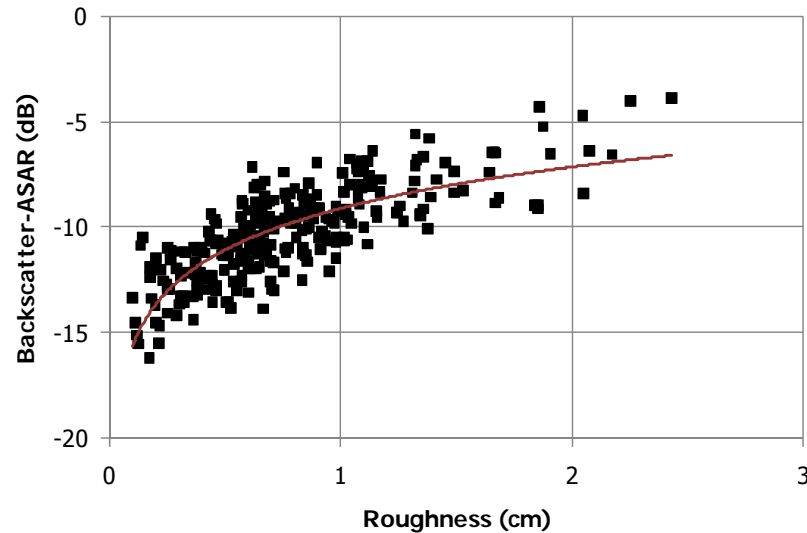


Figure 5.5. Backscatter – Roughness relationship for the Data Set II - ASAR

During the computation of surface roughness values, the limitations of the developed technique are also considered by eliminating farm and pasture areas which have;

- i) computed roughness values greater than Dubois model range ($h > 3.0$ cm) and/or
- ii) difference in the computed roughness values from the SAR and ASAR images are greater than the selected threshold value ($\Delta h > 0.5$ cm).

Since the computed roughness values of the basin are utilized by the first and the second soil moisture estimation methods, which are discussed in Chapter 6 of the study, the third method of soil moisture estimation is used for the areas where roughness values are not calculated during this analysis.

CHAPTER 6

SURFACE SOIL MOISTURE

Surface soil moisture condition of a watershed plays a significant role in separation of infiltration and surface runoff, and hence is a key parameter for the majority of physical hydrological models. Due to the sensitivity of dielectric constant of soil to water, microwave remote sensing (particularly the commonly available synthetic aperture radar) is a very potential tool for such studies. One of the major goals of this study is to obtain distributed surface soil moisture maps of the Kurukavak catchment, which can be further used as an input to a hydrological model. This is achieved for the field study dates of 09-Oct-2004, 18-Dec-2004, 07-May-2005 and 20-Aug-2005, and two soil moisture maps are obtained for each day, from the SAR and ASAR images of the basin, respectively.

The development and application steps of three different methodologies, which are used to derive distributed soil moisture grids, are discussed in this chapter of the study. These methods are utilized depending on the land use class and vegetation cover condition of the basin;

Method I – Backscatter Correction Factors, is used for the farmland and pasture fields of the basin for 09-Oct-2004, 18-Dec-2004, and 20-Aug-2005 dates when these areas have almost no vegetation cover. First, a nonlinear model relating radar backscatter with roughness, moisture and local incidence angle is developed with the point soil moisture measurements, which is then used to compute backscatter correction factors that are applied to the other farmland and pasture fields of the basin.

Method II – Water Cloud Model, is used for the farmland and pasture fields of the basin for 07-May-2005 when these areas are under dense vegetation cover. In this method, a semi-empirical backscatter model, the Water Cloud Model, is used in conjunction with the relationships developed for the first methodology.

Method III – Basin Indexes, is used for the forested areas of the basin for the field study dates of 09-Oct-2004, 18-Dec-2004, 07-May-2005 and 20-Aug-2005. Since radar waves could not penetrate through dense forest cover, radar images are impractical for moisture estimation in these areas. Hence, topographic index and solar radiation index of the basin are used to develop a relationship between soil moisture and these two basin indexes.

6.1. Method I – Backscatter Correction Factors

This method is applied to the farmland and pasture fields of the basin, for the field study dates of 09-Oct-2004, 18-Dec-2004, and 20-Aug-2005, when these areas have bare or sparsely vegetated land cover. As a result, since effect of vegetation is eliminated, radar backscatter depends only on the incidence angle, surface roughness and soil moisture. Considering the fact that wavelength of radar beams and polarization property of the acquired images are identical, and radar backscatter (σ);

- is directly correlated with *surface soil moisture* (m_v) (Quensay et al., 2000; Haider et al., 2004)
- is correlated with square root of *local incidence angle* (θ_L) (Goyal et al., 1999)
- is correlated with logarithm of *surface roughness* (h) (Leconte et al., 2004; Zribi and Dechambre, 2002) as obtained in the fifth chapter of this study,

a non-linear relationship is proposed as in Equation 6.1.

$$\sigma = a + b m_v + c \sqrt{\theta_L} + d \ln h \quad (6.1)$$

where;

a, b, c, d are constants

m_v is volumetric soil moisture ($m^3 m^{-3}$)

θ_L is local incidence angle (radian)

h is soil surface roughness (cm)

In the non-linear regression analysis of Equation 6.1, data from the 258 point soil moisture measurement locations (reduced by two levels as discussed in Chapter 5.2) for the 09-Oct-2004, 18-Dec-2004, and 20-Aug-2005 field study dates are used. Similar to the procedure handled for roughness analysis, two separate regression analyses are performed; for Data Set I-SAR and Data Set II-ASAR. Summary of source of the parameters used in the two data sets are tabulated in Table 6.1.

Table 6.1. Summary of parameters used in the regression analysis

Parameter	Data Set I-SAR	Data Set II-ASAR
Number of points	258	
Dates	09-Oct-2004, 18-Dec-2004 and 20-Aug-2005	
Radar Backscatter (dB)	From SAR imagery (Equation 4.8 and 4.9)	From ASAR imagery (Equation 4.8 and 4.9)
Local Incidence Angle (radian)	Topography and SAR imagery (Equation 4.7)	Topography and ASAR imagery (Equation 4.7)
Surface Soil Moisture ($m^3 m^{-3}$)	From point soil moisture measurements	
Soil Surface Roughness (cm)	From inversion of Dubois Model (Equation 5.5)	

In this part of the study, two versions of the proposed Equation 6.1 are analyzed;

i) wet soil backscatter relationship, $\sigma_{\text{bare-soil wet}} = f(m_v, \theta_L, h)$; is developed by assuming that radar backscatter (σ) is correlated with: roughness (h), moisture (m_v) and local incidence angle (θ_L). Two separate relationships are derived; Equation 6.2

for Data Set I-SAR and Equation 6.3 for Data Set II-ASAR with both having a high correlation coefficient value of 0.93.

$$[\text{SAR}] \sigma_{\text{bare-soil wet}} = 5.72 + 11.16 m_V - 26.78 \sqrt{\theta_L} + 4.92 \ln(h) \quad (6.2)$$

$$[\text{ASAR}] \sigma_{\text{bare-soil wet}} = 6.21 + 8.39 m_V - 26.87 \sqrt{\theta_L} + 4.70 \ln(h) \quad (6.3)$$

The graphical representations of the Equations 6.2 and 6.3, on which the observed backscatter values are plotted with respect to the computed ones using the derived relationships, are given in the Figures 6.1 and 6.2 for the SAR and ASAR images, respectively. The bare soil backscatter relationship is also employed in the second methodology of soil moisture estimation, in the Water Cloud Model.

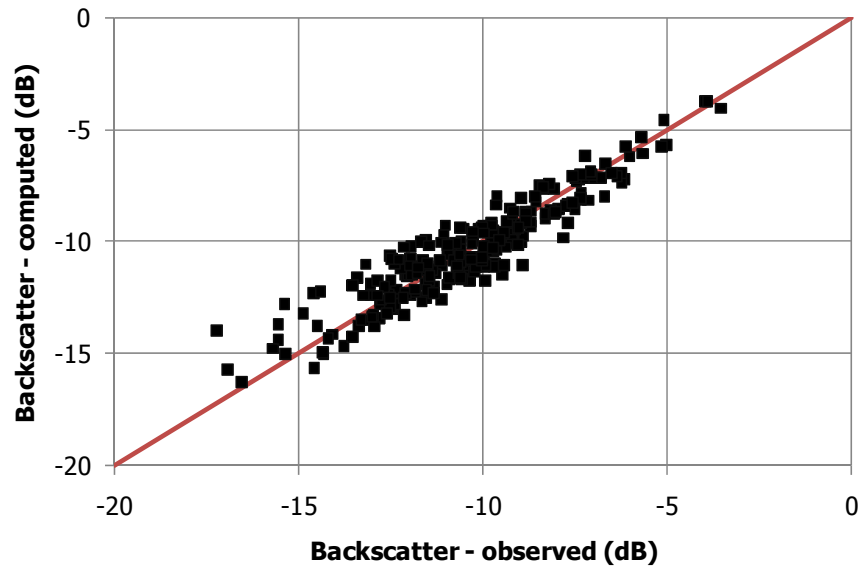


Figure 6.1. Computed vs. observed backscatter values for the Data Set I-SAR

ii) **dry soil backscatter relationship**, $\sigma_{\text{bare-soil dry}} = f(\theta_L, h)$; is developed by assuming that radar backscatter (σ) is correlated only with: roughness (h) and local incidence angle (θ_L), and, it is independent of soil moisture (m_V). Similar to the wet soil case, two separate relationships are derived; Equation 6.4 for Data Set I-SAR

and Equation 6.5 for Data Set II-ASAR, with correlation coefficient values of 0.87 and 0.89 , respectively.

$$[\text{SAR}] \sigma_{\text{bare-soil dry}} = 7.40 - 26.48 \sqrt{\theta_L} + 4.81 \ln(h) \quad (6.4)$$

$$[\text{ASAR}] \sigma_{\text{bare-soil dry}} = 7.42 - 26.27 \sqrt{\theta_L} + 4.62 \ln(h) \quad (6.5)$$

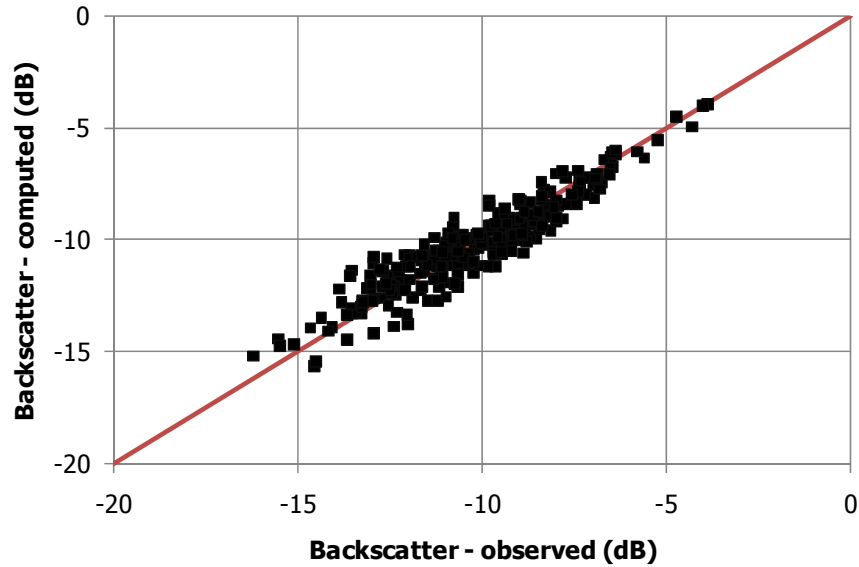


Figure 6.2. Computed vs. observed backscatter values for the Data Set II-ASAR

In the computation of backscatter correction factors (C) Equation 6.6, which is proposed by Goyal et al. (1999), is used on a pixel by pixel basis.

$$C = \frac{\sigma_{\text{reference}}}{\sigma_{\text{actual}}} \quad (6.6)$$

where;

$\sigma_{\text{reference}}$ is the reference backscatter value (dB) computed by using *dry soil backscatter relationship* (Equation 6.4 or 6.5) and by assuming flat and smooth surface ($h = 0$ and incidence angle, θ , is used instead of local incidence angle, θ_L)

σ_{actual} is the actual backscatter value (dB) computed for that pixel using *dry soil backscatter relationship* (Equation 6.4 or 6.5) but with the actual surface roughness ($h \neq 0$) and local incidence angle (θ_l) values

The correction factors, which are computed for each pixel, are then used to calculate the corrected backscatter values ($\sigma_{\text{corrected}}$) with Equation 6.7.

$$\sigma_{\text{corrected}} = \sigma_{\text{observed}} \times C \quad (6.7)$$

where;

σ_{observed} is the observed backscatter value in radar image (dB)

$\sigma_{\text{corrected}}$ is the corrected backscatter value (dB),

C is the correction factor obtained from Equation 6.6

Since the dry soil backscatter relationship is used in Equation 6.6, the correction factors remove only the effects of topography and surface roughness. As a result, the corrected backscatter coefficients ($\sigma_{\text{corrected}}$) are highly correlated with the observed soil moisture (m_v) values (Figures 6.3 and 6.4).

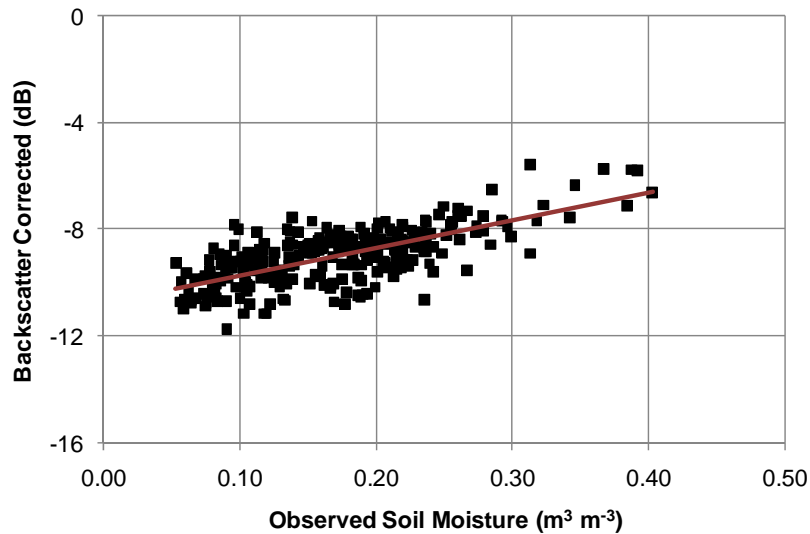


Figure 6.3. Corrected backscatter – observed soil moisture relationship for the Data Set I - SAR

For each data set, a relationship between the corrected backscatter ($\sigma_{\text{corrected}}$) and the observed soil moisture (m_v) values is obtained with linear regression analysis. Equations 6.8 and 6.9 represent these relationships for Data Set I-SAR and Data Set II-ASAR, with correlation coefficients of 0.69 and 0.62, respectively.

$$[\text{SAR}] \sigma_{\text{Corrected}} = - 10.74 + 10.29 m_v \quad [r=0.69] \quad (6.8)$$

$$[\text{ASAR}] \sigma_{\text{Corrected}} = - 10.24 + 7.87 m_v \quad [r=0.62] \quad (6.9)$$

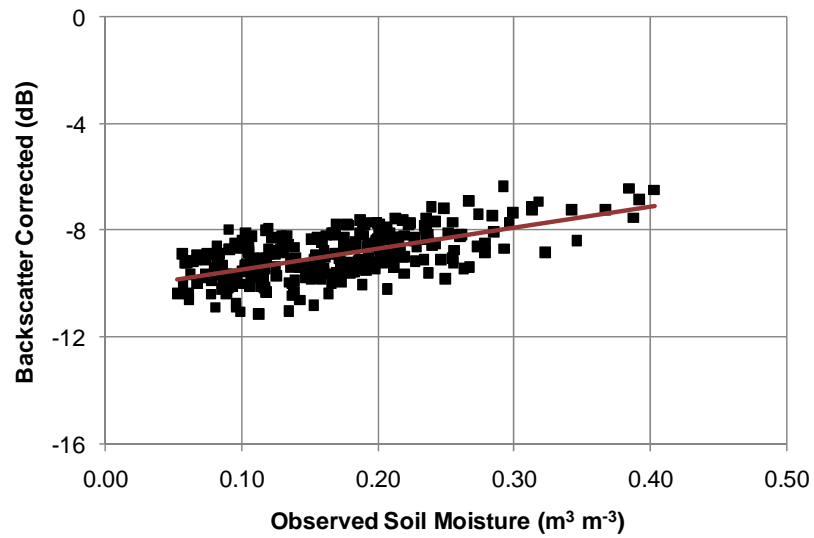


Figure 6.4. Corrected backscatter – observed soil moisture relationship for the Data Set II - ASAR

6.2. Method II – Water Cloud Model

Attema and Ulaby (1978) proposed a rather simple approach for modeling of backscatter from a vegetation canopy, known as the Water Cloud Model (WCM). Basic assumptions of this model are (Ulaby et al., 1981b; Bindlish and Barros, 2001) those:

- The vegetation is represented by a horizontal cloud of water spheres, which are uniformly distributed over the soil surface with the height of vegetation canopy.
- Multiple scattering between soil and vegetation, $\sigma_{veg+soil}^0$ in Equation 2.1, is neglected. As a result, the general equation of the Water Cloud Model is reduced to Equation 6.10.

$$\sigma_{can} = \tau^2 \sigma_{bare-soil} + \sigma_{vegetation} \quad (6.10)$$

where;

σ_{can} is the backscatter from the vegetation canopy (m^2/m^2)

$\sigma_{bare-soil}$ is the backscatter contribution of the bare soil under the vegetation canopy (m^2/m^2)

τ^2 is the two-way attenuation of the vegetation layer (effect of vegetation on bare soil backscatter values)

$\sigma_{vegetation}$ is the direct backscatter contribution of the vegetation layer (m^2/m^2)

$$\tau^2 = \exp(-2 B W_c \sec\theta_L) \quad (6.11)$$

$$\sigma_{vegetation} = A W_c \cos\theta_L (1 - \tau^2) \quad (6.12)$$

where;

A, B are parameters depending on vegetation type

W_c is the vegetation water content (kg/m^3)

θ_L is the local incidence angle (radian)

The Normalized Difference Vegetation Index (NDVI) is a commonly used vegetation index, representing the vegetation condition of an area on a scale from 0 (no vegetation) to 1 (dense vegetation). In the computation of vegetation water content

(W_C) of the study basin, the relationship between W_C and NDVI, which is proposed by Jackson et al. (1999), is used.

$$W_C = 1.9134 (\text{NDVI})^2 - 0.3215 (\text{NDVI}) \quad (6.13)$$

The NDVI is calculated as a ratio between measured reflectivity in the red and near infrared portions of the electromagnetic spectrum (Equation 6.14). These two spectral bands are chosen because they are most affected by the absorption of chlorophyll in leafy green vegetation and by the density of green vegetation on the surface. Also, in red and near-infrared bands, the contrast between vegetation and soil is at a maximum (Lilesand and Kiefer, 1999).

$$\text{NDVI} = (\text{NIR} - \text{Red}) / (\text{NIR} + \text{Red}) \quad (6.14)$$

where;

NIR = Near Infra-Red Band (Quickbird Band 4: 760 – 900 nm)

Red = Red Band (Quickbird Band 3: 630 – 690 nm)

The high resolution Quickbird image of the Kurukavak basin (Figure 3.2), acquired on 06-May-2006 is used to compute the distributed NDVI values of the study site. Similar to the other grid based data used in this study, the NDVI grid, which is computed for 0.60 m resolution, is resampled to 30 m and presented in Figure 6.5.

Even if there exists a one year period between the Quickbird image on 06-May-2006 and the SAR and ASAR imagery on 07-May-2005, the calculated NDVI map is used in the modeling of radar backscatter – soil moisture relationship for 07-May-2005 field study date. This is based on the assumption that vegetation cover/growth within the basin depends only on the day of the year and variations from one year to another year are negligible. Moreover, from field studies performed in the catchment, a significant change in the vegetation cover is observed from 07-May-2005 to 11-Jun-2005. As a result, among the field study dates (Table 4.2), on which both the SAR and ASAR images are acquired, only radar imagery from 07-May-2005 is used in the second methodology of surface soil moisture estimation.

In this part of the study a procedure, which utilizes the Water Cloud Model with a delta index approach, is applied to the farm and pasture areas of the Kurukavak basin for the 07-May-2005 dated SAR and ASAR images. The procedure is discussed in a stepwise manner below:

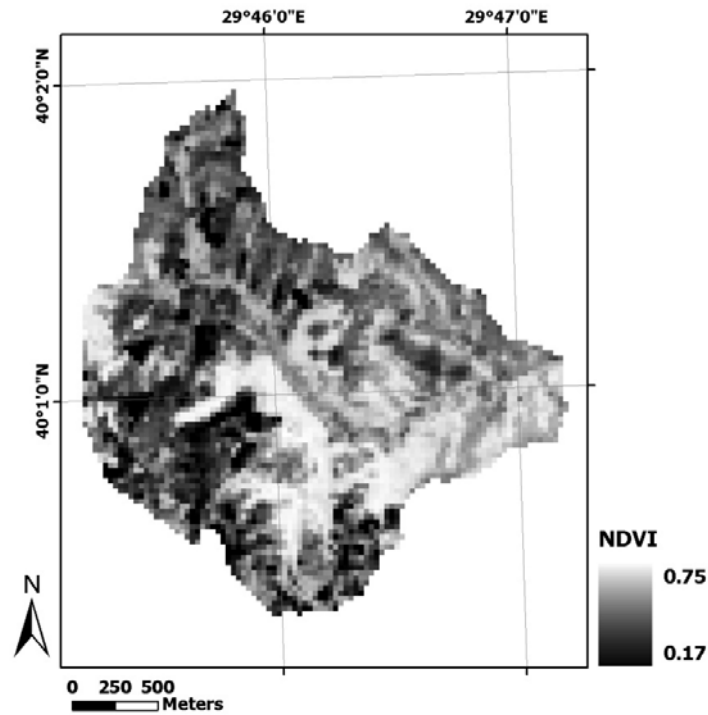


Figure 6.5. The Normalized Difference Vegetation Index grid of the Kurukavak basin

i) First, the unknown parameters A and B in the Water Cloud Model are estimated. Similar to the previous analyses, two separate data sets are prepared for the SAR and ASAR images, respectively. Each data set includes 94 point soil moisture measurement locations of 07-May-2005 field study date, which is reduced from initial 126 points as discussed in Chapter 5.2 of the study.

Then, *bare-soil backscatter* ($\sigma_{\text{bare-soil}}$) value in Equation 6.10 of WCM is computed using the *wet soil backscatter relationship* obtained in the first methodology; Equations 6.2 and 6.3 derived for $\sigma_{\text{bare-soil wet}} = f(m_v, \theta_L, h)$ relationship.

For the two data sets, two non-linear regression analyses are performed and similar A and B values are obtained for both of them. Since A and B parameters represent the geometrical properties of the scattering elements in the vegetation canopy (Ulaby et al., 1981b), these values are independent from radar sensor characteristics. Hence, for both of the radar images; SAR and ASAR, A and B values are calculated as 0.284 and 0.109, respectively. On a mix of land use classes: rangeland, wheat and pasture, Bindlish and Barros (2001) have determined the same values as 0.0012 and 0.091. Moreover, Moran et al. (1998) have calculated the A and B values on agricultural fields as 0 and 0.09

ii) Secondly, in order to investigate the accuracy of the WCM, the modeled *canopy backscatter* (σ_{can}) values of the 94 points are computed by using the WCM. In these computations, the A and B values estimated in the first step and the wet soil backscatter relationship are employed; $A = 0.284$, $B = 0.109$ and $\sigma_{\text{bare-soil wet}} = f(m_V, \theta_L, h)$.

Then the observed backscatter values from the 07-May-2005 SAR and ASAR images are compared with the computed canopy backscatter values (σ_{can}) from WCM. The plots of observed versus computed backscatter values for Data Set I-SAR and Data Set II-ASAR are given in Figures 6.6 and 6.7, and the correlation coefficient values of these relationships are calculated as 0.64 and 0.63, respectively.

iii) Prior to applying the delta index approach, *dry soil canopy backscatter* ($\sigma_{\text{can-dry}}$) values, by assuming dry soil surface condition under the same vegetation canopy, are calculated for the 94 points by using the WCM. In the computation of $\sigma_{\text{can-dry}}$;

- Similar to the computation of σ_{can} in the second step; A and B values, which are estimated in the first step ($A = 0.284$ and $B = 0.109$), are employed.
- Different from the computation of σ_{can} in the second step; the *dry soil backscatter relationship*, which does not take account of soil moisture, is used. Hence, Equations 6.4 and 6.5 from the first method, are utilized for the $\sigma_{\text{bare-soil dry}} = f(\theta_L, h)$ relationship.

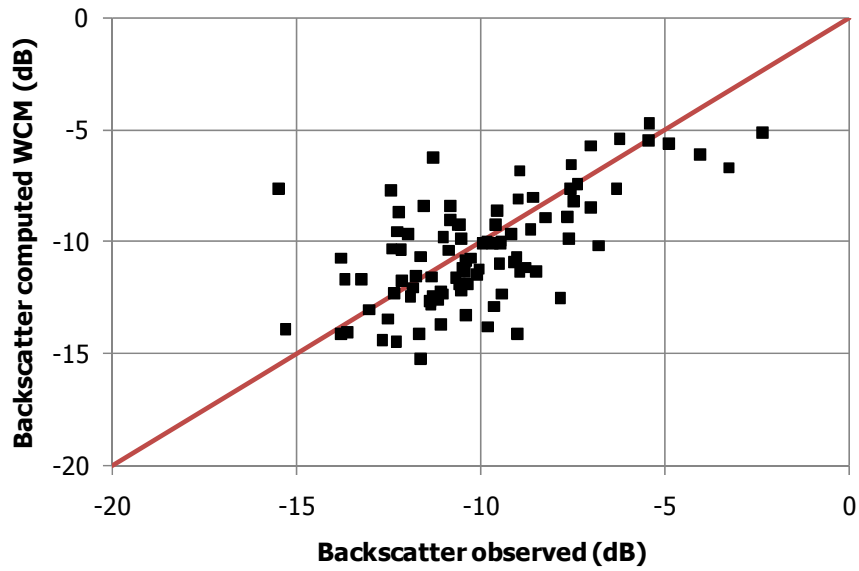


Figure 6.6. Observed vs. computed (σ_{can}) canopy backscatter values from the WCM for the Data Set I-SAR

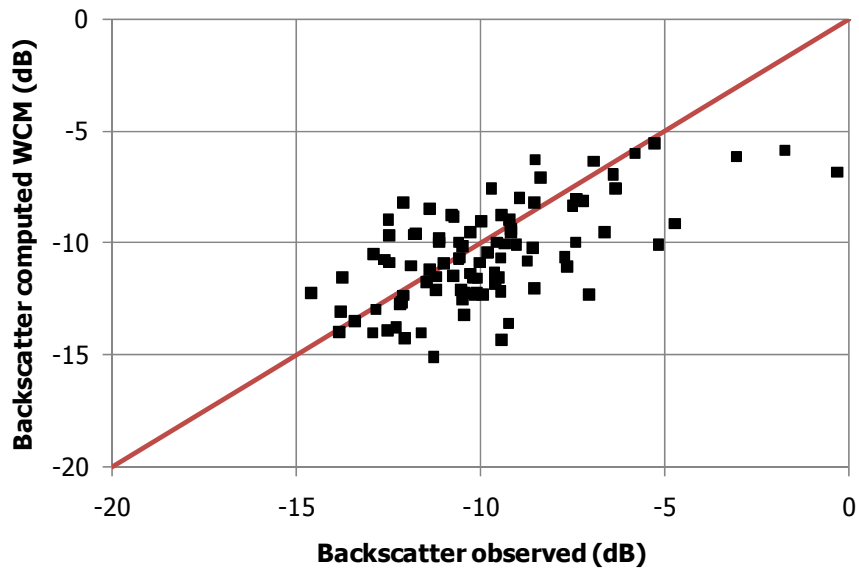


Figure 6.7. Observed vs. computed (σ_{can}) canopy backscatter values from the WCM for the Data Set II-ASAR

iv) Finally, a delta index ($\Delta\sigma$) value is calculated for the 94 point soil moisture measurement locations by computing the difference between the observed backscatter (σ_{observed} from the SAR and ASAR images of 07-May-2005) and the computed dry soil canopy backscatter values ($\sigma_{\text{can-dry}}$ from step 3), as in Equation 6.15.

$$\Delta\sigma = \sigma_{\text{observed}} - \sigma_{\text{can-dry}} \quad (6.15)$$

Since the only difference between the observed backscatter and the dry soil canopy backscatter values is soil moisture, the calculated delta values are expected to be correlated with surface soil moisture. This approach is examined by plotting the computed delta values ($\Delta\sigma$) with respect to the observed volumetric soil moisture values (m_v). The plots for the Data Set I-SAR and Data Set II-ASAR are given in Figures 6.8 and 6.9, respectively.

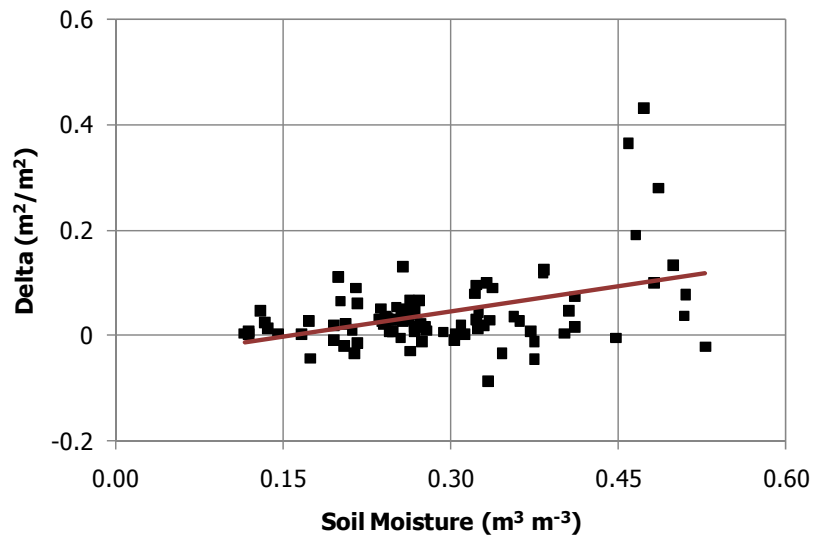


Figure 6.8. Relationship between delta ($\Delta\sigma$) and soil moisture (m_v) for the Data Set I-SAR

In order to obtain a relationship between the computed delta values ($\Delta\sigma$) and the observed soil moisture values (m_v), simple linear regression analyses are carried out

for the values presented in Figures 6.8 and 6.9, for SAR and ASAR data sets. The computed relationships are given in Equations 6.16 and 6.17, and the correlation coefficient values of these relationships are calculated as 0.42 and 0.45, respectively.

$$\Delta\sigma_{\text{SAR}} = -0.0511 + 0.3197 m_v \quad [r=0.42] \quad (6.16)$$

$$\Delta\sigma_{\text{ASAR}} = 0.2191 + 0.2418 m_v \quad [r=0.45] \quad (6.17)$$

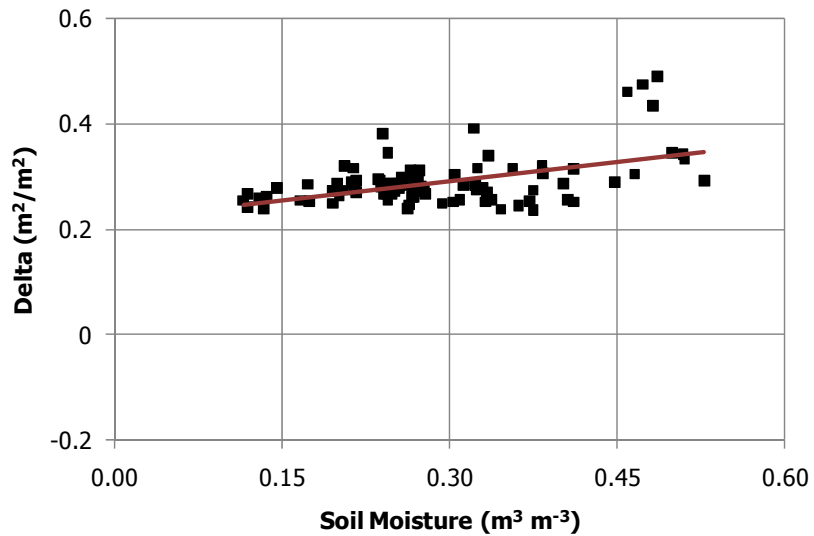


Figure 6.9. Relationship between delta ($\Delta\sigma$) and soil moisture (m_v) for the Data Set II-ASAR

6.3. Method III – Basin Indexes

The third method of the study is developed by using the point soil moisture measurements collected during all nine field studies, and it is utilized for the soil moisture mapping of the forested areas of the Kurukavak basin. In microwave remote sensing studies, forests are represented by a much thicker and denser vegetation canopy than farmland and pasture fields, and, rather than the physical properties of the soil surface, observed backscatter is dominated by the canopy

itself. As a result, radar images are impractical for surface soil moisture estimation in these areas.

Other than radar backscatter, soil moisture can be correlated to certain characteristics of the basin, such as terrain. Developing such a relationship can be used in spatial scaling of soil moisture. Terrain data is generally used to calculate patterns of substitute variables, like wetness and radiation indexes, which are used to estimate spatial pattern of soil moisture (Western et al., 2002). Moreover, Western et al. (1999) analyzed the spatial variations of soil moisture in Tarrawarra catchment of Australia, and found that the highest correlation ($r^2=0.61$) is observed when wetness index is combined with a radiation index.

The most commonly used terrain index is the topographic wetness index, proposed by Beven and Kirkby (1979). The Topographic Index grid of the study area is calculated from the Digital Elevation Model (DEM) of the Kurukavak basin (Figure 3.1) on a cell by cell basis by using Equation 6.18, and presented in Figure 6.10.

$$[\text{Topographic Index}] \quad TI = \ln \frac{\sum A_i}{\tan \beta_i} \quad (6.18)$$

where;

$\sum A_i$ is the upstream drainage area of the i^{th} cell

β_i is the surface slope at the i^{th} cell

The potential solar radiation, R_o , is the radiation received at a sloping surface in the absence of the atmosphere. It is expressed by Equation 6.19, which can be numerically integrated over any period of time to estimate the solar radiation potential of that period. The variation of potential solar radiation over a catchment depends only on the slope, aspect and the time of the year (Moore et al., 1993).

$$R_o = \frac{24 I}{\pi r^2} \cos \phi \cos \delta (\sin \eta - \eta \sin \eta) \quad (6.19)$$

where;

I is the solar constant, which is the average radiation flux on a plane perpendicular to the solar beam at the upper surface of the atmosphere, 1367 W m^{-2} (Dingman, 2002)

δ is the solar declination, which is the latitude at which the sun is directly overhead at noon, due to the 23.5° tilt of the earth's rotational axis. This value changes regularly from $+23.5^\circ$ to -23.5° as the earth rotates around the sun (Dingman, 2002)

r is the ratio of earth sun distance to its mean

Φ , η are functions of the terrestrial latitude and topographic attributes (slope and aspect)

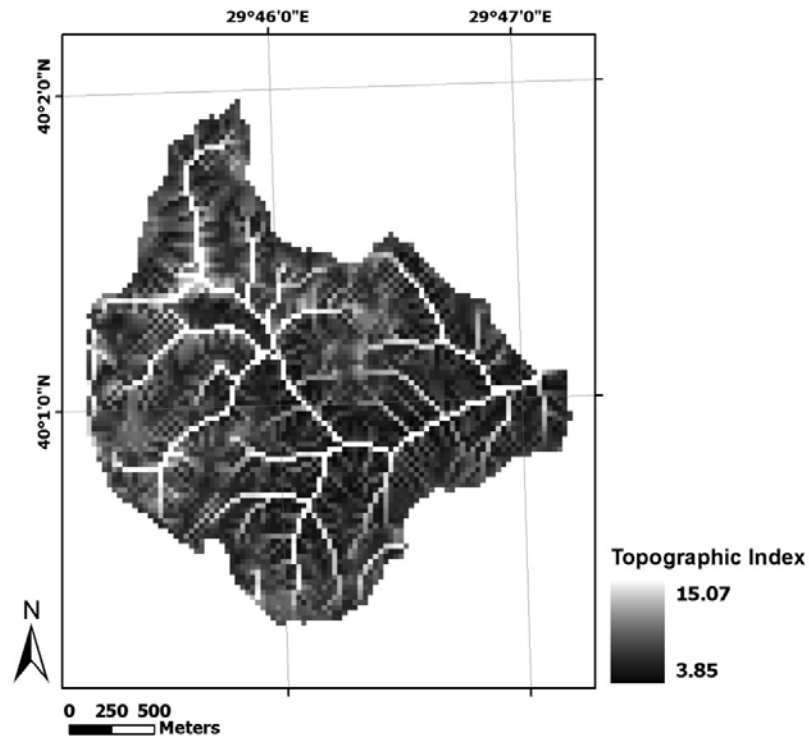


Figure 6.10. Topographic Index (TI) grid of the Kurukavak basin

The potential Solar Radiation Index (SRI) is defined as the ratio of radiation received on a sloping surface (R_0) to that received on a horizontal surface (R_{OH}) in the absence of atmospheric effects and calculated using Equation 6.20. It is a

measure of the spatial variation in solar radiation due to the effect of slope and aspect (Western et al., 2004).

$$[\text{Solar Radiation Index}] SRI = \frac{R_O}{R_{OH}} \quad (6.20)$$

In this study, daily total solar radiation (R_O) grids of the study catchment are calculated for all (9) field study dates (Table 3.3). The grids are determined by utilizing the slope map of the basin and total radiation received by each cell is computed for the 24 hour period of the day. For this purpose, hourly solar radiation values are computed with Equation 6.19 which are then integrated over time. Then, daily total solar radiation values are recomputed by assuming the whole basin as flat -slope is equal to 0- (R_{OH}). Finally, the solar radiation index (SRI) grids are obtained using Equation 6.20. As an example, the SRI grid derived for 09-Oct-2004 is shown in Figure 6.11.

Between the soil moisture (m_v) and the two basin indexes (TI and SRI) a linear relationship is proposed as in Equation 6.21.

$$m_v = a + b \text{ SRI} + c \text{ TI} \quad (6.21)$$

where; a, b and c are constants

In the linear regression analysis of Equation 6.21, the 126 point soil moisture measurement locations are employed. Since this method does not depend on radar imagery, a total of 9 field study dates and 1134 measurement values are used. The topographic index and solar radiation index values are extracted from the computed grids, and the linear relationship given in Equation 6.22 is obtained with a coefficient of correlation value of 0.79. The observed and computed soil moisture values are plotted with respect to each other in Figure 6.12. It is observed from the figure that Equation 6.22 results in higher moisture values for dry soil condition and lower moisture values for wet soil condition.

$$m_v = 0.048 + 0.185 \text{ SRI} + 0.014 \text{ TI} \quad [r=0.79] \quad (6.22)$$

6.4. Mapping Surface Soil Moisture

The land use map of the Kurukavak basin (Figure 3.3) is digitized from the Quickbird image of the area with five land use classes; forest, farmland, pasture, road and urban, among which forest areas constitute 53.1 %, farmland and pasture fields cover 23.6 % and 21.9 % of the basin, respectively. For the three methods developed for soil moisture estimation, only Method II-WCM depends on vegetation by means of NDVI. However, it is also found out that the land use class (farm or pasture) has no significant effect on the vegetation parameters (A and B) of the WCM. Moreover, the land use classes of urban and road cover a very small percentage of the basin and areas within these classes are considered with the forest class. As a result, land use classes of the basin are grouped under two major classes; i) Forest and Other, ii) Farmland and Pasture, for surface soil moisture mapping.

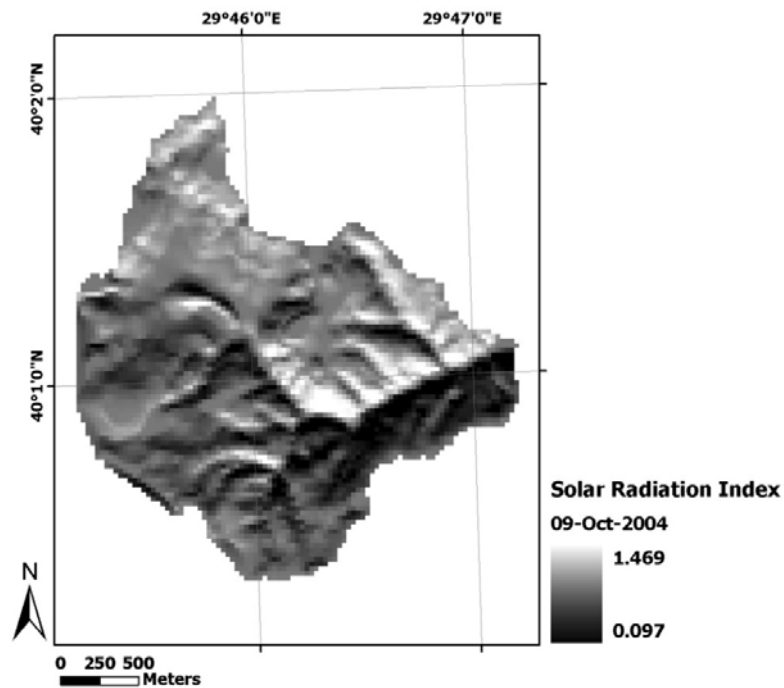


Figure 6.11. Solar Radiation Index (SRI) grid of the Kurukavak basin for 09-Oct-2004

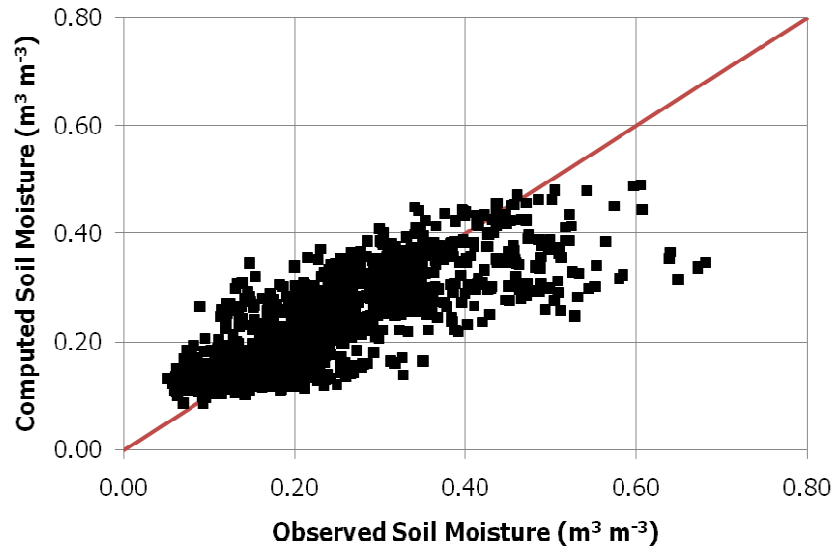


Figure 6.12. Observed vs. computed soil moisture values for the Method III

The land use map of the study catchment, representing the three major land use classes, is shown in Figure 6.13. The raster/grid type representation of the same information is derived from these data and presented in Figure 6.14. Similar to all raster data used during the study; backscatter coefficients, incidence angle, DEM, topographic index etc, land use data are computed with 30 m cell size, which is the general ground resolution of the study.

In addition to the cell size, all raster data of the study have exactly the same grid cell locations. Due to the computation requirements of the analyses, a *permanent raster model* is implemented for the whole basin. For this purpose, cell locations and cell size of the DEM are selected as the basis of the model. Then, these grid cells - and their center points- of the permanent raster model are assigned with a unique identification number (ID), which are used to form a common geo-database of the study. All of the raster datasets, created and used throughout this research, are calculated in a way to match the same cell locations of the permanent raster model. Then, unique cell IDs are used to extract the information from the raster dataset to the geo-database. This logic is also considered in the resampling process of point soil moisture measurement locations; from 68 to 126 points. Hence, the resampled

points and cells shown in Figure 3.7 for Plot 1 are obtained from the pre-defined permanent raster model of the study area. In addition, Figure 6.14 indicates a small portion of the land use raster where cell center locations are shown with points over the permanent raster model.

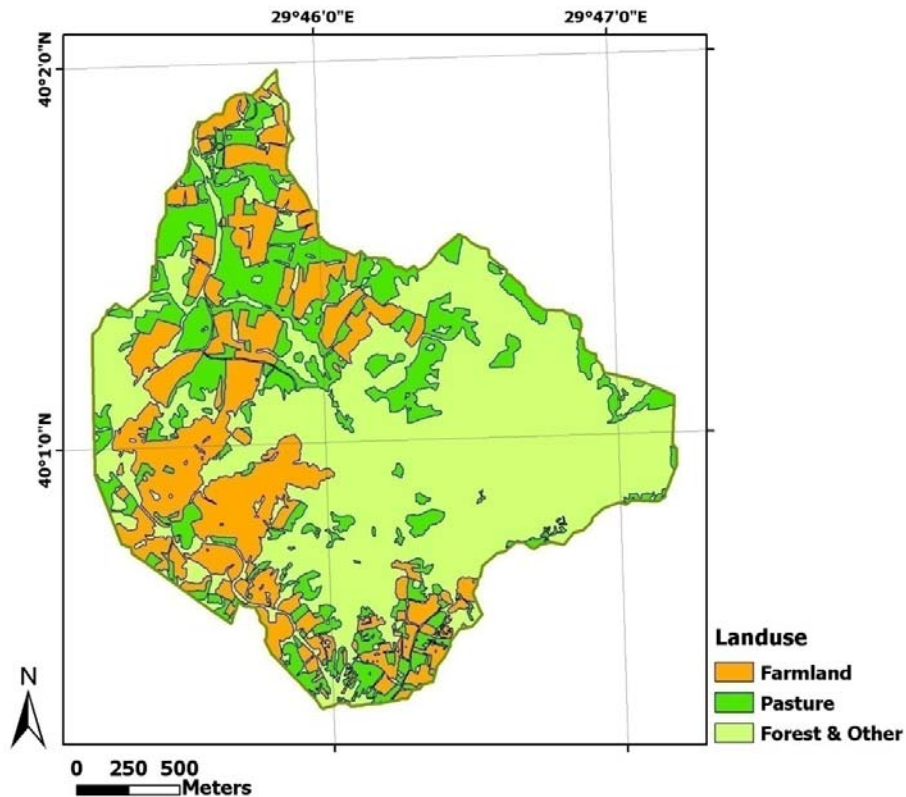


Figure 6.13. Land use map of the Kurukavak basin with major classes (vector)

Surface soil moisture mapping of the Kurukavak catchment is performed for the whole basin area and on a cell by cell basis. The permanent raster data model, having unique IDs, is utilized for this purpose. The cell IDs are used to extract necessary information; *backscatter coefficients, incidence and local incidence angles, DEM, slope, aspect, NDVI, topographic index, solar radiation index* etc., from the geo-database.

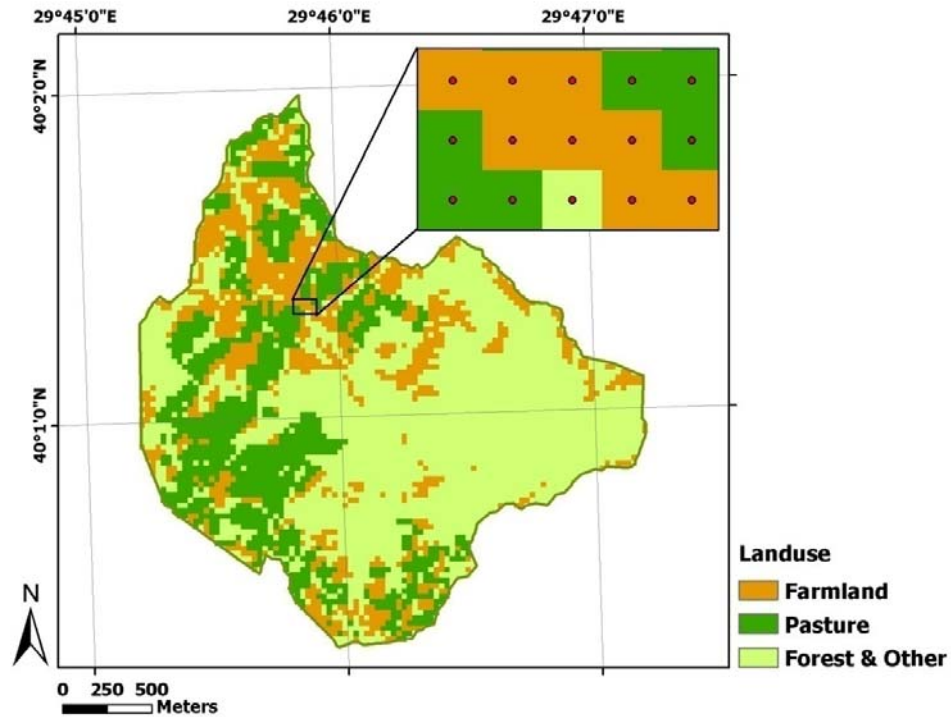


Figure 6.14. Land use map of the Kurukavak basin in permanent raster data model with cell centers as points

In the computation of surface soil moisture values of the Kurukavak catchment, the aforementioned three methods are used depending on the land use class and vegetation cover conditions of the area, which is summarized in Table 6.2. Moreover, computation of surface roughness values for the farmland and pasture areas of the basin; for 09-Oct-2004, 18-Dec-2004, 07-May-2005 and 20-Aug-2005 field study dates, is discussed in section 5.3 of this study.

The procedure applied for distributed soil moisture mapping of the catchment:

Method I – Backscatter Correction Factors:

- Dry soil backscatter relationship (Equation 6.4 and 6.5) is used to compute; actual (σ_{actual}) and reference ($\sigma_{\text{reference}}$) (assuming flat and smooth surface) backscatter values,

- Backscatter correction factors (C) are calculated for each raster cell by using Equation 6.6,
- Corrected radar backscatter ($\sigma_{\text{corrected}}$) values are obtained from Equation 6.7,
- Equations 6.8 and 6.9 are used to estimate surface soil moisture (m_v) value of each raster cell from the corrected backscatter values.

Table 6.2. Summary of the application of the soil moisture estimation methods

Date	Farmland & Pasture	Forest & Other	Figure Number SAR / ASAR
09-Oct-2004	Method I <i>BS Correction</i>	Method III <i>Basin Indexes</i>	B.1 / B.2
18-Dec-2004	Method I <i>BS Correction</i>	Method III <i>Basin Indexes</i>	B.3 / B.4
07-May-2005	Method II <i>WCM</i>	Method III <i>Basin Indexes</i>	B.5 / B.6
20-Aug-2005	Method I <i>BS Correction</i>	Method III <i>Basin Indexes</i>	B.7 / B.8

Method II – Water Cloud Model:

- Dry soil backscatter relationship (Equation 6.4 and 6.5) is used to compute the bare-soil backscatter ($\sigma_{\text{bare-soil}}$) values, which are then used in Equation 6.10 of WCM,
- Dry soil canopy backscatter ($\sigma_{\text{can-dry}}$) values are computed from WCM,
- Delta backscatter ($\Delta\sigma$) value of each raster cell is calculated by taking the difference between the observed (σ_{observed}) and the computed ($\sigma_{\text{can-dry}}$) backscatter values (Equation 6.15),
- Equations 6.16 and 6.17 are used to estimate surface soil moisture (m_v) value of each raster cell from the computed difference in backscatter ($\Delta\sigma$) values.

Method III – Basin Indexes:

- Equation 6.22 is employed to compute surface soil moisture (m_v) value of each raster cell from topographic index (TI) and solar radiation index (SRI) values.

The estimated surface soil moisture distributions of the Kurukavak catchment are presented from Figure B.1 to Figure B.8; for 09-Oct-2004, 18-Dec-2004, 07-May-2005 and 20-Aug-2005 field study dates and for the SAR and ASAR images. Throughout Chapter 6, the volumetric soil moisture values (m_v values in both the graphs and equations) are given in $m^3 m^{-3}$ units (on a range from 0 to 1), but in order to have better graphical representation in mapping of soil moisture, these values are multiplied by 100 and given in units of *percentages (%)* which is on a range from 0 to 100.

Moreover, frequency histograms of the computed soil moisture distributions are calculated for:

- i) the whole basin,
- ii) the farmland and pasture fields of the basin, where soil moisture values are calculated with Method I and II,
- iii) the forest and other land use types, where soil moisture values are computed with Method III.

which are then compared with the frequency histogram of the observed soil moisture measurements of the same day (from Figure C.1 to Figure C.8). Similar to the soil moisture distribution maps, the frequency histograms are calculated for the volumetric soil moisture values in the units of percentages (%).

In the computation of the frequency histograms, equal bins of 1 % length are selected from 0 % to 60 % for volumetric soil moisture. After calculating the number of points within each bin, frequency of the bin is evaluated by dividing this bin value with the total number of points. It is then multiplied with 100 to obtain the

frequency value in percentages. For the point soil moisture measurements, the total number of points, which is used in this computation, is 126. On the other hand, the total number of points used in the frequency analysis of the entire catchment is 5258; 2392 points from farmland and pasture, 2866 points from forest and other land use classes. As mentioned previously, these points refer to the cell center locations of the permanent raster data model (Figure 6.14), which has a ground resolution of 30 m.

Finally, statistical parameters; such as mean, standard deviation etc., of the volumetric soil moisture distributions are calculated for:

- i) the entire basin,
- ii) the farmland and pasture fields of the basin, where soil moisture values are calculated with Method I and II,
- iii) the forest and other land use types, where soil moisture values are computed with Method III.

which are also compared with the calculated statistical parameters of the observed soil moisture measurements of the same day (Tables C.1, C.2, C.3 and C.4). Similar to the soil moisture distribution maps, these statistical parameters are calculated for the volumetric soil moisture values in the units of percentages (%).

CHAPTER 7

LUMPED AND SEMI-DISTRIBUTED HYDROLOGICAL MODEL SIMULATION

In addition to the point rainfall measurements, the General Directorate of Agricultural Research of Turkey has been measuring runoff at the Kurukavak basin outlet. For this purpose, a V-notch weir was built at the basin outlet and discharge measurements have been carried out with a float-type stage gage. The runoff data recorded by this gage and the rainfall data collected by the Directorate for the Kurukavak basin are not evaluated within the scope of this study.

During the field studies in the Kurukavak basin, a rainfall and runoff measuring station is installed at the basin outlet on 28-Apr-2005. The station is composed of three major parts which are assembled on a single pole;

- A tipping bucket type rainfall gage,
- A pressure sensor, installed behind the weir for measuring water stage,
- A data logger.

From 28 April to 11 June of 2005, the station collected rainfall and stage data with 5-minute time increments. The rainfall gage records the total amount of precipitation and the pressure sensor records the average stage value within each time step. Then, by visiting the station during field studies, the collected data are downloaded from the data logger. During this period, a major flood event on 1st of June 2005 is recorded with a peak discharge value of 9.97 m³/s.

The third major goal of this study is to perform a semi-distributed hydrological analysis with a distributed input of surface soil moisture. For this reason, a hydrological model, which has the capabilities of:

- i) accepting distributed input parameters
- ii) performing distributed (cell by cell) hydrological analysis,

Hydrologic Engineering Center – Hydrologic Modeling System (HEC-HMS) is selected. The Hydrologic Modeling System is designed to simulate the precipitation-runoff processes of watershed systems. It is also designed to be applicable in a wide range of geographic locations for solving different water related problems. This includes large river basin water supply and flood hydrology, and small urban or natural watershed runoff (HEC, 2008).

The flood event on 1-Jun-2005 is simulated with the HMS model by considering a time window of one month;

- i) starting from 07-May-2005 at 10:00; the actual time of SAR and ASAR image acquisitions, hence the time of computed soil moisture distributions of the basin,
- ii) ending at 06-Jun-2005 at 10:00; when the flood recession is completed.

First, the distributed soil moisture grids of the Kurukavak basin are used as an input parameter of the HEC-HMS model. The soil moisture values computed from the 07-May-2005 SAR image are used in the calibration of undetermined HMS parameters. Then the calibrated parameters are utilized to simulate the same flood event; first by using the soil moisture distribution calculated from the 07-May-2005 ASAR image, and then by accepting an average (lumped) soil moisture value for the whole basin on 07-May-2005, which is the average of field soil moisture measurements. In other words, three different model simulations of the 1-Jun-2005 flood event, which are listed below, are carried out.

I) Distributed SAR: with initial soil moisture from the SAR image of 07-May-2005, also used for calibration of model parameters,

II) Distributed ASAR: with initial soil moisture from the ASAR image of 07-May-2005,

III) Lumped: with initial soil moisture from field measurements, a single value is accepted for the whole basin.

7.1. Calibration of Model Parameters

Developed by United States' Army, the HMS model is designed to be used with the national grid standards of the United States, and the model only accepts grids having ground resolution of 10 m, 20 m, 50 m, 100 m, 200 m, 500 m, 1000 m etc. In order to comply with these requirements, the ground resolution of all distributed (gridded) datasets of the study are set to 50 m, which is the nearest higher ground resolution to the 30 m base resolution used throughout the study. Prior to model simulation with HMS, the computed soil moisture grids are resampled to 50 m. After building the HEC-HMS model with the initial assumption of parameters and the rainfall-runoff data, model parameter calibration is carried out by;

- i) performing the sensitivity analysis of undetermined model parameters; by keeping all other parameters constant and observing the effect of change in the selected parameter on the model outcomes,
- ii) estimation of undetermined parameters by trial and error procedures.

Similar to other physical models, HEC-HMS is a component based model, in which the actual hydrological processes within the study area are represented by a number of interacting components. Each component is responsible for a single hydrological process; infiltration, evaporation etc., and the HMS components which are utilized in this study are discussed below.

Deficit and Constant Loss:

The deficit and constant loss method is used to take account of changes in soil moisture content with a single soil layer. Since the study is based on the field soil moisture measurements with the Time Domain Reflectometer (TDR), depth of soil layer is taken as the length of TDR probes; 160 mm. Due to lack of temperature and evaporation measurements within the Kurukavak basin, this method could not be integrated with an evapotranspiration method. The required parameters of the method are (HEC, 2008):

Maximum Deficit: specifies the maximum water storage capacity of the soil layer in units of depth. From previous studies (Tombul et. al., 2008) in the study area, average porosity of the soils is measured as 47.7 %. As a result, the maximum water storage capacity of the soil layer is computed by multiplying the depth of soil layer with the soil porosity (Equation 7.1). This value is assumed to be constant throughout the basin and used in three of the model simulations.

$$\text{MaxDef} = 0.477 \times 160 = 76.32 \text{ mm} \quad (7.1)$$

Initial Deficit: represents the initial soil moisture condition of the basin. It is the total depth of water which is required for a grid cell to reach the maximum deficit value. In other words, initial deficit indicates the difference between the maximum storage capacity and the available moisture content of a grid cell. Initial Deficit is calculated using the available/calculated volumetric moisture content of the soil and the previously computed maximum deficit with Equation 7.2.

$$\text{IniDef} = \text{MaxDef} - (m_v \times 160) \quad (7.2)$$

where m_v is the volumetric soil moisture content of the grid cell ($\text{m}^3 \text{m}^{-3}$)

Initial Deficit is the only model parameter which varies among the three model simulations. For the *Distributed SAR* and *Distributed ASAR* simulations, it is evaluated from the volumetric soil moisture grids of the Kurukavak basin for 07-

May-2005 (Figures B.5 and B.6). After resampling these grids to 50 m ground resolution, initial deficit value of each grid cell is calculated by using Equation 7.2. On the other hand, average value of TDR based soil moisture measurements at the 07-May-2005 dated field study is $0.2612 \text{ m}^3 \text{ m}^{-3}$, which gives an initial deficit value of 34.53 mm with Equation 7.3. This value is assumed to be constant for all grid cells for the *Lumped* event simulation.

$$\text{Lumped (IniDef)} = 76.32 - (0.2612 \times 160) = 34.53 \text{ mm} \quad (7.3)$$

Constant Rate: is the rate of infiltration of soil layer when it is fully saturated. As expected, it is a significant parameter for separation of the excess precipitation. From previous field sampling studies (Tombul et. al., 2008) held within the Kurukavak basin, saturated hydraulic conductivity of the basin soils range from 9 mm/h to 11 mm/h. In calibration of the model, this parameter is estimated as 8 mm/h.

Impervious: represents the percentage of the grid cell which has no contribution to the groundwater. In calibration of the model this parameter is estimated as 2 %.

Recession Baseflow:

The recession baseflow method is used to approximate the typical behavior of a watershed when channel flow recedes exponentially after a flood event (HEC, 2008). It defines the relationship of baseflow (Q) at time t with the initial baseflow at time t_0 (Q_0) as an exponential recession (Equation 7.4) (HEC, 2000).

$$Q = Q_0 k^t \quad (7.4)$$

where k is the exponential baseflow decay constant.

Figure 7.1 illustrates the computed baseflow with this method during a flood event, where the shaded region represents the exponential decay of baseflow from the start of flow. After the peak of direct runoff, a user defined threshold value is

described to indicate the start of the baseflow recession (Figure 7.2). The required parameters of the baseflow recession method are (HEC, 2008):

Initial Discharge: is the amount of baseflow at the beginning of the simulation, which is selected as the observed initial discharge at the basin outlet on 07-May-2005 at 10:00 (0.0016 m³/s).

Recession Constant: represents the rate of baseflow recession between storm events. It is defined as the ratio of baseflow at the current time to the baseflow one day earlier. In calibration of the model this parameter is estimated as 0.001.

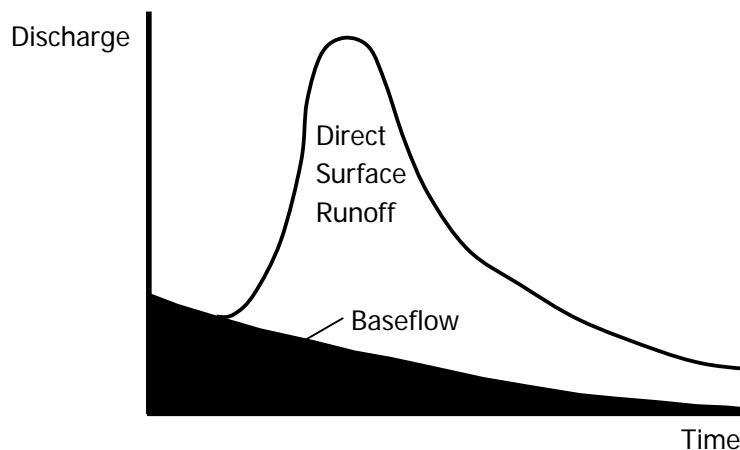


Figure 7.1. Illustration of exponential baseflow recession (HEC, 2000)

Ratio to Peak: defines the ratio of current flow to the peak flow and it is utilized during the falling limb of the hydrograph. The baseflow is reset when the current flow divided by the peak flow falls below this value. In calibration of the model this parameter is estimated as 0.4.

ModClark Transformation:

The ModClark method is a linear semi-distributed transform method which is based on the conceptual Clark unit hydrograph (UH) method (HEC, 2008). In Clark model,

UH of the basin is derived by using two important processes in the transformation of excess precipitation to runoff (HEC, 2000):

Translation: is the movement of excess water from its source to the watershed outlet,

Attenuation: is the reduction of magnitude of the discharge as the excess water is stored throughout the basin.

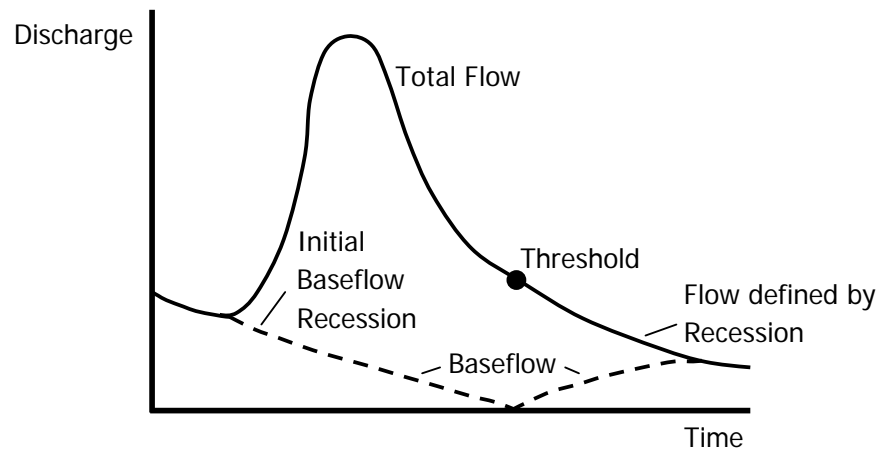


Figure 7.2. Illustration of baseflow recession after peak (HEC, 2000)

The Clark method uses a time-area curve and time of concentration to develop a translation hydrograph. On the other hand, after representing the basin as a collection of grid cells, the ModClark method eliminates the time-area curve and instead it uses a separate travel-time index for each grid cell.

This is achieved by calculating the travel distance of each cell to the watershed outlet. In the grid representation of the topography, each grid cell has 8 neighboring cells, and depending on the slope, surface flow originating in the center cell would flow to one of its 8 neighbors. Figure 7.3 illustrates a hypothetical basin which has a 3 by 3 grid cell representation. Direction of surface flow from each cell to one of its neighboring cells is shown with arrows.

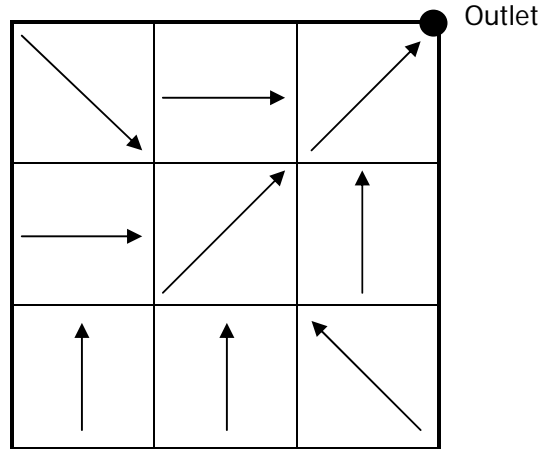


Figure 7.3. Schematic representation of flow direction

After determining the direction of flow of all grid cells, the *flow travel length* of each cell is calculated by tracing the flow from cell to cell; from the center of the originating cell to the outlet. For the most upstream cell of the hypothetical basin given in Figure 7.3, this process is also described schematically in Figure 7.4, in which cell size of the hypothetical basin is assumed as 10 m.

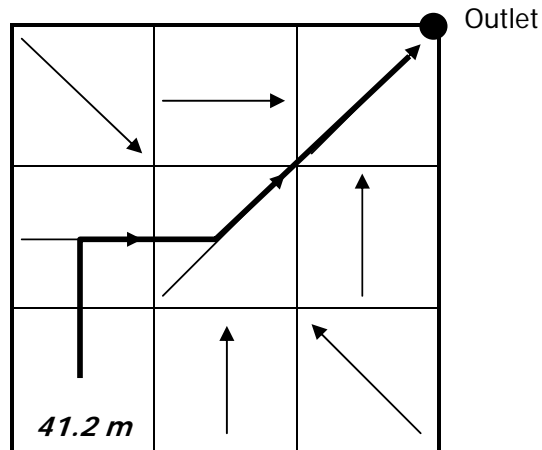


Figure 7.4. Schematic computation of flow travel length for 10 m cell size

Then, the flow travel length of each cell is scaled by the overall time of concentration to obtain travel-time index of each grid cell (Equation 7.5) (HEC, 2000).

$$t_{cell} = t_c \frac{d_{cell}}{d_{max}} \quad (7.5)$$

where;

t_{cell} is the travel time of the cell,

t_c is the time of concentration of the basin,

d_{cell} is the travel distance of flow from the cell to the outlet,

d_{max} is the travel distance of flow from the farthest cell to the outlet.

In the ModClark transformation method, the volume of inflow from each grid cell to the linear reservoir is computed as the product of cell area and excess precipitation calculated at that cell. The computed inflows are first lagged by the scaled travel-time index and then routed through a linear reservoir which yields an outflow hydrograph for that cell. HMS combines these cell outflow hydrographs to calculate the direct runoff hydrograph of the watershed (HEC, 2000; HEC, 2008). The required parameters of the ModClark transformation method are:

Time of Concentration: is the travel time required for the flow that is originating from the farthest point on the basin boundary, to reach to the outlet. The grid cell in the basin which has the largest flow travel length value will have exactly this specified time of concentration value as its travel-time index. In order to estimate the time of concentration value of a watershed, a number of empirical equations, utilizing morphological basin parameters, are available in the literature (ASCE, 1996). The time of concentration of the Kurukavak basin is calculated by using Kirpich and Bransby Williams equations; 0.4 and 1.2 hours respectively. In calibration of the model, this parameter is estimated as 0.5 hours.

Storage Coefficient: is used in the linear reservoir routing process of ModClark method and the same value is given to all grid cells. In calibration of the model this parameter is estimated as 1.2 hours.

Initial Abstraction Loss:

Initial abstraction represents the amount of water which is held by interception and depression storages and overland flow starts after it is satisfied. Even if the HMS model does not have a specified parameter for defining initial abstraction, it is included in the calibration part by extracting a certain depth of water from the recorded precipitation data prior to the start of surface runoff. In calibration of the model initial abstraction is estimated for this event as 43.9 mm.

Gridded Precipitation:

The gridded precipitation method is one of the meteorological models available in HMS. It is specifically designed to work with the ModClark transformation and preferably to be used with a radar-based precipitation data (HEC, 2008). Since radar rainfall data is not available for the study catchment, the rainfall data collected by the station at the basin outlet is the only precipitation gage utilized in this study. Hence, the observed precipitation in this gage is assumed to be distributed uniformly to all grid cells within the basin. As a result, a separate precipitation grid, covering the whole basin, is prepared for each time step (5 min) of the model and used as the rainfall input to the HMS.

Discharge Gage:

The Kurukavak basin, covering an area of 4.73 km², is considered as a small catchment and it is not further divided into smaller subbasins. Consequently, the catchment is modeled with two physical components: the basin and the outlet. The observed flow data at the basin outlet are input to the HMS model as a discharge gage and it is used to compare with the simulation outflows.

7.2. Simulation Results

As previously mentioned, three different model simulations of the 1-Jun-2005 flood event are carried out with HEC-HMS. Among the model parameters detailed in the

previous section, *Initial Deficit* is the only parameter that differs among the simulations. A summary of model parameters used in the HMS event simulations is presented in Table 7.1. In addition, numerical values such as peak flow, time of peak flow, total flow etc. which are representing the computed flow hydrographs are tabulated in Table 7.2. The percent change between the total flows and peak flows of the observed and simulated hydrographs are also calculated (Table 7.2). Moreover, the root mean square error (RMSE) between the computed and observed flow values is calculated using Equation 7.6. Lastly, graphical outputs of the simulations are presented in Figures 7.5, 7.6 and 7.7.

$$RMSE = \sqrt{\frac{\sum(Q_{observed} - Q_{computed})^2}{n-1}} \quad (7.6)$$

where;

$Q_{observed}$ is the observed discharge at time t

$Q_{computed}$ is the computed discharge at time t

n is the total number of discharge observations

After obtaining the simulation results, a graphical comparison between the computed and observed flood hydrographs is done. Since the *Distributed SAR* simulation parameters are obtained through calibration, the computed flood hydrograph with this simulation clearly represents the shape of the observed one (Figure 7.6). Moreover, the *Distributed ASAR* simulation output (Figure 7.7) is almost identical to the one calculated with the *Distributed SAR* simulation, and hence close to the observed flood hydrograph.

Then, the third model simulation, *Lumped*, is analyzed to differentiate the effects of using distributed and lumped initial soil moisture conditions. In the *Lumped* model simulation, since a constant initial soil moisture value is accepted for the whole basin, all basin cells reach to the maximum deficit value at the same time, and hence, overland flow on each cell starts at the same time, which results in a higher peak discharge value than the observed one (Figure 7.5).

Table 7.1. Summary of the parameters used in the model simulations

		Model Simulations		
		Distributed SAR	Distributed ASAR	Lumped
Deficit & Constant Loss	Initial Deficit (mm)	From 07-May-2005 SAR image: <i>Figure B.5</i>	From 07-May-2005 ASAR image: <i>Figure B.6</i>	Average TDR measurement on 07-May-2005: 34.53
	Maximum Deficit (mm)	76.32		
	Constant Loss (mm/h)	8		
	Impervious (%)	2		
Baseflow	Initial Discharge (m ³ /s)	0.0016		
	Recession Constant	0.001		
	Ratio to Peak	0.4		
ModClark	Time of Concentration (h)	0.5		
	Storage Coefficient (h)	1.2		
Initial Abstraction (mm)		43.9		
Precipitation		Gridded precipitation from the observed rainfall data at the basin outlet		
Discharge		Observed flow at the catchment outlet		

This physical process is more significant in the computed excess precipitation values and can be easily observed by comparing the simulation hyetographs of 01-Jun-2005 event (Figures 7.5, 7.6 and 7.7). For the *Lumped* simulation case, a sudden drop in the infiltration rate is computed which is then continued as a constant infiltration rate at 8 mm/h (Figure 7.5). On the other hand, the *Distributed SAR* and *Distributed ASAR* simulation outputs indicate a more accurate (close to nature)

infiltration process. From Figures 7.6 and 7.7, behavior of an exponential decay function is observed for the infiltration rate, which asymptotically approaches to the constant value of 8 mm/h after the flood peak.

Table 7.2. Comparison of simulation results with the observed values

	Observed	Model Simulations		
		Lumped	Distributed SAR	Distributed ASAR
Peak Discharge (m³/s)	9.97	10.89	9.77	9.90
Time of Peak	1-Jun-2005 07:20	1-Jun-2005 07:20	1-Jun-2005 07:20	1-Jun-2005 07:20
Total Flow (x 1000 m³)	118.10	118.29	109.23	109.89
% Difference in Peak Flows		9.2	2.0	0.7
% Difference in Total Flows		0.2	7.5	7.0
RMSE (Equation 7.5)		0.430	<i>0.351</i>	0.349
Figure Number		7.5	7.6	7.7

Lastly, the computed RMSE (Equation 7.6), between the observed and simulated discharge values of the Distributed and Lumped model simulations are compared. The RMSE value of the Distributed SAR and Distributed ASAR simulations are both calculated as 0.35. On the other hand, the same value is computed as 0.43 for the Lumped model simulation.

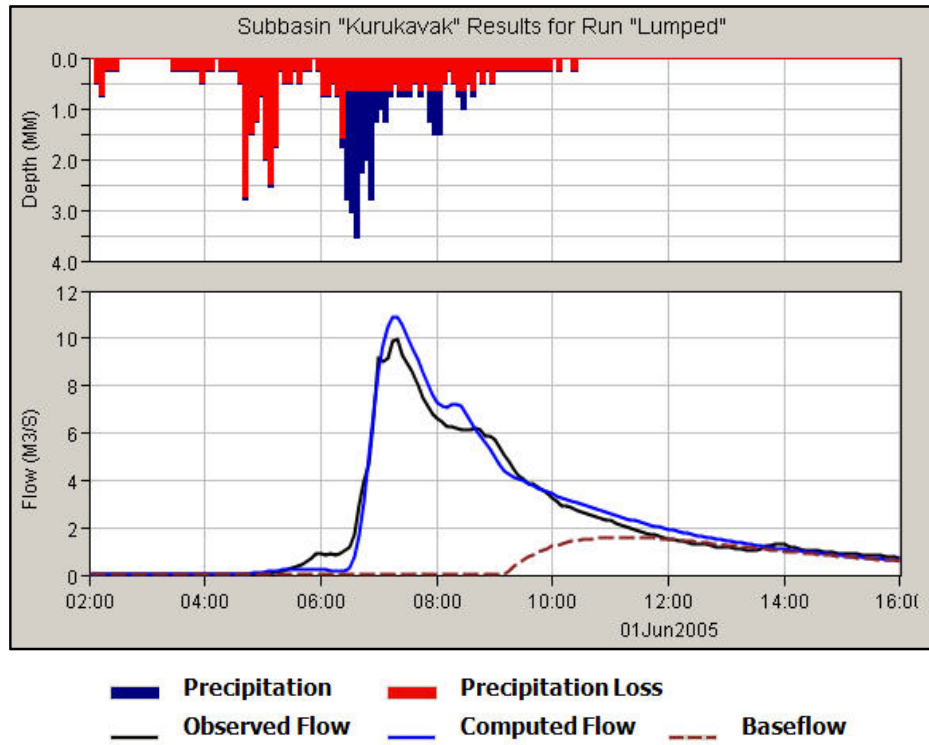


Figure 7.5. Results of the *Lumped* model simulation

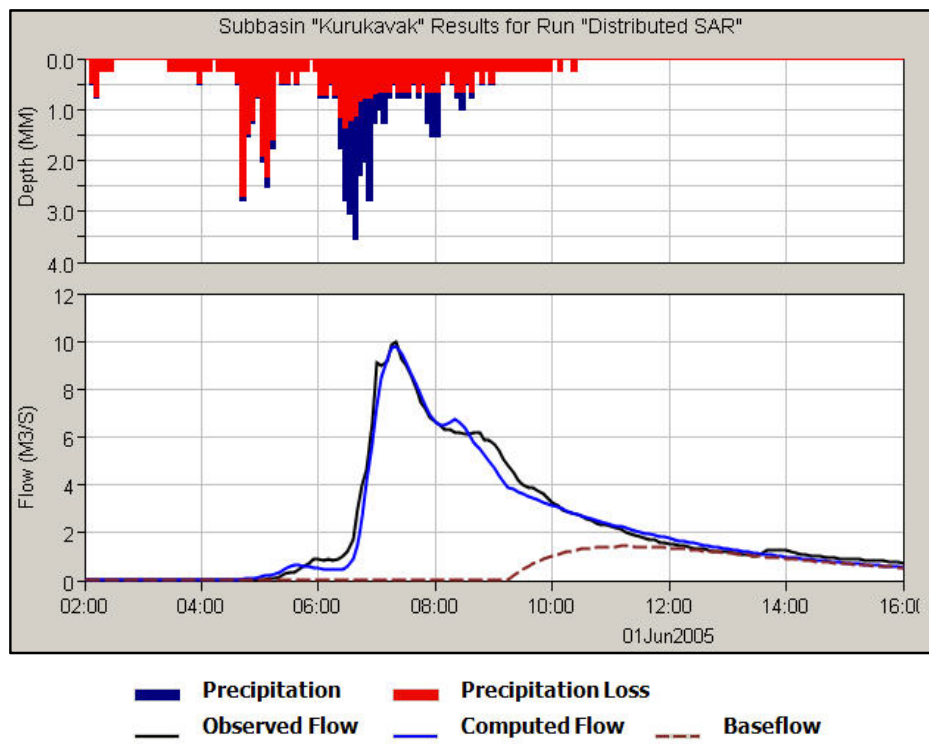


Figure 7.6. Results of the *Distributed SAR* model simulation

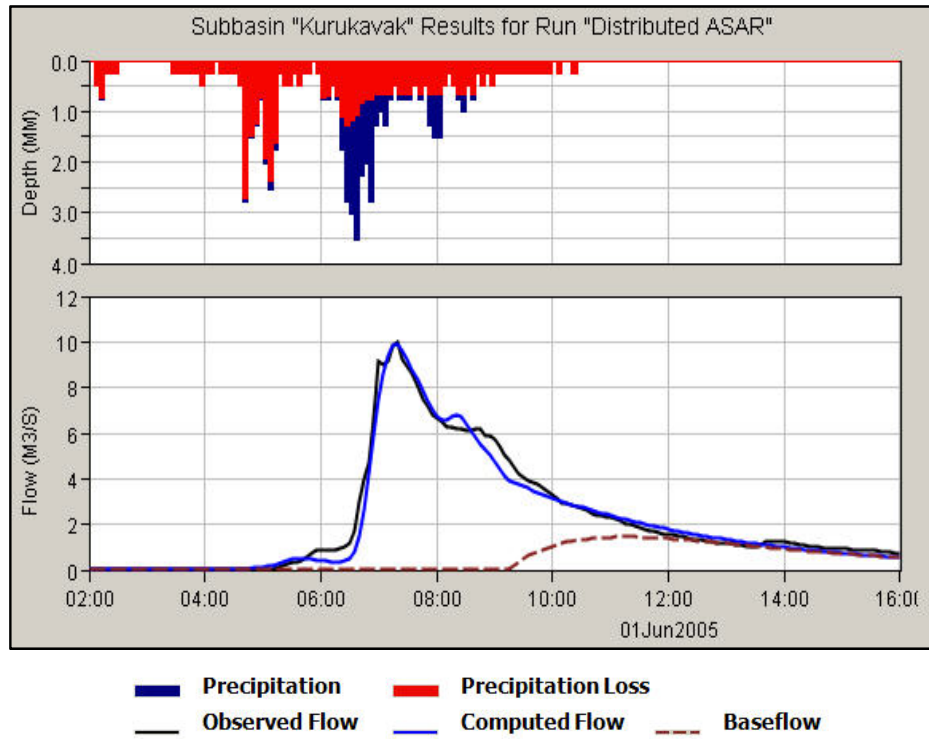


Figure 7.7. Results of the *Distributed ASAR* model simulation

CHAPTER 8

DISCUSSION OF RESULTS

Field measurement of soil moisture is limited to point records. On the other hand, with the development of new sensors and algorithms, remote sensing is a promising field of study for obtaining surface soil moisture at watershed and regional scales. In this research, outcomes of a case study on microwave remote sensing of surface soil moisture are presented. Extracting the soil moisture distribution of the study catchment from active microwave data, and then implementing these results with a semi-distributed hydrological model are the major accomplishments of this study. This chapter covers the detailed discussion regarding all aspects of this work.

The ***Study Basin*** is a micro catchment, which is located in the western Anatolia with an area of 4.73 km². Due to its small size, the Kurukavak watershed is very suitable for a pioneering study on microwave remote sensing of soil moisture in Turkey. On the other hand, among the three land use types of the basin, densely forested areas are not suitable for derivation of soil moisture – radar backscatter relationship. As a result, a method independent of radar imagery is developed for soil moisture estimation within these areas.

Point Soil Moisture Data Collection is achieved with a Time Domain Reflectometer (*TDR*). Field data collection is carried out on farmland and pasture land use classes of the basin; with 68 points within 9 plots for 9 field study dates of 2004-2005 water year. In selection of point locations, it is aimed to measure soil moisture on a wide range of values. In addition to land use, these locations are selected with a consideration in topography, and especially according to topographic index values of the points. It is observed from the collected moisture data that

farmland areas indicate a relatively better uniformity in moisture values than the pasture fields (Table 3.3). At the beginning of the study, Plot 10, which has a pasture land use class, has been selected on a remote part of the basin. Different from the other three pasture plots (P5, P8 and P9), P10 is located on a higher altitude with points having lower topographic index values. Unfortunately, due to its remote location, among the nine field studies, soil moisture data are collected only on 09-Oct-2004 for P10. As a result, the points within pasture fields have a higher mean topographic index value; 9.0, than that of farmland points; 6.5.

SAR/ASAR Images of the Kurukavak basin are the source of active microwave data. The acquired images have a fine ground resolution of 12.5 m, which is very appropriate considering the small size of the study catchment. On the other hand, ERS-2 and ENVISAT satellites have a high temporal resolution of 35 days, which makes it inadequate for investigating the seasonal variations in surface soil moisture.

Implementing a Permanent Raster Data Model; with a constant ground resolution, predefined cell locations and unique cell IDs, is the first successful accomplishment of the study. The only disadvantage of this method is the amount of error inserted in the datasets upon resampling of them to the constant cell size and location of the permanent raster model. On the other hand, using such a well defined geo-database is the key part of integrating point soil moisture measurements with the gridded datasets; radar imagery, slope, topographic index etc., of the study.

Dubois Model is a semi-empirical backscatter model, which is utilized for inversion of soil surface roughness values. The model is selected primarily for its simplicity and requirement for single roughness parameter. In building soil moisture – backscatter relationship, soil roughness is one of the key parameters. Since no field measurement of the soil roughness is carried out during field studies, inversion of the Dubois model is utilized to estimate the roughness values for the point soil moisture measurement locations. About 68 % of these values are found within the limits of both the Dubois model and the proposed threshold, and hence used to

derive soil roughness – radar backscatter relationships. For SAR and ASAR datasets, two non-linear equations (Equations 5.6 and 5.7) are obtained with high correlation coefficients of 0.72 and 0.77, respectively. Moreover, implementation of these equations on the other bare soil or sparsely vegetated fields of the Kurukavak basin is carried out successfully for soil surface roughness mapping. The proposed methodology requires two radar images of the same area with the same polarization; both are VV. On the other hand, the applied method could be simplified by utilizing two radar images having different polarizations; HH and VV.

The ***Wet Soil Backscatter Relationship*** (Equation 6.1), representing radar backscatter as a function of soil moisture, incidence angle and surface roughness, is the most significant accomplishment of this research. Two non-linear equations (Equation 6.1 and 6.2) are derived for SAR and ASAR datasets with a very high correlation value of 0.93, and hence found to be successful. Moreover, this relationship is open for further research on different basins with other radar sensor types and properties.

The ***Dry Soil Backscatter Relationship*** is the hypothetical variation of the wet soil relationship with an assumption of dry soil condition; the radar backscatter is independent of soil moisture. Due to the dominating effect of soil roughness on radar backscatter, the derived equations (Equation 6.4 and 6.5) have good correlation values of 0.87 and 0.89 for SAR and ASAR datasets, respectively. Moreover, the dry soil backscatter relationship is the key component of the first (Backscatter Correction Factors) and second (Water Cloud Model) methods used for soil moisture estimation in this study.

Backscatter Correction Factors is the first method used for computation of surface soil moisture distribution on bare or sparsely vegetated areas of the study catchment. The corrected backscatter values are found to be well correlated (0.69 for SAR and 0.62 for ASAR) with the surface soil moisture measurements. Among the three soil moisture methods utilized in this study, it is the most successful one and can be easily implemented for basins having similar conditions.

Water Cloud Model (WCM), which is applied to the vegetated fields of the basin other than forested areas, is the second method of the study for surface soil moisture estimation. Ulaby et al. (1981b) remarks that the Water Cloud Model is not an exact or perfect model and it should be regarded as a general first-order model. Among the three soil moisture methods, the WCM outputs present the smallest correlation; 0.42 for SAR and 0.45 for ASAR datasets. On the other hand, the proposed delta index method, which is discussed in section 6.2, is a new approach to the cloud model, and it is certainly open to further development and research.

Basin Indexes is the third and final method of soil moisture computation. Since this approach is applied to the forested areas of the basin, it is the only method in which radar imagery is not utilized. The derived relationship (Equation 6.22) indicates a high correlation value (0.79) between the observed and computed moisture values. However, plot of these values (Figure 6.12) represents that this relation yields slightly higher moisture values for drier soil condition and slightly lower moisture values for wet soils. This can be also visualized from the computed frequency histograms of the soil moisture distributions (Figure C.1 to C.8) where higher than observed mean moisture values can be seen in the histograms of 20-Aug-2005 and 09-Oct-2004 both of which have dry soil conditions.

Soil Moisture Distributions of the Kurukavak watershed are calculated for 09-Oct-2004 (Figures B.1 and B.2), 18-Dec-2004 (Figures B.3 and B.4), 07-May-2005 (Figures B.5 and B.6) and 20-Aug-2005 (Figures B.7 and B.8) field study dates. A better understanding about the computed soil moisture values can be observed by comparing the **frequency histograms** of the computed soil moisture distributions and observed soil moisture values given in Appendix C.

- **09-Oct-2004**; it is observed from Figures C.1 and C.2 that both of the soil moisture estimation methods (Backscatter Correction and Basin Indexes) result in a similar pattern with the observed one. But it is also seen from the histograms that computed values are slightly higher than the observed ones. Moreover, average observed moisture is 16.5 %, whereas an average

moisture value around 20 % is computed from both of the models (Table C.1).

- **18-Dec-2004**; from Figures C.3 and C.4, a very similar pattern is seen for the computed and observed soil moisture distributions obtained from both of the methods (Backscatter Correction and Basin Indexes). The tabulated average moisture values (Table C.2) are around 20 % for both of the observed and computed moisture distributions.
- **07-May-2005**; is the only date where Water Cloud Model is used for soil moisture estimation. Even if the outcomes of the cloud model are not found as successful as the other two methods, frequency histograms of the computed and observed soil moisture distributions (Figures C.5 and C.6, and Table C.3) indicate a good similarity.
- **20-Aug-2005**; histograms of computed soil moisture distributions, with Backscatter Correction and Basin Indexes methods, do not indicate a similar pattern with the histogram of the observed values. In addition, since 20-Aug-2005 has the driest soil condition among the nine field studies, similar to 09-Oct-2004, both of the methods result in higher mean moisture values than the observed one (Figures C.7 and C.8, and Table C.4).
- **SAR/ASAR**; the frequency histograms of the computed soil moisture distributions from the SAR and ASAR datasets are almost identical for Backscatter Correction method. A significant difference in patterns is observed with the Water Cloud Model between Figures C.5 and C.6. Since the third methodology, the Basin Indexes, is independent of radar imagery no variations between the histograms of the SAR and ASAR images is expected.

HEC-HMS; is the semi-distributed hydrological model used for simulation of the 01-Jun-2005 flood event which is recorded at the outlet of the Kurukavak basin. For this purpose, three different simulations, with each one having different initial soil

moisture conditions, are carried out. For the *Distributed SAR* and *Distributed ASAR* simulations, the initial soil moisture condition is obtained from the soil moisture distributions of the 07-May-2005 field study date, from the SAR and ASAR images, respectively. On the other hand, for the *Lumped* simulation, the average TDR measurement observed at the field study on 07-May-2005 is assumed to be uniform over the entire catchment. Implementing the distributed soil moisture estimates of the study with a hydrological model is the last important accomplishment of this thesis.

- ***Distributed SAR & Distributed ASAR***; simulations output almost identical flood hydrographs which are also very close to the observed hydrograph in shape, peak discharge and total volume of flood (Figures 7.6 and 7.7; Table 7.2). The computed root mean square error between the observed and simulated flow values, ordinate values of the hydrographs, is 0.35 for both of the simulations.
- ***Lumped***; simulation results in a higher peak than the observed one, with a computed root mean square error value of 0.43 between the observed and simulated discharge values. The major difference between the Lumped and Distributed simulations is observed from the computed precipitation losses with the model; a sudden drop continued with a constant rate of infiltration is observed for the Lumped case in Figure 7.5. On the other hand, even if a constant value is defined for the model, an exponential decay in the infiltration rate, which is close to the actual behavior, is observed for the distributed cases in Figures 7.6 and 7.7.

The main aim of the hydrological model simulations is to perform a semi-distributed analysis with a distributed soil moisture input. Due to the lack of hydrological data for the study watershed, the model runs are carried out with the minimum number of model components. But the outcomes of integrating distributed soil moisture with a hydrological model are very promising and it should be further investigated with more model components and/or by other hydrological models.

CHAPTER 9

RECOMMENDATIONS AND CONCLUSIONS

9.1. Recommendations

This thesis work covers a case study on microwave remote sensing of soil moisture. Both of the applied techniques and the developed relationships within the scope of this work are open to further discussion and development. A list of recommendations for future studies sharing similar research objectives is given below.

- The study basin is a small catchment and hence it is very suitable for a case study application. For future studies it is recommended to implement and investigate the proposed techniques of this research on basins larger in size.
- A major problem in radar remote sensing of soil moisture within the Kurukavak basin is the densely forested areas, which constitute about half of the basin area. A better understanding about the Backscatter Correction and the Water Cloud Model soil moisture estimation methods would be obtained with the application of these techniques on a watershed without dense vegetation cover.
- Prior to the field studies, the point soil moisture measurement locations are selected at the office with a consideration in a number of topographic parameters. Since unexpected problems could be faced during field studies, it is also recommended that alternative locations should be selected as well.

- Even if the TDR is a powerful and easy to operate instrument, the total number of point measurements that can be obtained at a single field study depends on the field conditions and the operator. Moreover, it is also observed during field data collection that surface soil moisture varies considerably within a day depending on the weather conditions. Consequently, installation of permanent soil moisture sensors within the study area to continuously collect soil moisture data should also be considered.
- The temporal resolution of the acquired active microwave images, 35 day cycles of the satellites, is not suitable for time series analysis of soil moisture. But these sensors have the fine resolution to carry out analysis for watershed scale applications. For basins larger in size, coarse resolution scatterometer data with smaller repeat cycles could also be integrated with fine resolution active microwave data.
- Due to its ease of use and flexibility, implementation of a permanent raster data model could be used on various remote sensing applications where ground measurements are to be integrated with raster data sets of different resolutions.
- The Dubois model includes two relationships, for VV and HH polarized images separately. Since all radar imagery utilized in this study are VV polarized; only one of the two model equations can be implemented with an inversion and comparison algorithm. On the other hand, roughness parameter can be extracted directly with both of the equations by using two radar images of the same area with different polarizations.
- The computed radar backscatter – soil surface roughness relationships can be further used for similar basins where no field roughness measurements are accomplished. Unfortunately, accuracy of the derived relationships cannot be validated with field measurements. The validation of computed

roughness values with ground measurements is also recommended as a future work.

- The *wet soil backscatter relationship* and the Backscatter Correction Factors method are the most promising outcomes of this research and they should be further tested on different fields and under other sensor types. In addition, the delta index approach used with the Water Cloud Model has a considerable potential for remote sensing of soil moisture on vegetated areas.
- The HEC-HMS model, which is used for the simulation of 1-June-2005 flood event, has the advantages of public availability and capability of performing distributed analyses. But the distributed components of the model are designed to work within the continental United States and hence it is not easy to implement basins outside North America. As a result, the semi-distributed event analysis could be carried out with other rainfall – runoff models having similar capabilities.
- As detailed in the Chapter 7 of the study, the flood event simulations are performed with the minimum number of model components that is required to run the HMS model. A major recommendation at this point should be utilization of other model components which could increase the accuracy of model outcomes. In addition to including an evapotranspiration component, such as *Gridded Priestley Taylor*, using a different soil model, which represents the soil in more than one layer like *Gridded Soil Moisture Accounting* method, is recommended for future studies.
- Since precipitation data from a single rain gage are only available, uniform distribution of the precipitation is assumed throughout the entire catchment. A better representation of the flood event can be obtained with records from more than one rainfall measurement station.

9.2. Conclusions

Soil moisture is an important variable that controls various land surface processes and it is essential to weather forecasting, climate modeling and flood simulation. In spite of its importance to several disciplines, soil moisture information is not widely available on watershed and regional scales. Consequently, development of better estimation techniques for soil moisture, especially with the integration of remote sensing imagery, is a challenging but promising field of study.

The main objective of this study is to retrieve soil moisture information from active microwave remote sensing which is achieved through development and application of a number of relationships and techniques as outlined in Chapter 1 of the thesis. In this respect, a micro catchment in western Anatolia is selected as a case study, and a number of field studies are carried out for collection of point soil moisture data. In addition, active microwave images of the basin for these dates are also acquired from European Space Agency (ESA).

First objective of the study is to develop a methodology for soil roughness mapping of the study basin, which is achieved with the inversion of the Dubois backscatter model. Despite the fact that the method is successfully applied to the bare or sparsely vegetated surfaces of the basin, it has limitations from both the Dubois model and initial assumption of the applied technique. As a result, surfaces from smooth to medium level of roughness can only be extracted from remote sensing data.

The second objective of the study is to propose an algorithm for reliable estimation of soil moisture from radar imagery on bare or sparsely vegetated surface conditions. In this respect, the wet soil backscatter relationship is developed and further used within the soil moisture estimation methods. A variation of this relationship is utilized within the Backscatter Correction Factors method, which is the first method used for producing soil moisture maps of the study catchment. Both of the developed backscatter relationships and the applied method are found very promising that they could be easily implemented for future studies.

Extracting soil moisture distribution of the study basin under dense vegetation cover condition is the third objective of the study. It is accomplished with an implementation of delta index algorithm with the Water Cloud Model, which is also the second method used for soil moisture mapping of the Kurukavak catchment. Even if the outcomes of this technique are found to be relatively successful, it has certain drawbacks due to the limitations of the Water Cloud Model in describing the complexity of the actual physical condition.

Basin Indexes is the third method used for soil moisture mapping of the Kurukavak basin. Topographic and solar radiation indexes are utilized to build a linear relationship between these watershed indexes and point soil moisture measurements. This relationship is then applied to the forest land use class of the catchment, where microwave remote sensing of soil parameters is not possible. A major question in this method is the applicability of the soil moisture measurement locations, which are not selected within forested areas of the basin. Since the method is solely developed on terrain indexes, the relationship is independent of land use conditions. On the other hand, it should be noted that this method has a general tendency to overestimate dry soil condition and underestimate the wet soil condition.

Finally, soil moisture maps of the Kurukavak basin are produced with the three methods; Backscatter Correction Factors method is applied for bare or sparsely vegetated, Water Cloud Model is used for densely vegetated and Basin Indexes method is applied for forested land use conditions of the watershed.

In the last part of the study, the computed soil moisture distribution maps are input to a semi-distributed hydrological model as an initial soil moisture condition of a flood event simulation. In order to investigate the contribution of distributed initial soil moisture data on hydrological model outputs, simulation of the same event is also performed with the lumped initial moisture condition. A major difference in the decay of computed infiltration rates is observed between these conditions. Even if a constant value is defined for the model, an exponential decay in the infiltration rate, which is similar to the actual behavior, is observed for the distributed condition.

REFERENCES

ASCE, 1996, Hydrology Handbook, 2nd Edition, American Society of Civil Engineers, New York, USA

Attema, E.P.W., Ulaby, F.T., 1978, Vegetation Modeled as a Water Cloud, Radio Science, 19, pp. 357 – 364

Baghdadi, N., Gaultie S., King, C., 2002a, Retrieving Surface Roughness And Soil Moisture from Synthetic Aperture Radar (SAR) Data Using Neural Networks, Canadian Journal of Remote Sensing, 28, pp. 701 – 711

Baghdadi, N., King, C., Chanzy, A., Wingneron, J.P., 2002b, An empirical calibration of IEM model based on SAR data and measurements of soil moisture and surface roughness over bare soils, International Journal of Remote Sensing, 23, pp. 4325 – 4340

Baghdadi, N., King, C., Bourguignon, A., Remond, A., 2002c, Potential of ERS and Radarsat data for surface roughness monitoring over bare agricultural fields: application to catchments in Northern France, International Journal of Remote Sensing, 23, 17, pp. 3427-3442

Baghdadi, N., Zribi, M., 2006, Evaluation of Radar Backscatter Models IEM, OH, Dubois Using Experimental Observations, International Journal of Remote Sensing, 27, 18, pp. 3831 – 3852

Beven, K.J., Kirkby, M.J., 1979, A Physically Based Variable Contributing Area Model of Basin Hydrology, Hydrology Science Bulletin, 24, 1, pp. 43 - 69

Bindlish, R., Barros, A.P., 2000, Multifrequency soil moisture inversion from SAR measurements with the use of IEM, Remote Sensing of Environment, 71, pp. 67-88

Bindlish, R., Barros, A.P., 2001, Parameterization of Vegetation Backscatter in Radar-Based Soil Moisture Estimation, Remote Sensing of Environment, 76, pp. 130 – 137

Ceballos, A., Scipal, K., Wagner, W., Martinez-Fernandez, J., 2005, Validation of ERS scatterometer-derived soil moisture data in the central part of the Duero Basin, Spain, Hydrological Processes, 19

Chauhan, N., Le Vine, D., Lang, R., 1999, Passive and active microwave remote sensing of soil moisture under a forest canopy, In Proceedings of the International Geoscience and Remote Sensing Symposium, IGARSS '99, 28 June – 2 July 1999, Hamburg, Germany. IEEE, Piscataway, N.J., pp. 1914 – 1916.

Chen, K.S., Yen, S.K., Huang, W.P., 1995, A simple model for retrieving bare soil moisture from radar scattering coefficients, *Remote Sensing of Environment*, 54, pp. 121 – 126

Du, Y., Ulaby, F.T., Dobson, M.C., 2000, Sensitivity to Soil Moisture by Active and Passive Microwave Sensors, *IEEE Transactions on Geoscience and Remote Sensing*, 38, pp. 105–114

Dingman, S.L., 2002, *Physical Hydrology: 4th Edition*, Prentice Hall, New Jersey, USA

Dubois, P., Van Zyl, J., Engman, T., 1995, Measuring soil moisture with imaging radars. *IEEE Transactions on Geoscience and Remote Sensing*, 33, 4, pp. 915 – 926

Engman, E.T., Chauhan, N., 1995, Status of Microwave Measurements with Remote Sensing, *Remote Sensing of Environment*, 51

ESA, 1998, *ENVISAT: ASAR Science and Applications*, Technical Document SP-1225, European Space Agency

Friedl, M.A., Davis, F.W., 1994, Sources of variation in radiometric surface temperature over a tallgrass prairie, *Remote Sensing of Environment*, 48

Fung, A.K., Li, Z., Chen, K.S., 1992, Backscattering from a randomly rough dielectric surface, *IEEE Transactions on Geoscience and Remote Sensing*, 30, pp. 356 – 369

Goyal, S.K., Seyfried, M.S., O'Neill, P.E., 1999, Correction of surface roughness and topographic effects on airborne SAR in mountainous rangeland areas, *Remote Sensing of Environment*, 67, pp. 124 - 136

Haider, S.S., Said, S., Kothiyari, U.C., Arora, M.K., 2004, Soil Moisture Estimation using ERS 2 SAR Data: A Case Study in the Solani River Catchment, *Hydrological Sciences*, 49, 2, pp. 323 – 334

HEC, 2000, *HEC-HMS: Technical Reference Manual*, US Army Corps of Engineers Hydrologic Engineering Center, Davis CA, USA

HEC, 2008, *HEC-HMS version 3.2: User's Manual*, US Army Corps of Engineers Hydrologic Engineering Center, Davis, CA, USA

Henderson, F.M., Lewis, A.J., 1998, *Manual of Remote Sensing Volume II: Principles and Applications of Imaging Radar*, 3rd Edition, John Wiley, Hoboken, NJ, USA

- Jackson, T.J., Le Vine, D.M., Hsu, H.Y., Oldak, A., Starks, P.J., Swift, C.T., Isham, J.D., Haken, M., 1999, Soil Moisture Mapping at Regional Scales Using Microwave Radiometry: The Southern Great Plains Hydrology Experiment, *IEEE Transactions on Geoscience and Remote Sensing*, 37, 5, pp. 2136 - 2151
- Laur, H., Bally, P., Meadows, P., Sanchez, J., Schaettler, B., Lopinto, E., Esteban, D., 2004, Derivation of the Backscatter Coefficient in ESA ERS SAR Products, European Space Agency, Technical Note ES-TN-RS-PM-HL09, Issue 2, Rev. 5f
- Leconte, R., Brissette, F., Galarneau, M., Rousselle, J., 2004, Mapping Near-Surface Soil Moisture with RADARSAT-1 Synthetic Aperture Radar Data, *Water Resources Research*, 40
- Lillesand, T.M., Kiefer, R.W., 1999, *Remote Sensing and Image Interpretation*, John Wiley & Sons, New York
- Moran, M.S., Vidal, A., Troufleau, D., Inoue, Y., Qi, J., Clarke, T.R., Pinter, P.J. Jr., Mitchell, T., Neale, C.M.U., 1997, Combining Multi-Frequency Microwave and Optical Data for Farm Management, *Remote Sensing of Environment*, 61, pp. 96 – 109
- Moran, M.S., Vidal, A., Troufleau, D., Inoue, Y., Mitchell, T. A., 1998, Ku and C Band SAR for Discriminating Agricultural Crop and Soil Conditions, *IEEE Transactions on Geoscience and Remote Sensing*, 36, 1, pp. 265 - 272
- Moran, M.S., Hymer, D.C., Qi, J., Sano, E.E., 2000, Soil Moisture Evaluation Using Multi Temporal Synthetic Aperture Radar In Semiarid Rangeland, *Agricultural and Forest Meteorology*, 105, pp. 69–80
- Moran, S.M., Peters-Lidard, C.D., Watts, J.M., McElroy, S., 2004, Estimating Soil Moisture at the Watershed Scale with Satellite-Based Radar and Land Surface Models, *Canadian Journal of Remote Sensing*, 30, 5
- Moore, I.D., Norton, T.W., Williams, J.E., 1993, Modelling Environmental Heterogeneity in Forested Landscapes, *Journal of Hydrology*, 150, pp. 717 - 747
- Neusch, T., Sties, M., 1999, Application Oof Dubois-Model Using Experimental Synthetic Aperture Radar Data for the Determination of Soil Moisture and Surface Roughness, *ISPRS Journal of Photogrametry and Remote Sensing*, 54, pp. 273 – 278
- Noborio, K., 2001, Measurement of Soil Water Content and Electrical Conductivity by Time Domain Reflectometry: A Review, *Computers and Electronics in Agriculture*, 31, pp. 213 – 237
- Oh, Y., Sarabandi, K., Ulaby, F.T., 1992, An Empirical Model and an Inversion Technique for Radar Scattering from Bare Soil Surfaces, *IEEE Transactions on Geoscience and Remote Sensing*, 30, pp. 370 – 382

Quensay, A., Le Hegarat-Masclé, S., Taconet, O., Vidal-Madjar, D., Wigneron, J.P., Loumagne, C., Normand, M., 2000, Estimation of Watershed Soil Moisture Index from ERS/SAR Data, *Remote Sensing of Environment*, 72, pp. 290 – 303

Rahman, M.M., Moran, M.S., Thoma, D.P., Bryant, R., Holifield Collins, C.D., Jackson, T., Orr, B.J., Tischler, M., 2008, Mapping Surface Roughness and Soil Moisture using Multi-Angle Radar Imagery without Ancillary Data, *Remote Sensing of Environment*, 12, pp. 391 - 402

Rosich, B., Meadows, P., 2004, Absolute Calibration of ASAR Level 1 Products Generated with PF - ASAR, European Space Agency, Technical Note, ENVI-CLVL-EOPG-TN-03-0010, Issue 1, Rev. 5

Sabins, F.F.Jr., 1997, *Remote Sensing – Principles and Interpretations*, 3rd Edition, W. H. Freeman, New York

Sahebi, M.R., Angles, J., Bonn, F., 2002, A Comparison of Multi-Polarization and Multi-Angular Approaches for Estimating Bare Soil Surface Roughness from Spaceborne Radar Data, *Canadian Journal Of Remote Sensing*, 28, 5, pp. 641 – 662

Schneider, K., Oppelt, N., 1998, The Determination of Mesoscale Soil Moisture Patterns with ERS Data, In *Proceedings of the International Geoscience and Remote Sensing Symposium, IGARSS '98*, 6–10 July 1998, Seattle, Wash. IEEE, New York

Shi, J., Wang, J., Hsu, A.Y., O'Neill, P.E., Engman, E.T., 1997, Estimation of Bare Surface Soil Moisture and Surface Roughness Parameter Using L-Band SAR Image Data, *IEEE Transactions on Geoscience and Remote Sensing*, 35, pp. 1254 – 1266

Shoshany, M., Svoray, T., Curran, P.J., Foody, G.M., Perevolotsky, A., 2000, The Relationship Between ERS-2 SAR Backscatter and Soil Moisture: Generalization from a Humid to Semi-Arid Transect, *International Journal of Remote Sensing*, 21, pp. 2337 – 2343

Stein, M.L., 1999, *Interpolation of Spatial Data: Some Theory for Kriging*, Springer, New York

Su, Z., Troch, P.A., De Troch, F.P., 1997, Remote Sensing of Bare Soil Moisture Using EMAC/ESAR Data, *International Journal of Remote Sensing*, 18, 10, pp. 2105 – 2124

Thoma, D.P., Moran, M.S., Bryant, R., Rahman, M., Holifield-Collins, C.D., 2006, Comparison of Four Models to Determine Surface Soil Moisture from C-Band Radar Imagery in a Sparsely Vegetated Semiarid Landscape, *Water Resources Research*, 42

Tombul, M., Şorman, A.Ü., Akyürek, Z., 2008, Hidrolojik Benzerlik Parametrelerinin Oluşturulmasında Kullanılmak Üzere Toprak Neminin ERS/SAR-ASAR Uydu Görüntülerinden Elde Edilmesi, TUBİTAK Research Project 104Y045, Eskişehir, Turkey

Topp, G.C., Davis, J.L., Annan, A.P., 1980, Electromagnetic Determination of Soil Water Content: Measurement in Coaxial Transmission Lines, *Water Resources Research*, 16, pp. 574 – 582

Ulaby, F.T., Batlivala, P.P., Dobson, M.C., 1978, Microwave Backscatter Dependence on Surface Roughness, Soil Moisture, and Soil Texture: I. Bare Soil, *IEEE Transactions Geosciences Remote Sensing*, 16, pp. 286 – 295

Ulaby, F.T., Moore, R.K., Fung, A.K., 1981a, *Microwave Remote Sensing Active and Passive, Volume I: Microwave Remote Sensing Fundamentals and Radiometry*, Artech House, Norwood, MA, USA

Ulaby, F.T., Moore, R.K., Fung, A.K., 1981b, *Microwave Remote Sensing Active and Passive, Volume II: Radar Remote Sensing and Surface Scattering and Emission Theory*, Norwood, MA, USA

Ulaby, F.T., Dubois, P. C., van Zyl, J., 1996, Radar Mapping of Surface Soil Moisture, *Journal of Hydrology*, 184, pp. 57 – 84

van Oevelen, P.J., Hoekman, D.H., 1999, Radar Backscatter Inversion Techniques for Estimation of Surface Soil Moisture: EFEDA-Spain and HAPEX-Sahel Case Studies, *IEEE Transactions on Geoscience and Remote Sensing*, 37, pp. 113 – 123

Verhoest, N.E.C., Hoeben, R., De Troch, F.P., Troch, P.A., 2000, Soil Moisture Inversion from ERS and SIR-C Imagery at the Zwalm Catchment, Belgium, In *Proceedings of the International Geoscience and Remote Sensing Symposium, IGARSS '00, 24–28 July 2000, Honolulu, Hawaii. IEEE, New York. pp. 2041–2043*

Wagner, W., Scipal, K., Pathe, C., Gerten, D., Lucht, W., Rudolf, B., 2003, Evaluation of the Agreement Between the First Global Remotely Sensed Soil Moisture Data with Model and Precipitation Data, *Journal of Geophysical Research*, 108

Western, A.W., Grayson, R.B., Blöschl, G., Willgoose, G.R., McMahon, T.A., 1999, Observed Spatial Organization of Soil Moisture and its Relation to Terrain Indices, *Water Resources Research*, 35, pp. 797 – 810

Western, A.W., Grayson, R.B., Blöschl, G., 2002, Scaling of Soil Moisture: A Hydrologic Perspective, *Annu. Rev. Earth Planet Sci.*, 30, pp. 149 - 180

Western, A.W., Zhou, S., Grayson, R.B., McMahon, T.A., Blöschl, G., Wilson, D.J., 2004, Spatial Correlation of Soil Moisture in Small Catchments and Its Relationship to Dominant Spatial Hydrological Processes, *Journal of Hydrology*, 286, pp. 113 - 134

Wickel, A.J., Jackson, T.J., Wood, E.F., 2001, Multitemporal Monitoring of Soil Moisture with RADARSAT SAR During the 1997 Southern Great Plains Hydrology Experiment, *International Journal of Remote Sensing*, 22, pp. 1571 – 1583.

Zribi, M., Dechambre, M., 2002, A New Empirical Model to Retrieve Soil Moisture and Roughness from C-Band Radar Data, *Remote Sensing of Environment*, 84, pp. 42 – 52

APPENDIX A

SOIL SURFACE ROUGHNESS MAPS

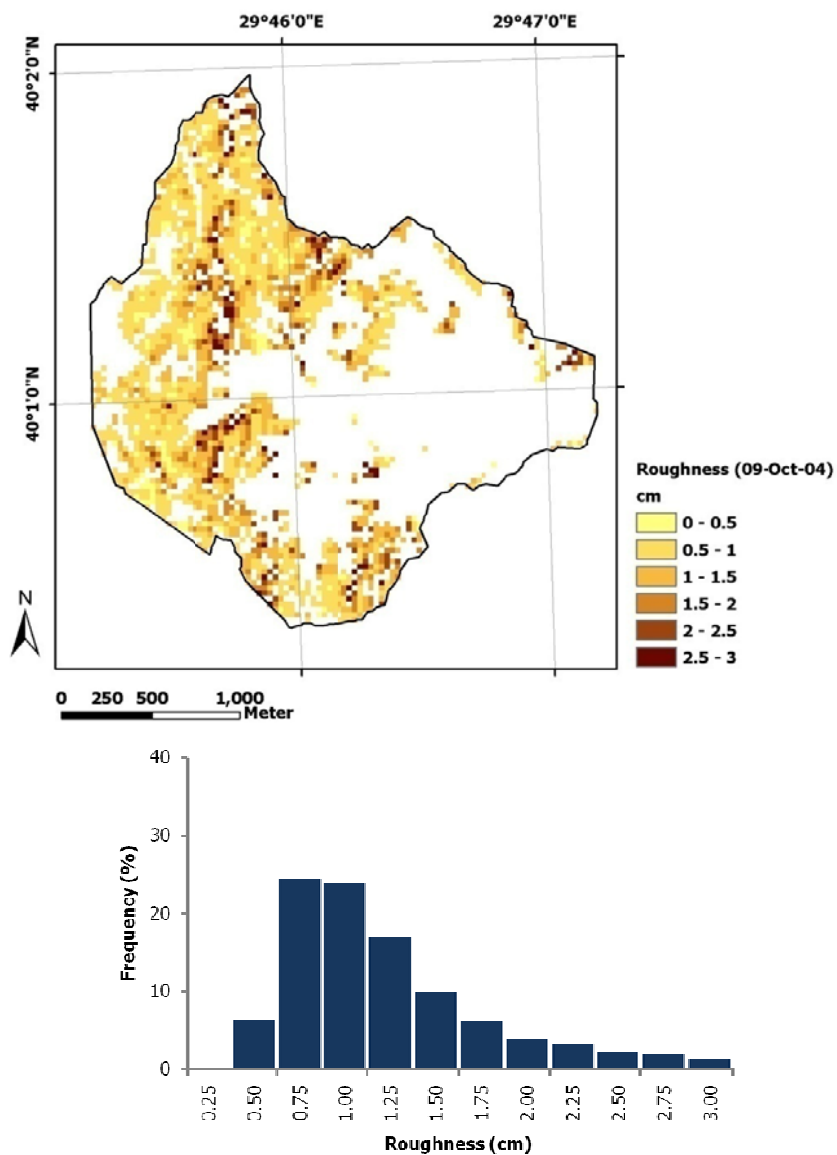


Figure A.1. Soil surface roughness map and histogram for 09-Oct-2004

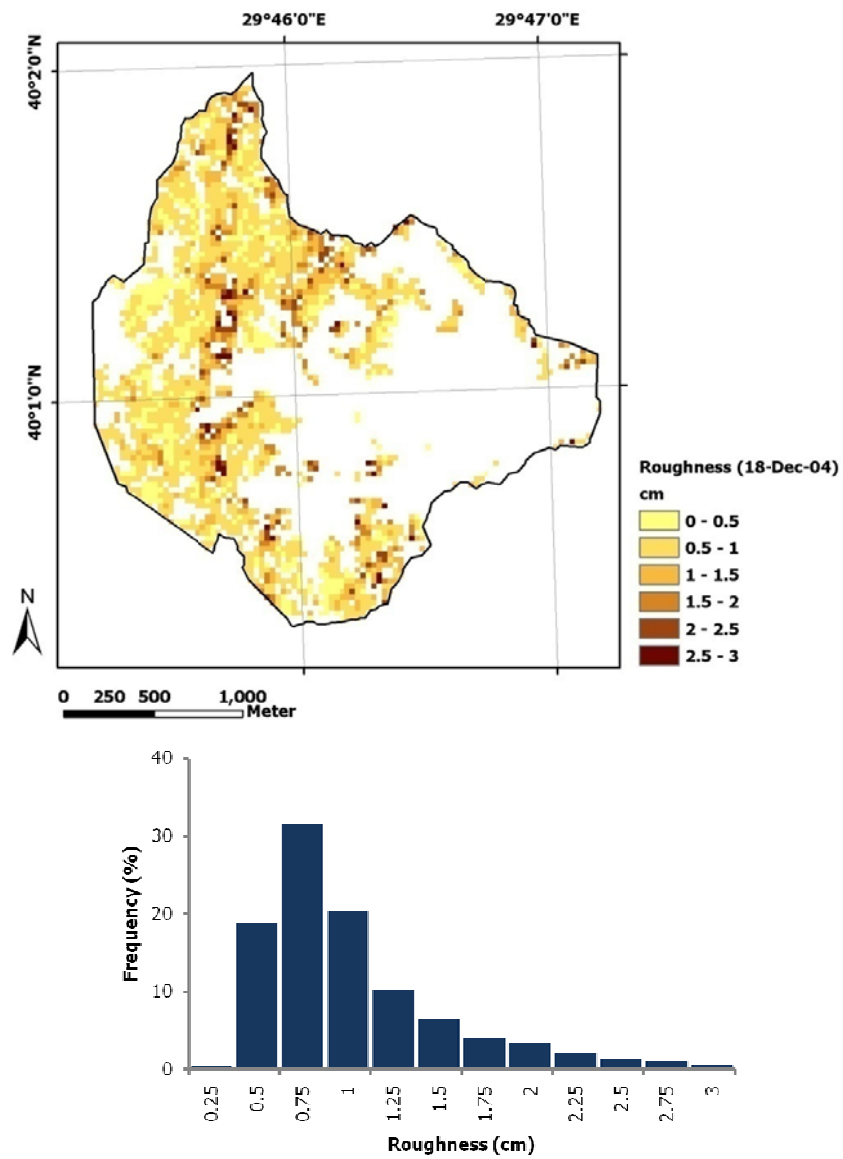


Figure A.2. Soil surface roughness map and histogram for 18-Dec-2004

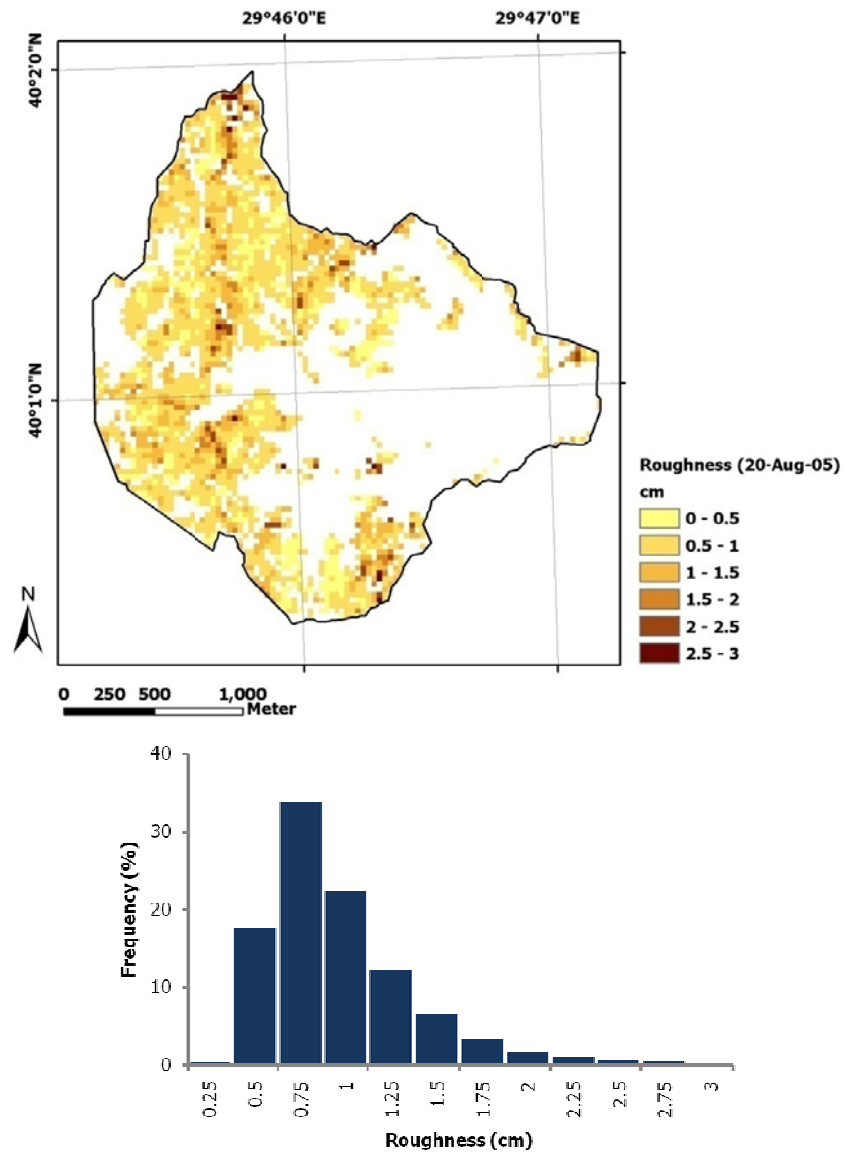


Figure A.3. Soil surface roughness map and histogram for 20-Aug-2005

APPENDIX B

SURFACE SOIL MOISTURE MAPS

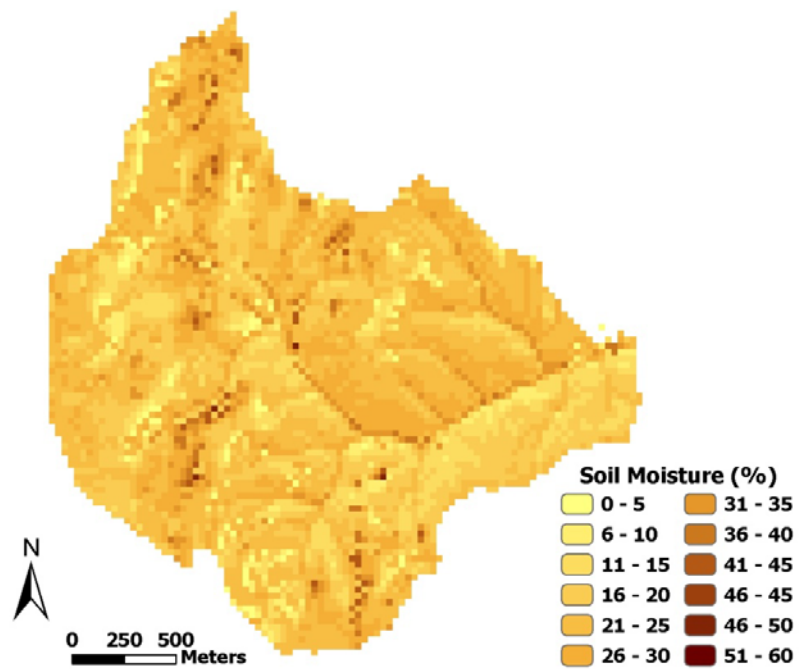


Figure B.1. Soil moisture distribution of the Kurukavak basin for 09-Oct-2004 (SAR)

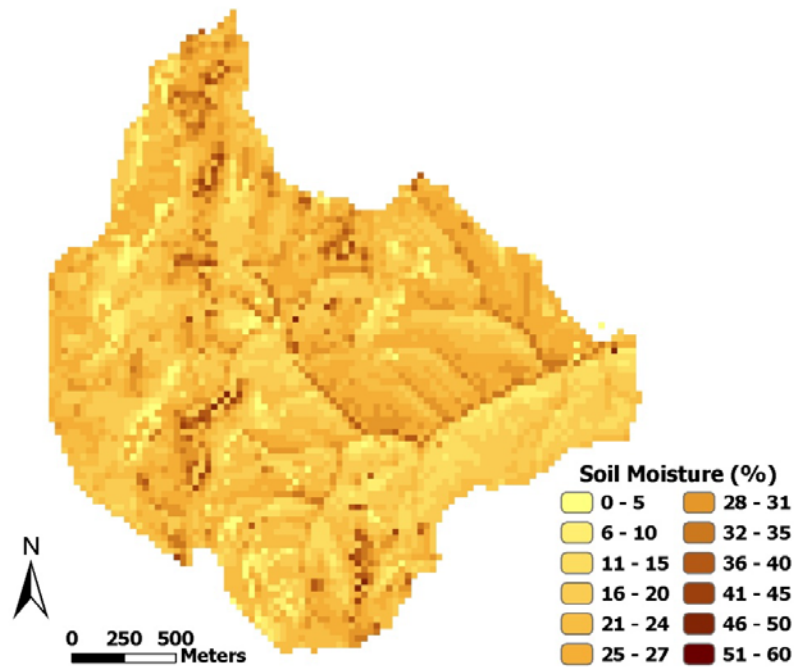


Figure B.2. Soil moisture distribution of the Kurukavak basin for 09-Oct-2004 (ASAR)

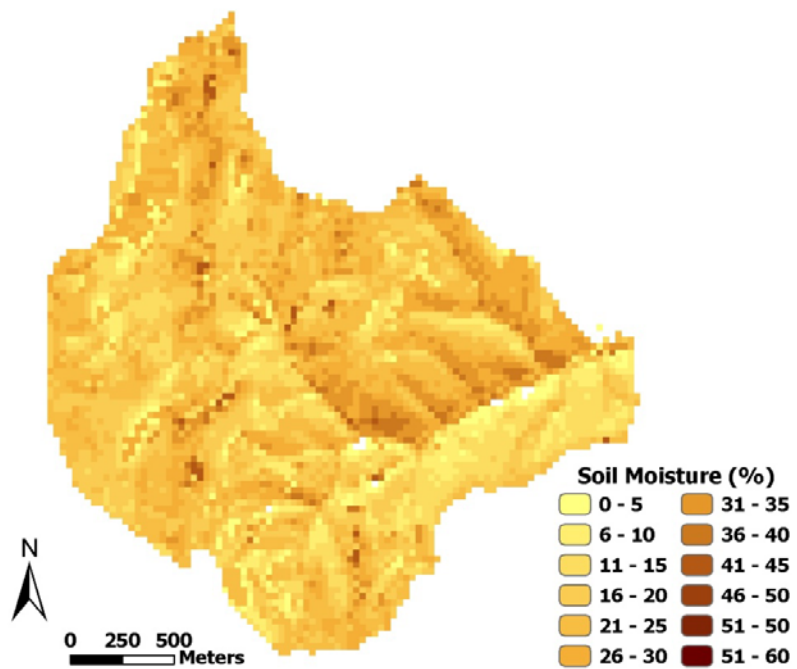


Figure B.3. Soil moisture distribution of the Kurukavak basin for 18-Dec-2004 (SAR)

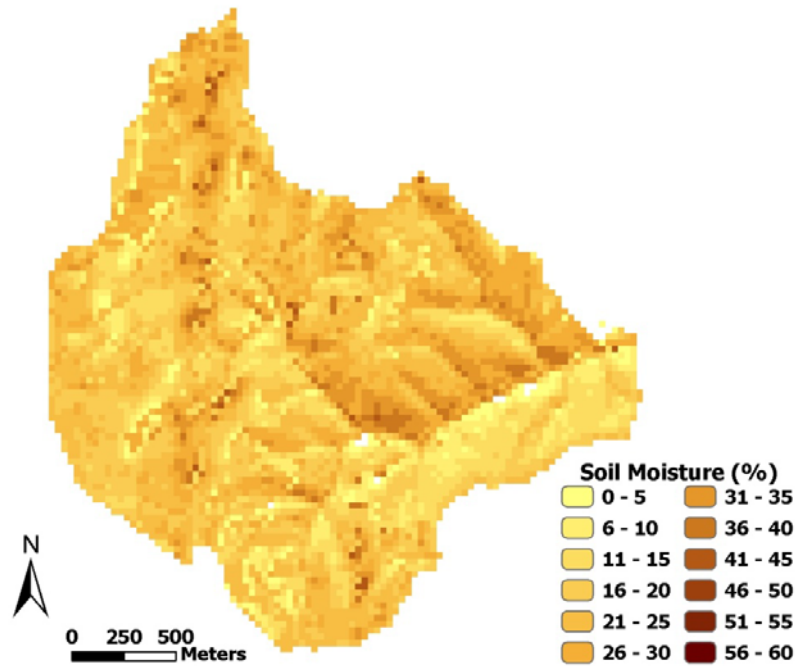


Figure B.4. Soil moisture distribution of the Kurukavak basin for 18-Dec-2004 (ASAR)

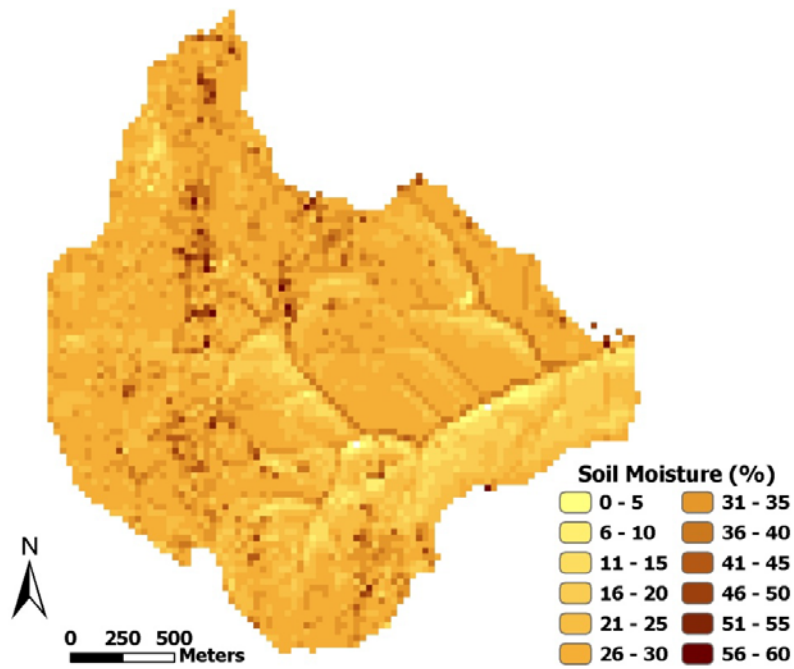


Figure B.5. Soil moisture distribution of the Kurukavak basin for 07-May-05 (SAR)

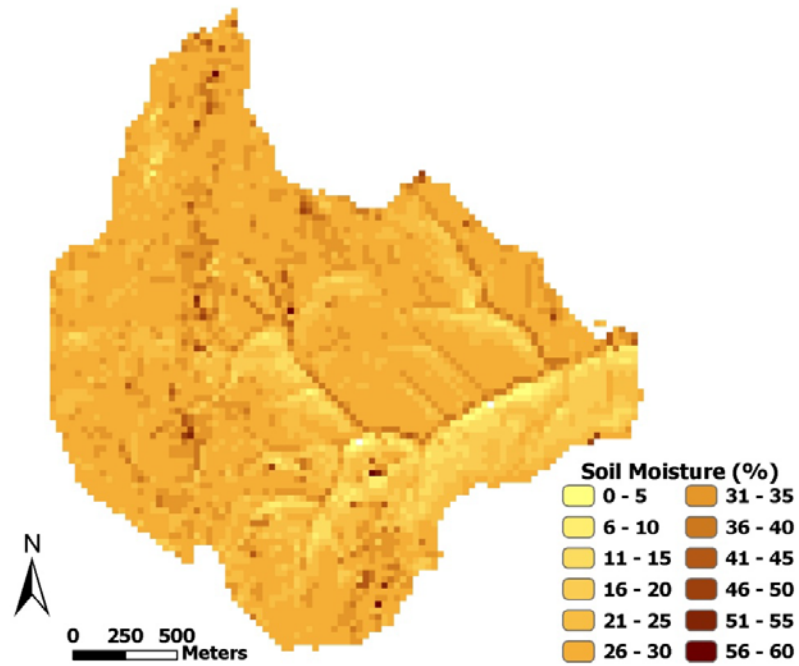


Figure B.6. Soil moisture distribution of the Kurukavak basin for 07-May-05 (ASAR)

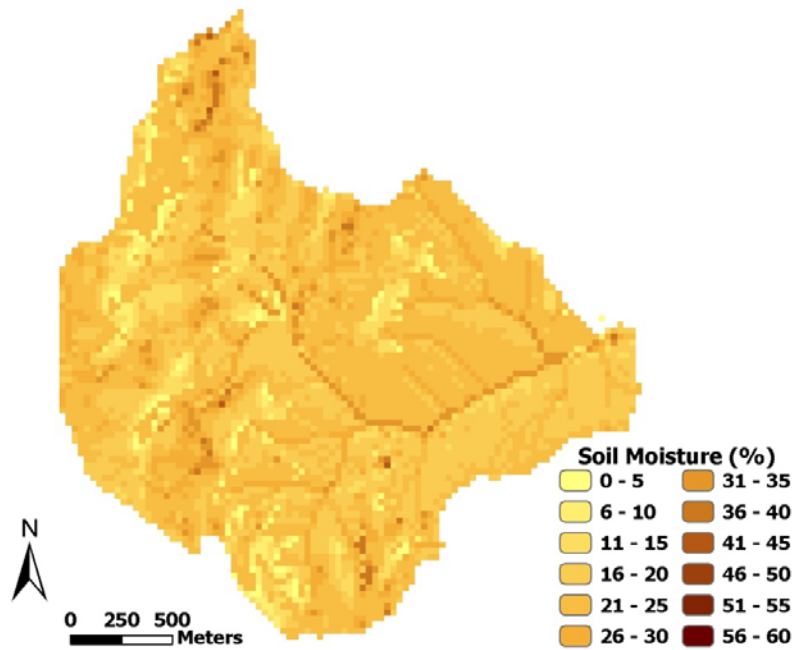


Figure B.7. Soil moisture distribution of the Kurukavak basin for 20-Aug-2005 (SAR)

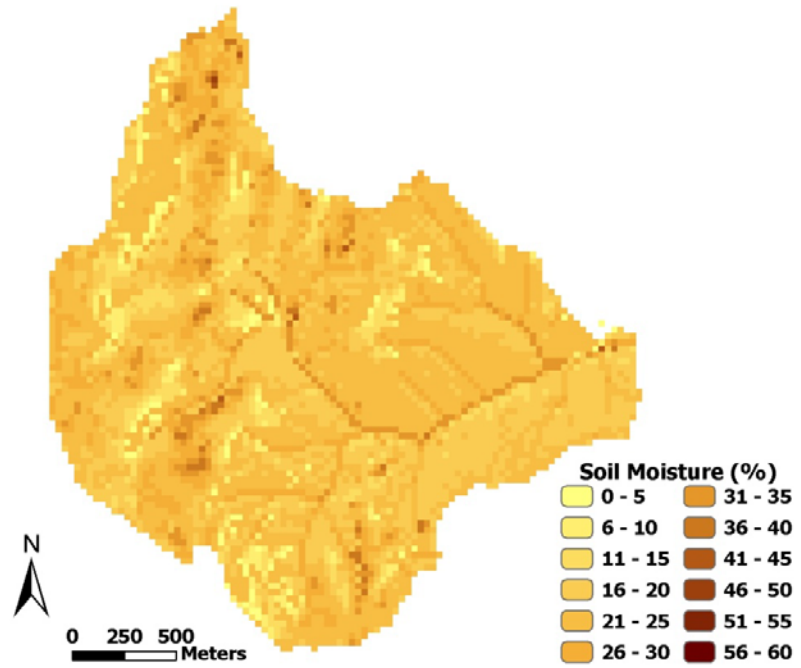


Figure B.8. Soil moisture distribution of the Kurukavak basin for 20-Aug-2005 (ASAR)

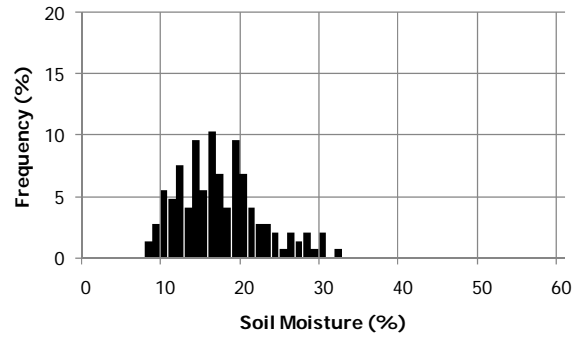
APPENDIX C

**OBSERVED VERSUS COMPUTED
SURFACE SOIL MOISTURE VALUES**

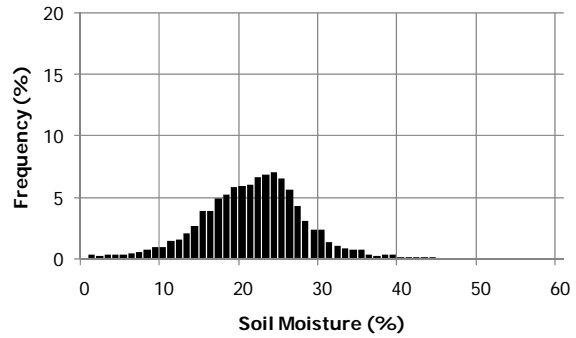
Table C.1. Statistical parameters of the computed and observed soil moisture values for 09-Oct-2004 (Volumetric soil moisture values in %)

		09-Oct-2004	
		SAR	ASAR
Entire Basin Methods I and III (n = 5258)	<i>Mean</i>	20.93	21.00
	<i>Std. Dev.</i>	6.57	6.57
	<i>Max</i>	47.09	48.33
	<i>Min</i>	0.02	0.04
Farmland and Pasture Method I (n = 2392)	<i>Mean</i>	20.57	20.73
	<i>Std. Dev.</i>	8.31	8.38
	<i>Max</i>	47.09	48.33
	<i>Min</i>	0.02	0.04
Forest and Other Method III (n = 2866)	<i>Mean</i>	21.17	21.18
	<i>Std. Dev.</i>	5.06	5.04
	<i>Max</i>	36.80	36.80
	<i>Min</i>	4.33	4.33
Point Soil Moisture Measurements (n = 126)	<i>Mean</i>	16.52	
	<i>Std. Dev.</i>	5.27	
	<i>Max</i>	31.27	
	<i>Min</i>	7.04	

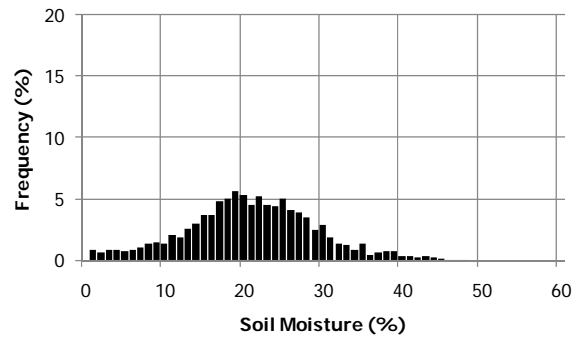
**Point Soil Moisture
Measurements
(*n* = 126)**



**Entire Basin
Methods I and III
(*n* = 5258)**



**Farmland and
Pasture
Method I
(*n* = 2392)**



**Forest and Other
Method III
(*n* = 2866)**

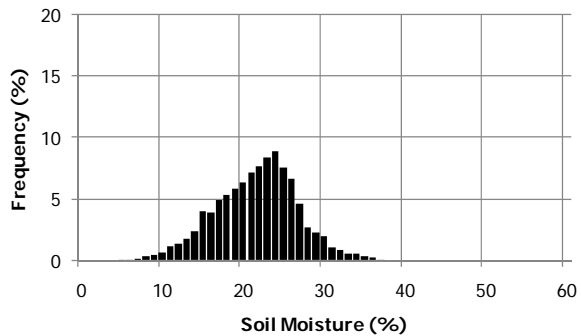
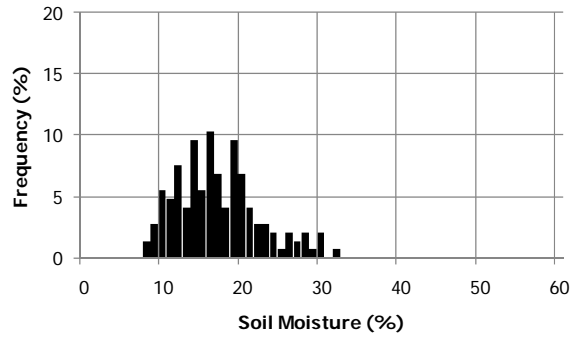
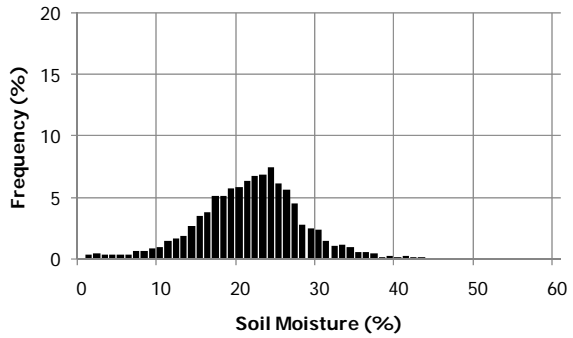


Figure C.1. Frequency histograms of the computed and observed soil moisture values for the 09-Oct-2004 SAR image

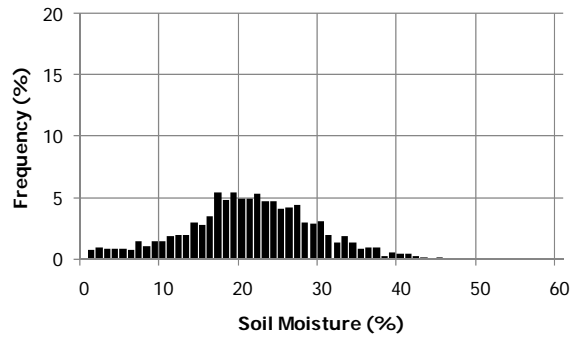
**Point Soil Moisture
Measurements
(*n* = 126)**



**Entire Basin
Methods I and III
(*n* = 5258)**



**Farmland and
Pasture
Method I
(*n* = 2392)**



**Forest and Other
Method III
(*n* = 2866)**

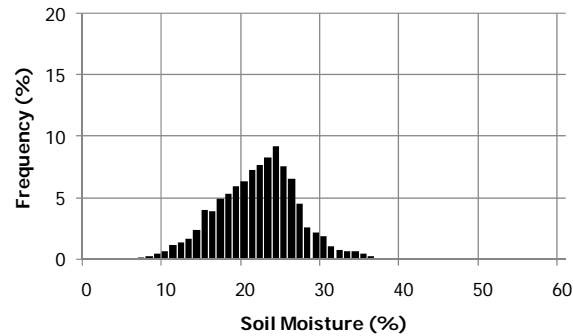
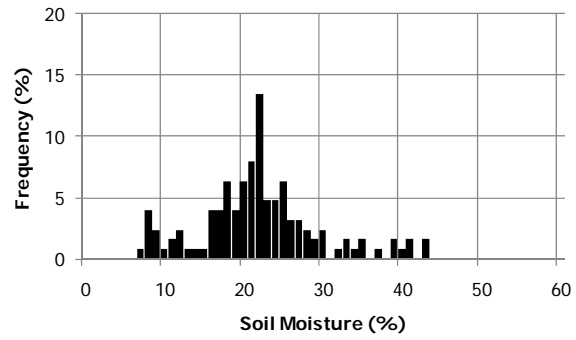


Figure C.2. Frequency histograms of the computed and observed soil moisture values for the 09-Oct-2004 ASAR image

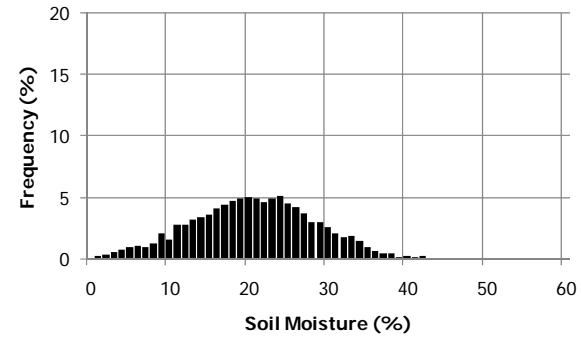
Table C.2. Statistical parameters of the computed and observed soil moisture values for 18-Dec-2004 (Volumetric soil moisture values in %)

		18-Dec-2004	
		SAR	ASAR
Entire Basin Methods I and III (n = 5258)	<i>Mean</i>	20.18	20.23
	<i>Std. Dev.</i>	7.81	7.82
	<i>Max</i>	44.61	44.94
	<i>Min</i>	0.04	0.16
Farmland and Pasture Method I (n = 2392)	<i>Mean</i>	19.36	19.46
	<i>Std. Dev.</i>	7.81	7.86
	<i>Max</i>	44.61	44.94
	<i>Min</i>	0.04	0.16
Forest and Other Method III (n = 2866)	<i>Mean</i>	20.77	20.77
	<i>Std. Dev.</i>	7.75	7.74
	<i>Max</i>	41.56	41.56
	<i>Min</i>	1.02	1.02
Point Soil Moisture Measurements (n = 126)	<i>Mean</i>	21.58	
	<i>Std. Dev.</i>	7.63	
	<i>Max</i>	42.85	
	<i>Min</i>	6.64	

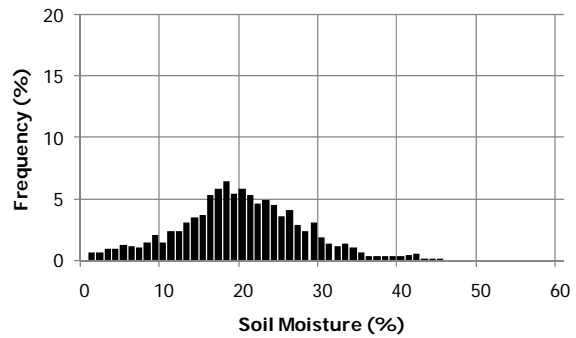
**Point Soil Moisture
Measurements**
(n = 126)



**Entire Basin
Methods I and III**
(n = 5258)



**Farmland and
Pasture
Method I**
(n = 2392)



**Forest and Other
Method III**
(n = 2866)

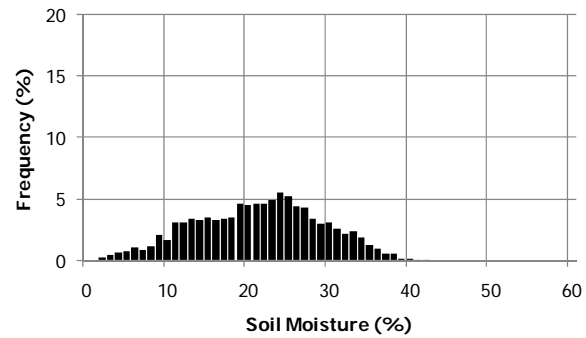
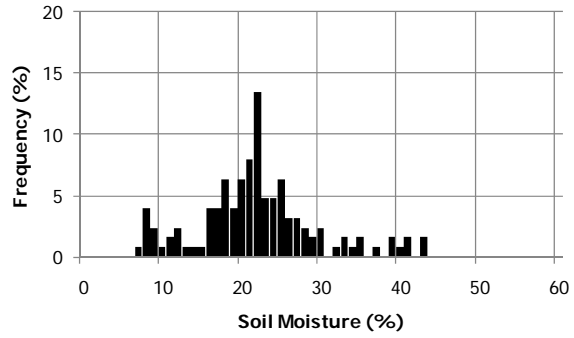
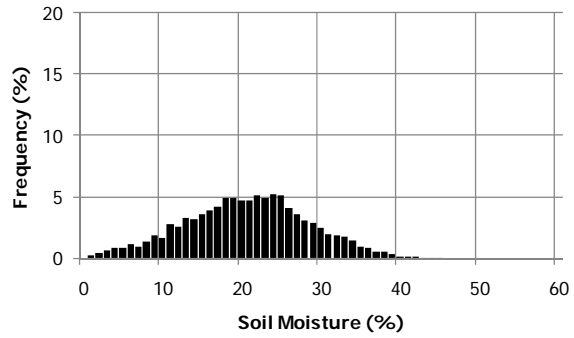


Figure C.3. Frequency histograms of the computed and observed soil moisture values for the 18-Dec-2004 SAR image

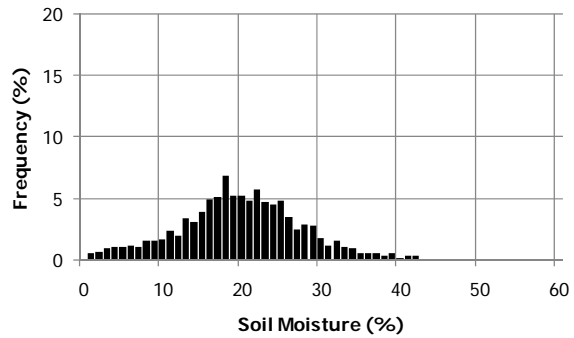
**Point Soil Moisture
Measurements**
(n = 126)



**Entire Basin
Methods I and III**
(n = 5258)



**Farmland and
Pasture
Method I**
(n = 2392)



**Forest and Other
Method III**
(n = 2866)

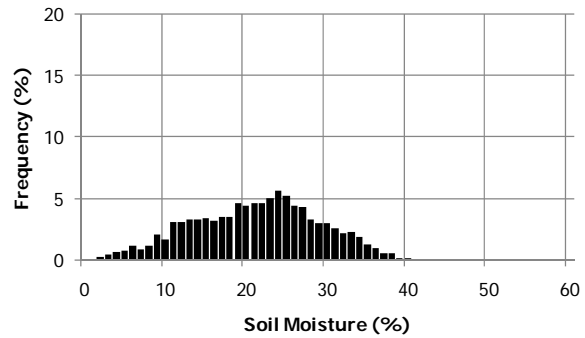
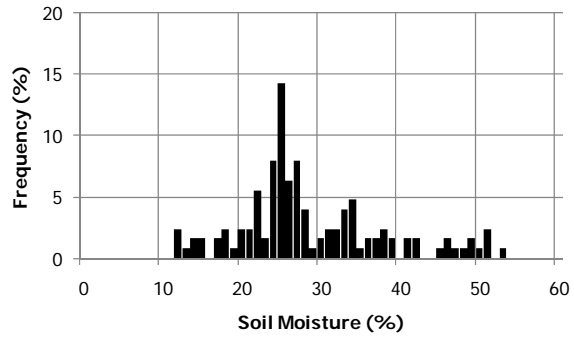


Figure C.4. Frequency histograms of the computed and observed soil moisture values for the 18-Dec-2004 ASAR image

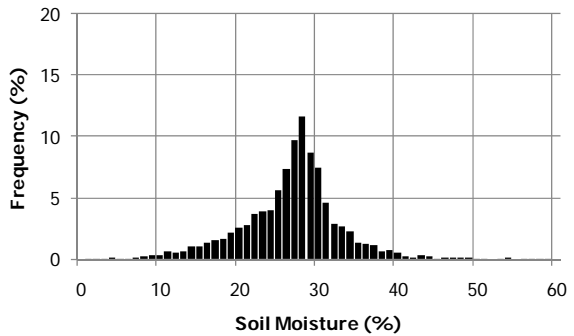
Table C.3. Statistical parameters of the computed and observed soil moisture values for 07-May-2005 (Volumetric soil moisture values in %)

		07-May-2005	
		SAR	ASAR
Entire Basin Methods II and III (n = 5258)	<i>Mean</i>	26.21	26.12
	<i>Std. Dev.</i>	6.51	5.86
	<i>Max</i>	58.61	58.03
	<i>Min</i>	0.68	0.68
Farmland and Pasture Method II (n = 2392)	<i>Mean</i>	29.13	28.91
	<i>Std. Dev.</i>	5.88	4.21
	<i>Max</i>	58.61	58.03
	<i>Min</i>	3.30	0.97
Forest and Other Method III (n = 2866)	<i>Mean</i>	23.87	23.86
	<i>Std. Dev.</i>	6.02	6.03
	<i>Max</i>	40.14	40.14
	<i>Min</i>	0.68	0.68
Point Soil Moisture Measurements (n = 126)	<i>Mean</i>	28.20	
	<i>Std. Dev.</i>	9.18	
	<i>Max</i>	52.77	
	<i>Min</i>	11.57	

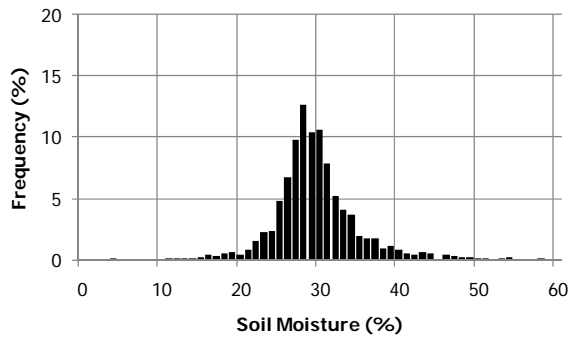
**Point Soil Moisture
Measurements**
(n = 126)



**Entire Basin
Methods II and III**
(n = 5258)



**Farmland and
Pasture
Method II**
(n = 2392)



**Forest and Other
Method III**
(n = 2866)

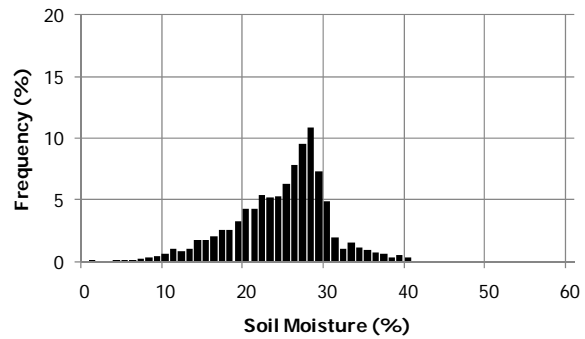
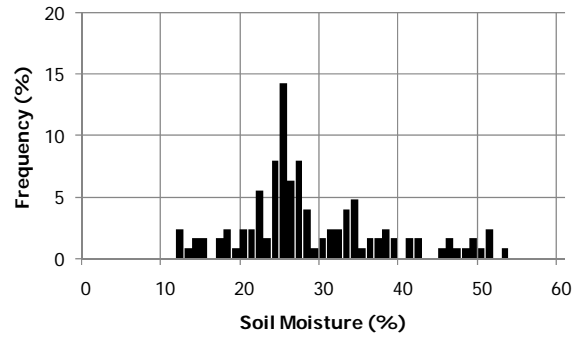
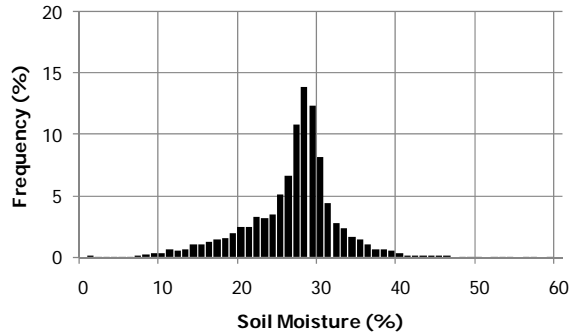


Figure C.5. Frequency histograms of the computed and observed soil moisture values for the 07-May-2005 SAR image

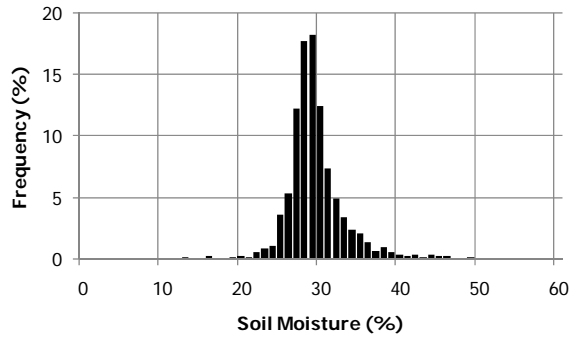
**Point Soil Moisture
Measurements
(*n* = 126)**



**Entire Basin
Methods II and III
(*n* = 5258)**



**Farmland and
Pasture
Method II
(*n* = 2392)**



**Forest and Other
Method III
(*n* = 2866)**

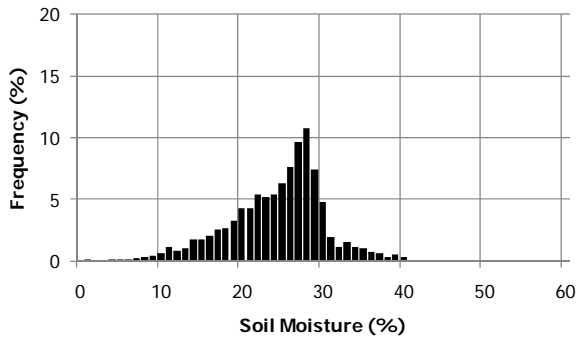
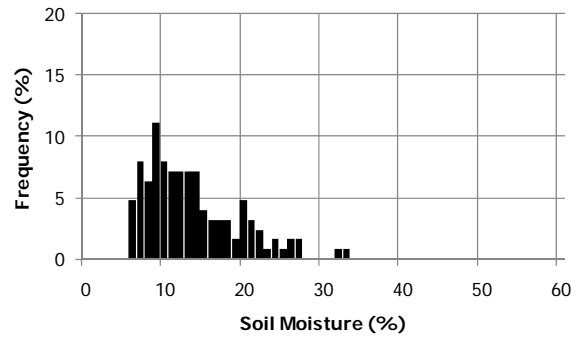


Figure C.6. Frequency histograms of the computed and observed soil moisture values for the 07-May-2005 ASAR image

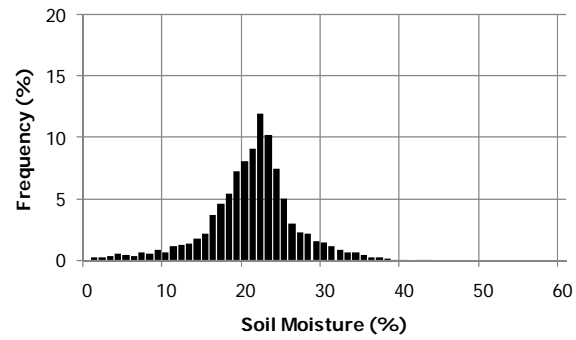
Table C.4. Statistical parameters of the computed and observed soil moisture values for 20-Aug-2005 (Volumetric soil moisture values in %)

		20-Aug-2005	
		SAR	ASAR
Entire Basin Methods I and III (n = 5258)	<i>Mean</i>	20.45	20.70
	<i>Std. Dev.</i>	5.58	5.67
	<i>Max</i>	42.34	45.27
	<i>Min</i>	0.02	0.03
Farmland and Pasture Method I (n = 2392)	<i>Mean</i>	18.90	19.46
	<i>Std. Dev.</i>	7.29	7.60
	<i>Max</i>	42.34	45.27
	<i>Min</i>	0.02	0.03
Forest and Other Method III (n = 2866)	<i>Mean</i>	21.58	21.58
	<i>Std. Dev.</i>	3.47	3.45
	<i>Max</i>	35.11	35.11
	<i>Min</i>	11.44	11.44
Point Soil Moisture Measurements (n = 126)	<i>Mean</i>	12.98	
	<i>Std. Dev.</i>	5.85	
	<i>Max</i>	32.69	
	<i>Min</i>	5.09	

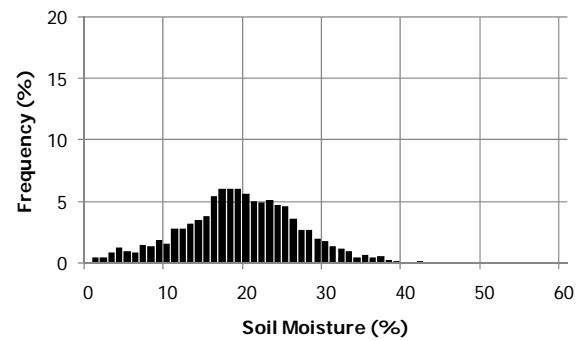
**Point Soil Moisture
Measurements**
(n = 126)



**Entire Basin
Methods I and III**
(n = 5258)



**Farmland and
Pasture
Method I**
(n = 2392)



**Forest and Other
Method III**
(n = 2866)

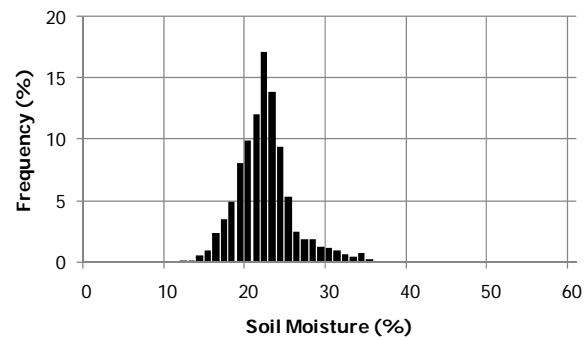
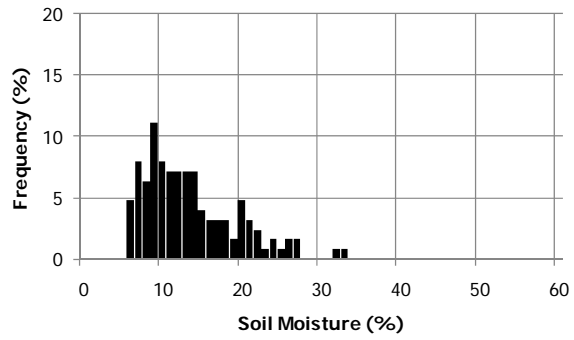
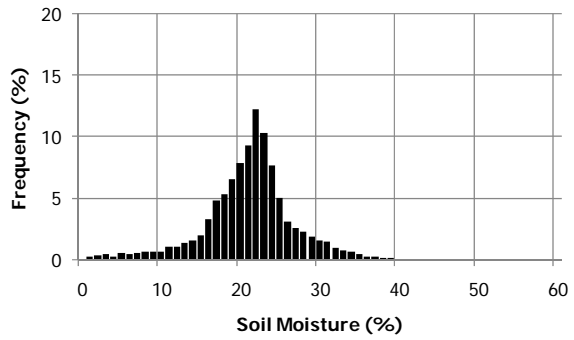


Figure C.7. Frequency histograms of the computed and observed soil moisture values for the 20-Aug-2005 SAR image

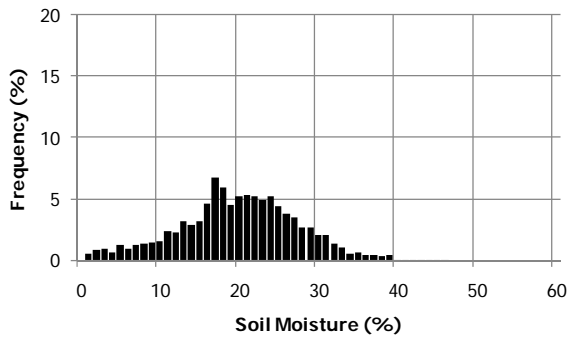
**Point Soil Moisture
Measurements**
(n = 126)



**Entire Basin
Methods I and III**
(n = 5258)



**Farmland and
Pasture
Method I**
(n = 2392)



**Forest and Other
Method III**
(n = 2866)

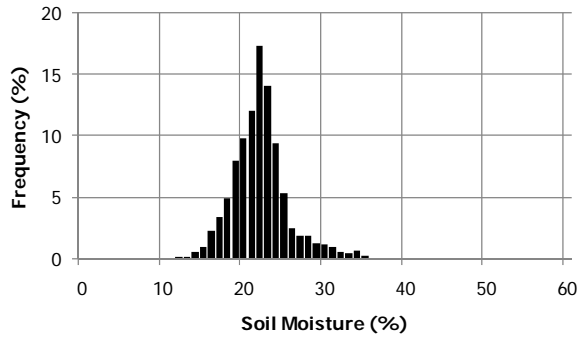


Figure C.8. Frequency histograms of the computed and observed soil moisture values for the 20-Aug-2005 ASAR image

CURRICULUM VITAE

PERSONAL INFORMATION

Surname, Name: Yılmaz, Musa

Nationality: Turkish (TC)

Date of Birth: 20 August 1978

Email: musa@musayilmaz.com

EDUCATION

Degree	Institution	Year of Graduation
PhD	METU Civil Engineering	2008
MS	METU Civil Engineering	2003
BS	METU Civil Engineering	2000
High School	Antalya Anatolian High School, Antalya	1996

WORK EXPERIENCE

Year	Place	Enrollment
2000 - 2007	METU Civil Engineering	Research Assistant

FOREIGN LANGUAGE

English